STABILITY AND STRUCTURE OF HYDROGEN DEFECTS IN ZINC OXIDE

By

SLADE JOSEPH JOKELA

A dissertation submitted in partial fulfillment
of the requirements for the degree of

DOCTOR OF PHILOSOPHY

WASHINGTON STATE UNIVERSITY
Materials Science Program

DECEMBER 2006

To the Faculty of Washington State University:

The members of the Committee appointed to examine the dissertation of SLADE JOSEPH JOKELA find it satisfactory and recommend that it be accepted.

_____

Chair

_____

_____

STABILITY AND STRUCTURE OF HYDROGEN
DEFECTS IN ZINC OXIDE

Abstract

Slade J. Jokela, Ph.D.
Washington State University
December 2006

Chair: Matthew D. McCluskey

Zinc oxide (ZnO) is a wide band gap semiconductor with potential optical, electronic, and mechanical applications. First-principles investigations predicted that hydrogen impurities act as shallow donors in ZnO. IR spectroscopy showed that hydrogen exhibits a local vibrational mode at 3326.3 cm^{-1}, at liquid-helium temperatures, corresponding to an O-H type bond. Results from high-pressure and polarized IR spectroscopy strongly suggest that hydrogen occupies an antibonding location with an O-H bond oriented at an angle of 110.6° from the c axis. By correlating the IR absorbance strength with free-electron concentration, it was established that the O-H complexes are shallow donors. However, the O-H donors are unstable, decaying significantly after several weeks at room temperature. The kinetics of the dissociation follow a bimolecular decay model, consistent with the formation of H_2 molecules. Attempts at chemical vapor transport (CVT) growth of ZnO crystals were successful. Results varied from Zn-rich, orange-colored samples to nearly colorless ZnO polycrystals. Further analysis revealed an unknown contaminant that became apparent after annealing in hydrogen, resulting in an IR absorption peak at 3150 cm^{-1}.

TABLE OF CONTENTS

LIST OF FIGURES

LIST OF TABLES

ACKNOWLEDGMENTS

The last five years seem to be a blur in comparison to the last five months. I would not have been able to make it through with out the help and support of so many people. First and foremost in this long list is my advisor, Dr. Matthew McCluskey. He has helped me through many situations over the last six years. More to the point, he has introduced me to the countless researchers I will be working with for the rest of my career. I would like to thank Dr. Kelvin Lynn and Dr. Ursula Mazur for their presence on my committee as well as their help with my research.

In addition to my advisors, I would also like to thank all of my peers in the Physics Department and Materials Science Program. I would like to specifically thank Bonner Walsh for helping out on late night study sessions by providing distractions, whether appropriately timed or not. Additional thanks goes to the rest of the McCluskey group: Gabriel Hanna, Win Maw Hlaing Oo, and Bobbie Riley for picking up any slack that I may have been responsible for.

Further thanks are in order for the entire faculty and staff of the Physics Department and Materials Science Program. I would like to thank Dr. Guy Worthey for allowing me to set up my telescope in the observatory. I cannot say how much of a relief it is to just sit and look up at the stars. Dr. Michael Allen has also contributed to my hobby in astronomy.

Last, but certainly not least, I would like to thank my parents, John and Renee, for providing the support necessary for me to make it to and through college. Also,

my brother and sister, Justin and Tawnya, have given a great deal of encouragement.

This work was supported by the National Science Foundation under Grant No. DMR-0203832. Partial support was provided by Washington State University's Institute for Shock Physics through DOE Grant No. DE-FG03-97SF21388 as well as the American Chemical Society Petroleum Research Fund.

Chapter 1
INTRODUCTION

Our current age of microelectronics would not be possible without the pioneering efforts that discovered the industry-changing properties of semiconductors. Where before there were comparatively simple electronics containing bulky vacuum tubes, we now have complex hand-held computing devices composed of millions of solid-state transistors. Since the invention of the transistor over a half-century ago [Bardeen and Brattain (1948); Shockley and Pearson (1948)], research into the field of semiconductors has been focused on producing smaller, more efficient, and less expensive alternatives to existing technologies, and finding new uses for existing materials. With the ability to manipulate and control the electrical and optical properties of materials, there seems to be no end in sight for productive research into semiconductors. Zinc oxide (ZnO) is a semiconductor with a wide range of applications, potentially replacing GaN as a blue or UV-light emitting diode as well as use in transparent transistors. Hydrogen defects, the focus of this thesis, have complicated the advances necessary for ZnO to become a front-runner in solid-state optoelectronic devices.

A semiconductor is a crystalline material which is typically composed of covalently bonded atoms. Neighboring atoms in the lattice complete each other's electron shells. Atoms bonded in a crystal lattice give rise to a complex structure of allowed and forbidden energies that each electron can occupy. The ranges of allowed electron energies are known as *bands* while the forbidden energies are known as *band gaps*. In

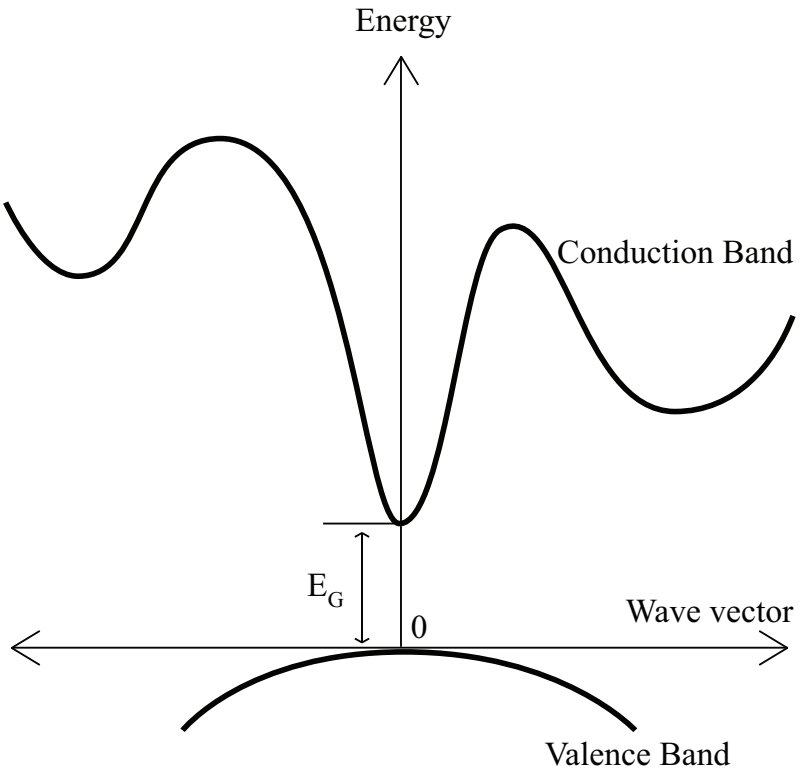

Figure 1.1: An example of a band diagram similar to GaAs. The band gap energy is labeled E_G.

an intrinsic semiconductor held at absolute zero temperature, the band structure is composed of completely filled bands and completely empty bands. The filled bands are those that the electrons occupy while in their ground state. The empty bands are all of higher energy than the occupied energy bands. Of the occupied bands, the one with highest energy is known as the *valence band*, corresponding to the valence shell of electrons. Of the unoccupied bands, the band of lowest energies is known as the *conduction band*.

The energy difference between the lowest point in the conduction band and the highest point in the valence band is the minimum amount of energy needed to excite an electron out of the valence band (Fig. 1.1). Once the electron is in the conduction

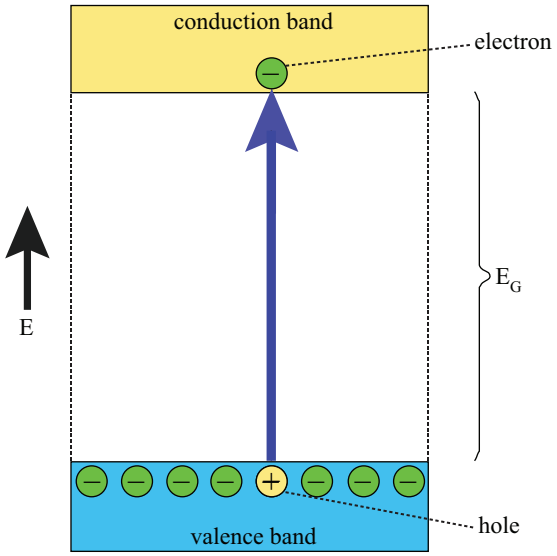

Figure 1.2: A simplified band structure showing an electron excited across the band gap and into the conduction band.

band, it is free to move as a charge carrier through the crystal. The space once occupied by the electron, in the valence band, can be filled by a valence electron from a neighboring atom. This missing electron is called a *hole.* The hole drifts between atoms, behaving as a positive charge carrier, in much the same way as an electron in the conduction band can carry negative charge through the crystal. With increased temperatures, an electron has an increasing probability of occupying the conduction band. At room temperature, for a band gap of a few eV, only a small fraction of electrons occupy the conduction band (Fig. 1.2).

The interruption of translational symmetry of the lattice has interesting effects on the band structure of the semiconductor. For instance, the inclusion of an impurity atom or *dopant* into the lattice can introduce an energy level within the band gap. If this energy level is near the conduction band (valence band), the impurity is known as a *donor* (*acceptor*). A donor can have its electron easily excited into the conduction

band where it is allowed to conduct current. An acceptor provides an energy level near the valence band, where an electron can be easily excited into the acceptor level, allowing the remaining hole in the valence band to conduct current. In an ideal intrinsic semiconductor, the number of holes in the valence band is always equal to the number of electrons in the conduction band. A semiconductor with dopants, however, will have an excess of free electrons or holes. Materials with electrons (holes) as the primary charge carrier are known as n-type (p-type) semiconductors.

The simplest example that can be given is a comparison of n-type and p-type crystalline silicon. The electron structure for silicon's outermost shell is $3s^2 3p^2$, requiring four more electrons to complete the 3p subshell. In crystalline silicon, the completed subshell for a silicon atom is achieved by sharing electrons with four of its neighboring atoms; the sharing of electrons is known as covalent bonding. In this manner, each Si atom shares four of its electrons with each of the four neighboring Si atoms. Each Si atom in the lattice shares electrons to complete its own 3p subshell and contributes to the completion of the neighboring atoms' 3p subshells.

If an impurity is now substituted on the silicon lattice, the perfect covalent bonding is interrupted. For instance, if we look at the electron configuration for phosphorus ($3s^2 3p^3$), we will note that it has five electrons that it can easily donate. When substituted on the silicon lattice, the additional electron in the phosphorus valence shell has a binding energy of only 45 meV. This is sufficiently low that even at room temperature the electron is excited into the conduction band. In an elemental semiconductor like silicon, phosphorus is defined as a donor impurity and silicon doped with phosphorus atoms is an n-type semiconductor. If we use boron ($3s^2 3p^1$) as an impurity, we note that it has only three valence electrons. The incomplete valence shell is essentially a hole, as mentioned before. At room temperature, this hole can

easily be filled by a neighboring silicon atom's electron, but the hole does not disappear. Instead, it jumps around between atoms, behaving as a positively charged carrier. Under these conditions, boron is defined as an acceptor impurity and the material is a p-type semiconductor.

Hydrogenic model of a donor

The introduction of a phosphorus atom into crystalline silicon leaves one electron free from a covalent bond. However, the electron is still weakly bound to the positive phosphorus ion by Coulomb attraction. The phosphorus ion and electron can be thought of as a hydrogenic system, which can be modeled using the Bohr model for hydrogen. As discussed in Kittel (2005), the effective electron mass in direct-gap semiconductors is given by

$$\frac{1}{m^*} = \frac{1}{\hbar^2}\frac{d^2E}{dk^2}, \tag{1.1}$$

where m^* is the effective electron mass and $\frac{d^2E}{dk^2}$ is the curvature of the conduction band or valence band. Using the Bohr model, we then obtain the binding energy for this electron:

$$E_B = \frac{13.6\text{eV}}{\epsilon^2}\frac{m^*}{m_e}, \tag{1.2}$$

where ϵ is the dielectric constant and m_e is the mass of a free electron. Likewise, the Bohr radius is given by

$$a_0 = 0.5\text{Å}\frac{\epsilon m_e}{m^*}. \tag{1.3}$$

Vibrational effects of impurities

Not only do impurities affect the electronic properties of materials, but they also affect the vibrational properties of the lattice [Barker and Sievers (1975)]. The atoms

that compose a crystal lattice are bonded together, so they do not vibrate independently of each other. Instead, vibrations in a crystal lattice occur over the length of the crystal in collective modes. As with the quantum harmonic oscillator, these oscillations exhibit quantized energies. Each unit of quantized vibrational energy is called a *phonon*. In this system of vibrational modes, there exists a maximum phonon frequency that can be associated with lattice vibrations. The maximum frequency is reached when the wavelength of the mode approaches a lower limit, equal to twice the atomic spacing (Sec. 2.3).

When the perfect symmetry of a lattice is broken by an impurity, new vibrational modes are created. In the case that a light atom, such as hydrogen, replaces a heavier atom, vibrational modes arise with energies much higher than that of the maximum phonon energy. This vibrational mode is localized in both real space and frequency space, and is called a *local vibrational mode* (LVM).

1.1 Zinc oxide

1.1.1 Background

Zinc oxide is a wide band gap semiconductor which is already prevalent in today's commerce and industry. The 3.4 eV band gap gives ZnO a broad range of potential uses in optical and electrical applications [Pearton *et al.* (2004)]. However, when single-crystal bulk ZnO is grown by any of the common growth techniques, it exhibits n-type conductivity. As of now, there are no methods which reliably produce p-type ZnO. In order for these applications to come to fruition, p-type ZnO must be realized.

With the advent of p-type ZnO will also come light emitting diodes (LEDs), with emission ranging from blue to ultraviolet, that will replace more expensive, less efficient [Look (2001)], and difficult to grow [Ntep *et al.* (1999)] GaN devices. Further

applications include transparent electronic devices for use in liquid-crystal displays (LCDs) [Wager (2003)] or any other application where an invisible transistor or electronic circuit may be advantageous. ZnO has been used as a transparent conductor [Minami (2000)] in solar cells [Nuruddin and Abelson (2001)]. It also has the benefit of being ecologically friendly; it's even used as a mineral supplement in animal feed [Smith *et al.* (1997)].

Spintronics is also a developing field that may benefit from ZnO [Prinz (1998); Dietl and Ohno (2003); Kamilla and Basu (2002)]. The storage [Parkin *et al.* (2003)] and manipulation [Steane (1998)] of information using the spin states of impurities or charge carriers may prove practical for quantum computing or memory applications. Mn-doped *p*-type ZnO is theorized to be ferromagnetic at room temperature [Dietl *et al.* (2000)]. Combined with the potential optical and electrical properties of ZnO, room-temperature ferromagnetism would be a useful feature for magneto-optical switches [Didosyan *et al.* (2004)], spin LEDs [Jonker *et al.* (2000); Ohno *et al.* (1999); Kikkawa and Awschalom (1999); Fiederling *et al.* (1999)], and spin-polarized solar cells [Zutic *et al.* (2001)].

1.1.2 Single-crystal zinc oxide growth methods

In contrast to GaN, bulk single-crystal ZnO can be grown by several techniques. The common methods used for growing bulk ZnO are melt growth, vapor growth, solution growth, and hydrothermal growth.

Melt growth

One of the methods of growing crystals is to start with molten ZnO and allow it to cool slowly. Crystallization is achieved at a solid/liquid interface, the position

of which is defined by a controllable temperature gradient. The pressurized melt growth of ZnO used by Cermet Inc. is proprietary, the precise details of which are not released [Nause *et al.* (2005)]. Their method was developed around the need for melt growth methods involving materials with high melting temperatures, at which point the material also becomes extremely reactive. In the case for ZnO, temperatures in excess of 2000 °C are necessary to melt the material. These temperatures are achieved by radio-frequency energy, which induces Joule heating within the material. At this temperature, ZnO will readily decompose into its constituent elements. To prevent this, Cermet Inc. uses a pressurization technique that introduces an oxygen atmosphere at pressures up to 100 atm. To prevent contamination from the crucible walls, Cermet Inc. fashions a crucible out of whatever material is to be grown (in this case, ZnO). The crucible is externally cooled to prevent melting.

Vapor growth

Vapor growth is the condensation of materials from the vapor phase. The simplest of cases would involve a material with a high vapor pressure that is slowly condensed onto a cooler point in the growth chamber. In vapor growth, a seed crystal can be used to enhance oriented growth of the crystal. However, ZnO has a rather low vapor pressure, making this a difficult and slow endeavor. Another method, chemical vapor transport (CVT), uses an intermediate chemical reaction. In the case of ZnO, this reaction involves the formation of two different species of materials, both of which have vapor pressures higher than that of ZnO. We have employed this method for our ZnO growth. See Sec. 3.6 for a more detailed description of this technique. The use of a seed is also possible with CVT and is known as seeded chemical vapor transport (SCVT). SCVT was employed by Eagle Picher for their ZnO growth technique.

Solution growth

Solution growth of ZnO is achieved by dissolving ZnO in a solution, such as PbF_2, at an elevated temperature near 1150°C. At this temperature the solubility of ZnO in PbF_2 is 30%. As the mixture is cooled, ZnO will begin to precipitate out of the solution. When the mixture has solidified, it is composed of inhomogeneous pockets of ZnO. These ZnO crystals must be broken free of the PbF_2 matrix, making this an inefficient growth technique.

Hydrothermal growth

Hydrothermal growth uses an aqueous solvent at elevated temperatures and pressures to dissolve ZnO. Commonly, NaOH, LiOH, and KOH are used as solvents. The use of a solvent allows the growth process to be carried out at much lower temperatures as compared to melt growth and CVT growth methods. The hydrothermal growth technique has the advantage of creating high quality crystals. However, this comes with an expense; the growth rate is roughly 250 μm per day. Hydrothermal growth also has the effect of incorporating the elemental components of the solvent into the crystal, an advantage or disadvantage depending on the goal of the researcher.

1.1.3 Electronic properties of as-grown ZnO

As grown, ZnO typically has n-type conductivity. It is thought that various defects, including hydrogen, oxygen vacancies, and zinc interstitials may be partially responsible for the as-grown conductivity of ZnO [Look *et al.* (1999)]. The latter two have been ruled out in calculations by Janotti and Van de Walle (2006). It is also possible that unintentional group-III element doping may also be partially responsible for the donor concentration in as-grown ZnO.

The difficulty in obtaining *p*-type ZnO stems from the high concentration of donors in as-grown samples. The donors compensate acceptors that are introduced for the purpose of obtaining *p*-type conductivity. Several attempts to overcome this hurdle have been made with nitrogen [Look *et al.* (2002); Kobayashi *et al.* (1983); Nakahara *et al.* (2002); Li *et al.* (2003); Singh *et al.* (2003)], as well as other group-V elements [Kim *et al.* (2003); Ryu *et al.* (2003); Aoki *et al.* (2002); Limpijumnong *et al.* (2004)], as an acceptor dopant. Though promising, there are still uncertainties about the reliability of measurements of samples containing these dopants. Independent studies have failed to reproduce reports of *p*-type ZnO. While the group-V elements are promising, more work must be done on achieving *p*-type ZnO with a low level of compensating donors [Look *et al.* (2005)]. Work has shown that Li and Na substituting for Zn also behave as acceptors. However, difficulties arise due to self-compensation that occurs when Li and Na reside at interstitial locations.

1.1.4 ZnO crystallography

The structure of ZnO is wurtzite with lattice parameters c = 5.220 Å, a = 3.258 Å [Decremps *et al.* (2003)], and u = 0.382 (see Fig. 1.3). The ratio, c/a=1.600 and the value of u = 0.380, are approximately that of the ideal (close-pack) wurtzite lattice, 1.633 and 0.375 respectively.

1.2 Hydrogen in zinc oxide

1.2.1 Pioneering research

The study of hydrogen defects in ZnO is not a new one, but one that has been reinvigorated in recent years. Early studies performed in the 1950's by Mollwo (1954) and Thomas and Lander (1956) concerned hydrogen diffusion into ZnO crystals. Both

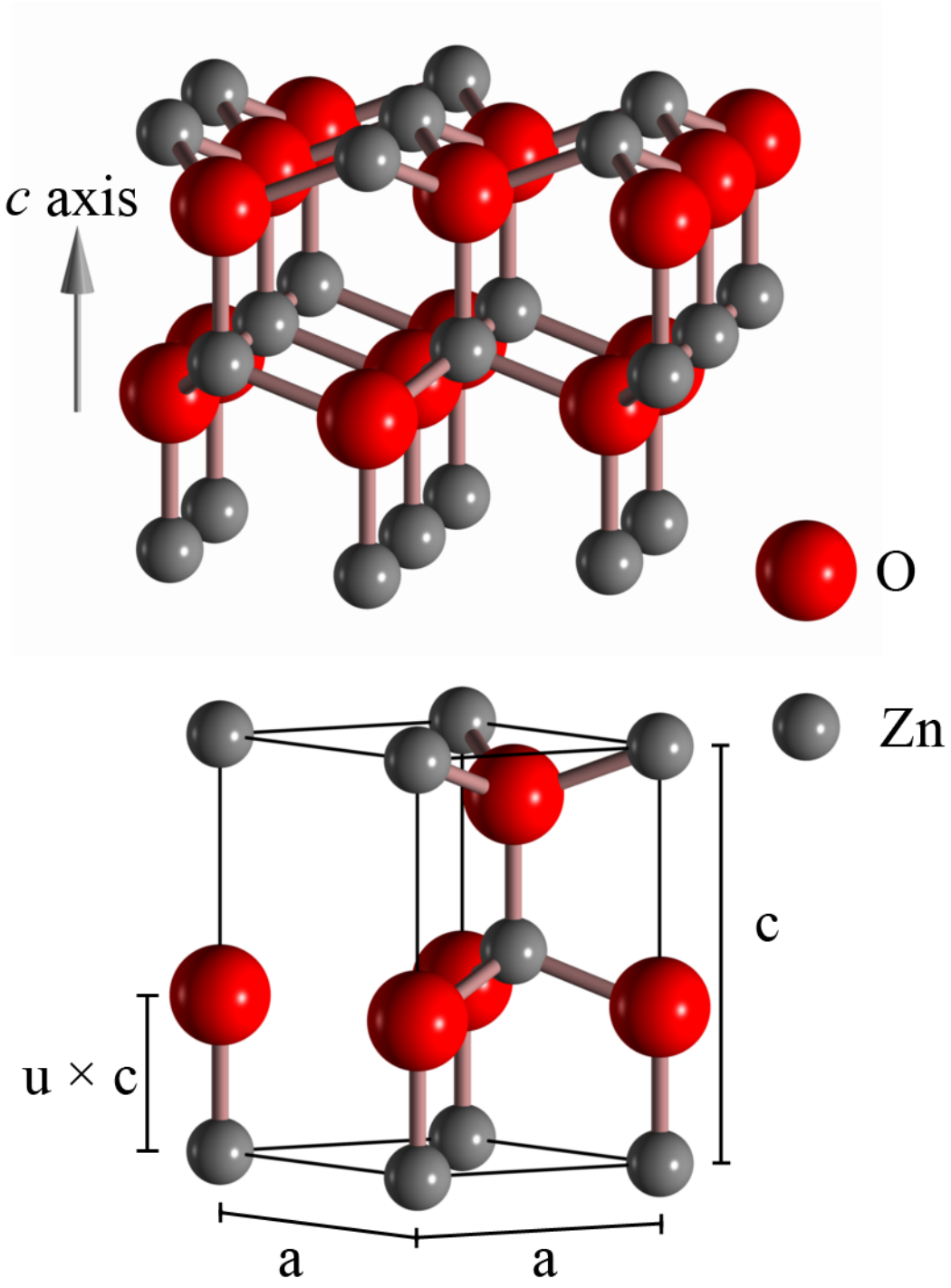

Figure 1.3: Top: A section of a wurtzite ZnO crystal lattice. Bottom: The unit cell lattice parameters for wurtzite ZnO.

studies found that annealing ZnO crystals in a hydrogen ambient increased their electrical conductivity. However, their conclusions were somewhat different from each other. Mollwo considered that the reduction of surface ZnO by hydrogen left elemental zinc to diffuse into the crystal and act as donor centers. Thomas and Lander reached a different conclusion upon further studies of ZnO. They concluded that hydrogen diffuses into the ZnO crystal lattice and is directly responsible for producing donors. They suspected that hydrogen combined with an oxygen ion, and the resulting OH^- center could be easily ionized.

In addition to the electrical conductivity, both research groups determined the diffusion rate of hydrogen into ZnO crystals at various temperatures. From these data they determined an activation energy for hydrogen diffusion. Mollwo determined the activation energy to be 1.12 eV while Thomas and Lander determined the value to be 0.91 eV.

1.2.2 Recent studies of hydrogen in zinc oxide

The primary motivation for this work came from the theoretical calculations of Van de Walle (2000). In his work, he calculated the formation energies and charge states of hydrogen in various locations in the wurtzite ZnO crystal lattice. It was found that the configurations with the lowest formation energies were all donor sites. The donor with the lowest formation energy was located at the $BC_\perp$ location with a formation energy of -1.84 eV. However, more recent calculations from Limpijumnong and Zhang (2005) revealed that the $BC_\parallel$ has the lowest formation energy (Tbl. 1.1).

Around the time of Van de Walle's work, it was thought that ZnO was always grown *n*-type due to native defects [Look *et al.* (1999)]. It had been shown by this time that the most common native defects were interstitial zinc and oxygen vacancies.

Site	ΔE (eV)	$\tilde{\omega}_{Har}$ (cm^{-1})	$\tilde{\omega}_{AC}$ (cm^{-1})	$\omega\,(\tilde{\omega})$ (cm^{-1})	Measured ω (cm^{-1})
$BC_{\parallel}$	0.00	3659	-282	3475 (3377)	3611[a]
$BC_{\perp}$	0.15	3706	-285	3519 (3421)	
$AB_{O,\parallel}$	0.17	3370	-352	3116 (3018)	3326[b]
$AB_{O,\perp}$	0.14	3379	-323	3154 (3056)	
H_2O	-	3815	-257	3657 (3559)	3657

Table 1.1: Calculated formation energies (relative to $BC_{\parallel}$) for hydrogen in ZnO, where $\tilde{\omega}_{Har}$, $\tilde{\omega}_{AC}$, and $\tilde{\omega}$ are the calculated harmonic terms, anharmonic terms, and net vibrational frequency for hydrogen in ZnO, respectively. The values of $\tilde{\omega}$ were offset by the difference between measured and calculated values for a free H_2O molecule, resulting in ω [Limpijumnong and Zhang (2005)]. See Fig. 1.4 for corresponding locations of hydrogen in ZnO.

[a] Lavrov *et al.* (2002)
[b] McCluskey *et al.* (2002)

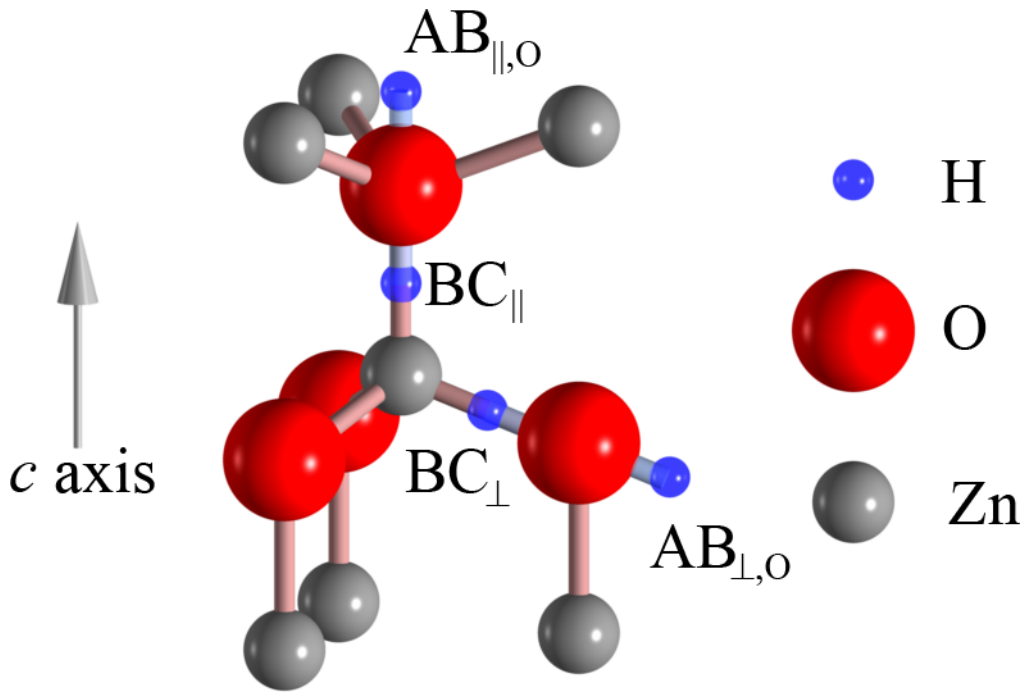

Figure 1.4: ZnO structure showing four possible locations where hydrogen may reside.

Both are deep donors [Janotti and Van de Walle (2006)], so neither one can explain the high conductivity of the crystals. In light of these revelations, the n-type conductivity must be due to defect impurities inadvertently incorporated into the crystal during growth. Van de Walle's work showed that hydrogen is an excellent candidate for such a defect.

Shortly after Van de Walle's calculations were published, work began on testing the predictions. Some of the first work was performed using positive muon implantation. Positive muons diffuse and interact in much the same way as protons do within a crystal lattice. At low temperatures, the muon can even capture an electron and form muonium, an exotic atom. In this case, muonium simulates hydrogen rather well. The benefit to using muonium is increased sensitivity in detection techniques over those employed for hydrogen. The technique essentially allows for the detection of individual muonium atoms as they decay. From the gathered data, one can determine the characteristics of the muonium site as well as the electrical characteristics of the muonium atom. The results showed that implanted muonium was in a shallow donor state in ZnO [Cox *et al.* (2001); Gil *et al.* (2001)]. The conclusion is that hydrogen in ZnO should also be in a shallow donor state.

Further studies involving temperature dependent Hall measurements revealed two donor levels, labeled D1 and D2, with respective activation energies of 35 meV and 66 meV [Hofman *et al.* (2002)]. It was also shown that the concentrations of these two donors were $(6 \pm 2) \times 10^{16}$ cm^{-3} and $(4 \pm 2) \times 10^{16}$ cm^{-3}, respectively. Confirmation was achieved with electron paramagnetic (EPR) measurements that showed a total carrier concentration of $(1 \pm 0.2) \times 10^{17}$, in good agreement with the results from the Hall measurements. In an attempt to determine the chemical nature of the donor, electron nuclear double resonance was employed (ENDOR). The results, in correlation

with EPR and Hall measurements, showed that hydrogen was the likely cause for the D1 donor [Hofman *et al.* (2002)].

1.3 The effects of oxygen vacancies and zinc interstitials on the conductivity of ZnO

For some time there was speculation that oxygen vacancies and zinc interstitials were responsible for the high electron carrier concentration of ZnO [Look *et al.* (1999)]. Calculations by Janotti and Van de Walle (2006) have shown that these native defects can be ruled out for as-grown ZnO. The results of their work show that oxygen is a deep donor with a high formation energy in *n*-type ZnO. Their results also show that zinc interstitials are shallow donors, but they too have a high formation energy. In addition, zinc interstitials are unstable in ZnO as they easily diffuse through the lattice. Another candidate for the *n*-type conductivity of ZnO was the Zn antisite. However, this defect has been shown to have an even higher formation energy than the zinc interstitial.

1.3.1 Oxygen vacancies

Janotti and Van de Walle (2006) calculated that the oxygen vacancy in *n*-type ZnO has a large formation energy (3.5 eV). Also shown were three charge states for the oxygen vacancy, the neutral, 1+, and 2+ states. The relaxation of the Zn atoms makes the 1+ state unstable. Their calculations show that the formation energy decreases under *p*-type conditions, making oxygen vacancies compensating defects for *p*-type ZnO.

1.3.2 Zinc interstitials

Similar results came from the calculations on zinc interstitials. The formation energy is even higher than that of the oxygen vacancy. While zinc interstitials do diffuse quickly through the ZnO crystal lattice, there is a stable position at the octahedral site. Even though this position is stable, the high formation energy decreases the likelihood of zinc interstitials.

1.3.3 Zinc antisites

Zinc on an oxygen lattice point is expected to be a shallow donor. The calculations showed that this configuration had a higher formation energy than the zinc interstitial. Once formed, the zinc antisite is more stable under thermal effects than the zinc interstitial, making it harder to remove by annealing. Zinc antisites could play a role under conditions of irradiation.

1.4 Hydrogen defects in other semiconductors

Hydrogen has been well studied in many other semiconductors. In nearly every case, the introduction of hydrogen has dramatic effects on the electrical properties of the material. In some cases, such as high-purity germanium detectors, these effects can be useful. In others, hydrogen contamination can be detrimental to the intended operation of a device. In both situations, it is beneficial to understand the process by which hydrogen is introduced into the material as well as the effects it has on the material's properties.

Some of the most dramatic effects were discovered in the III-V semiconductors, where hydrogen neutralizes donor impurities in n-type materials and acceptor impurities in p-type materials [Chevallier *et al.* (1991)]. In GaN:Mg, for example, hydrogen

effectively passivates Mg acceptors, rendering the material semi-insulating [Brandt *et al.* (1994); Götz *et al.* (1996)]. The sample must be annealed in order to dissociate Mg-H complexes and obtain p-type conductivity. This is not the behavior that hydrogen is expected to have in ZnO, where its theorized to be a shallow donor.

Hydrogen-related effects were studied at great length in GaAs doped with various donor or acceptor substitutional impurities. In the cases studied, hydrogen bonds with the impurity or to an atom with which the impurity was bonded [Pearton *et al.* (1986); Pan *et al.* (1987b); Chevallier and Aucouturier (1988a); Nandhra *et al.* (1988)]. In so doing, the hydrogen neutralizes the impurity defect, whether that defect is a donor or an acceptor.

Hydrogen can also passivate electronic states created by dislocations, grain boundaries, and surfaces. Such effects have been seen in crystalline silicon [Pankove (1991)]. Extended defects contain dangling bonds which have a dramatic effect on the electrical characteristics of the material. For example, dislocations due to lattice mismatch in crystalline silicon grown on sapphire strongly affect the photovoltage when light strikes the defect. This is due to the effects the dislocation has on the photo-generated carriers. Upon hydrogenation, these defects no longer affect the photovoltage.

Grain boundaries also have a strong effect on the photoconductivity of crystalline silicon. A grain boundary behaves as two back-to-back Schottky barriers. One of these barriers will be reversed-biased to the driving voltage, hindering the flow of electrons or holes across the boundary. Hydrogenation passivates the dangling bonds responsible for this effect.

The termination of a regular crystal lattice at the surface is the greatest defect. In a p-n junction, the surface allows for a large leakage current for a reverse bias across the diode. It has been shown that hydrogenation of the surface of these diodes reduces

the leakage current dramatically. It is expected that the widening of the bandgap at the surface due to hydrogen has the effect of reflecting charge carriers, preventing surface leakage current across the *p*-*n* junction.

1.4.1 Hydrogen in gallium arsenide

Donor neutralization

The introduction of hydrogen into *n*-type GaAs:Si results in a decrease in donors and an increase in carrier mobility [Jalil *et al.* (1986); Pan *et al.* (1987a)]. It had been proposed that the decrease in active silicon donors was a result of neutral Si-H complexes forming in the region of hydrogen in-diffusion [Chevallier *et al.* (1985)]. The results of Jalil *et al.* (1986) confirmed this model.

The hydrogen complex in GaAs:Si was first observed by Jalil *et al.* (1987). The vibrational frequency was observed, at liquid-helium temperatures, to be 896.8 cm^{-1} and shifted to 641.5 cm^{-1} for deuterium. Further studies showed that another hydrogen related vibrational mode was observed at 1717.2 cm^{-1}. An isotopic shift in this frequency was also observed between ^{28}Si and ^{29}Si, suggesting that these are Si-H related vibrational modes. The two hydrogen related vibrational modes at 896.8 cm^{-1} and 1717.2 cm^{-1} can be attributed to the Si-H wag and stretch modes, respectively. This is strong evidence that the hydrogen is directly responsible for the passivation of the Si donors.

Acceptor neutralization

Acceptor neutralization by hydrogen in *p*-type III-V semiconductors was first shown in GaAs:Zn [Johnson *et al.* (1986b)]. Further evidence of acceptor neutralization was also shown for beryllium [Nandhra *et al.* (1988)], carbon [Pan *et al.* (1987b)],

and silicon [Chevallier *et al.* (1988b)]. However, unlike hydrogen in *n*-type GaAs:Si, hydrogen in *p*-type GaAs:Zn [Pajot *et al.* (1987)] and GaAs:Be [Nandhra *et al.* (1988)] has been shown to directly bond with As, rather than the acceptor impurity.

1.4.2 Hydrogen in crystalline silicon

Hydrogen passivation of dangling bonds

In the work of Gray and Brown (1966), a reduction in the density of states was observed near the interface between SiO_2 and Si when oxidation was performed with oxygen containing water. Researches attributed this effect to hydrogen passivation of the dangling bonds at the interface layer. As discussed by Pankove (1991), these effects are also seen for dangling bonds on the surface, in grain boundaries, and dislocations.

Acceptor passivation

In *p*-type Si:B, it was found that hydrogen results in the reduction of hole carriers [Sah *et al.* (1983)]. They demonstrated that hydrogen could diffuse into the crystal, neutralizing boron acceptors up to a depth of 2 μm [Pankove *et al.* (1984)]. Upon annealing at temperatures above 200 °C, it was found that the hydrogen complex was broken up, decreasing the resistance to as-grown values [Sah *et al.* (1983)]. Since it had been established that hydrogen passivates dangling bonds in crystalline silicon, it was thought that hydrogen passivates boron acceptors by binding to the dangling bond created when boron substitutes for a silicon atom [Pankove *et al.* (1984)]. Later calculations showed that a form of bond sharing occurs where hydrogen bonds to both silicon and boron in Si:B [Estreicher *et al.* (1989)], confirming results showing vibrational modes likely caused by hydrogen-acceptor bonds in Si [Stavola *et al.* (1987)].

Donor passivation

One of the first experiments to show hydrogen passivation of shallow donors was Johnson (1986a) in a study on n-type Si:P. Not only did the resistivity increase upon hydrogenation, but the mobility increased as well. The increase in mobility was attributed to a decrease of ionized impurities, neutralized as a result of hydrogen being introduced to the crystal. Empirical calculations performed in the same study showed that hydrogen preferred to bond with silicon in an "antibonding" position, opposite to the phosphorus impurity. Calculations using an *ab initio* method, performed by Chang and Chadi (1988), agreed with the empirical calculations.

Spectroscopic evidence confirmed the theoretical predictions [Bergman *et al.* (1988)]. After hydrogen-plasma treatment of n-type silicon, the samples exhibited absorption bands at 1555, 1561, and 1562 cm^{-1} for P, As, and Sb doped silicon, respectively. The weak dependence on donor species indicates that hydrogen binds to silicon, in a position removed from the donor atom, as suggested by the calculations made by Chang and Chadi (1988).

Chapter 2
THEORY OF VIBRATIONAL MODES

2.1 Introduction

While our initial work focused on hydrogen in as-grown ZnO, our later work focused on growing nitrogen doped ZnO. During this later work hydrogen was used as a probe where it could form an N-H bond. In both cases, hydrogen forms a bond with a native or impurity atom within the ZnO crystal lattice. To correctly interpret infrared absorption spectra, it is important to understand the effects of introducing a light atom, such as hydrogen, into a crystal lattice. Not only does an impurity atom modify the natural frequencies of the lattice, it can also introduce a vibrational mode with a frequency higher than the phonon modes of a perfect crystal. The new mode is known as a local vibrational mode (LVM).

2.2 The harmonic oscillator

2.2.1 The classical harmonic oscillator

Before we can discuss how defects affect the vibrational properties of a crystal lattice, we must first describe the vibrational properties of a pure lattice. To begin, we will start with the classical description of a particle constrained to one dimension in a parabolic potential, known as the simple harmonic oscillator. In this system, the potential is given by

$$V(x) = V_o + \frac{1}{2}kx^2, \tag{2.1}$$

where x is the particle's displacement from equilibrium and k is given by

$$k = \left.\frac{d^2V}{dx^2}\right|_0 . \tag{2.2}$$

The force on the particle at any given position in the harmonic potential can be derived as

$$F = -\frac{dV}{dx} = -kx, \tag{2.3}$$

a restatement of Hooke's Law, where k is referred to as the spring constant. The solution to this differential equation is

$$x(t) = A\cos(\omega t + \phi), \tag{2.4}$$

where both A and ϕ are constants determined by the initial conditions. The oscillation frequency ω is given by:

$$\omega = \sqrt{\frac{k}{m}}, \tag{2.5}$$

where m is the mass of the particle.

The kinetic energy of this system is given by

$$T = \frac{1}{2}m\left(\frac{dx}{dt}\right)^2 = \frac{p^2}{2m}, \tag{2.6}$$

where p is the momentum of the particle. The total energy is given by

$$E = T + V = \frac{p^2}{2m} + \frac{1}{2}m\omega^2x^2. \tag{2.7}$$

Substitution of Eq. (2.4) into Eq. (2.7) yields

$$E = \frac{1}{2} m\omega^2 A^2, \tag{2.8}$$

where A is the amplitude of the oscillation.

2.2.2 The quantum harmonic oscillator

While Eq. (2.8) is valid for the classical harmonic oscillator, it does not satisfy the quantized energy requirements that govern particles in the quantum domain, such as atoms in a crystal lattice. To solve the quantum harmonic oscillator problem, we must turn to quantum theory.

Following the discussion in Cohen-Tannoudji (1977), we replace x and p from Eq. (2.7) with the observables X and P. These quantities satisfy the Heisenberg uncertainty relation which states

$$\Delta X \cdot \Delta P \gtrsim \hbar, \tag{2.9}$$

where ΔX is the uncertainty of the particle's position and ΔP is the uncertainty of the particle's momentum. The Heisenberg relation states that the position and momentum cannot be simultaneously defined to an arbitrary degree of accuracy. For instance, as the accuracy of the position is increased (ΔX decreased), the accuracy of the momentum must decrease such that Eq. (2.9) remains satisfied. The following holds true for the X and P operators:

$$[X, P] = i\hbar, \tag{2.10}$$

where $[A, B]$ is known as the commutator and is defined as

$$[A, B] = AB - BA. \tag{2.11}$$

If $[A, B] = 0$, then A and B are said to commute. As a result, both observables can be determined simultaneously with arbitrary accuracy. In the case of Eq. (2.10), X and P do not commute, a consequence of which is the Heisenberg relation.

The Hamiltonian operator can be obtained from Eq. (2.7) by simple substitution previously mentioned:

$$H = \frac{P^2}{2m} + \frac{1}{2}m\omega^2 X^2. \tag{2.12}$$

For simplicity, X and P are replaced with dimensionless operators:

$$\hat{X} = \sqrt{\frac{m\omega}{\hbar}}X \tag{2.13}$$

and

$$\hat{P} = \frac{1}{\sqrt{m\hbar\omega}}P, \tag{2.14}$$

resulting in a unit-less Hamiltonian,

$$\hat{H} = \frac{1}{2}(\hat{X}^2 + \hat{P}^2). \tag{2.15}$$

It can be shown that the following relation between H and $\hat{H}$ exists:

$$H = \hbar\omega\hat{H}. \tag{2.16}$$

The next step is to find the solutions of the eigenvalue equation

$$\hat{H}\left|\psi_n^i\right\rangle = \varepsilon_n \left|\psi_n^i\right\rangle, \tag{2.17}$$

where the eigenvalues ε_n are dimensionless. The index n denotes the energy level and the index i is used to denote orthogonal sets of eigenvectors associated with the same eigenvalue n.

Continuing to follow Cohen-Tannoudji, two new operators are defined

$$a = \frac{1}{\sqrt{2}}(\hat{X} + i\hat{P}) \tag{2.18}$$

$$a^\dagger = \frac{1}{\sqrt{2}}(\hat{X} - i\hat{P}). \tag{2.19}$$

The dimensionless Hamiltonian can be written

$$\hat{H} = a^\dagger a + \frac{1}{2} = \frac{1}{2}(\hat{X} - i\hat{P})(\hat{X} + i\hat{P}) + \frac{1}{2}. \tag{2.20}$$

It can also be shown that

$$\hat{H} = aa^\dagger - \frac{1}{2}. \tag{2.21}$$

Two commutation relations can be derived

$$[\hat{H}, a] = -a \tag{2.22}$$

and

$$[\hat{H}, a^\dagger] = a^\dagger. \tag{2.23}$$

By defining

$$N = a^\dagger a, \tag{2.24}$$

we can write Eq. (2.20) as

$$\hat{H} = N + \frac{1}{2}. \tag{2.25}$$

Application of Eq. (2.24) to a wave-function results in

$$N \left|\psi_n^i\right\rangle = n \left|\psi_n^i\right\rangle. \tag{2.26}$$

When applied to a wave-function, Eq. (2.22) yields

$$\hat{H} a \left|\psi_n^i\right\rangle - a\hat{H} \left|\psi_n^i\right\rangle = -a \left|\psi_n^i\right\rangle. \tag{2.27}$$

Inserting Eq. (2.17) we obtain

$$\hat{H} a \left|\psi_n^i\right\rangle = (\varepsilon_n - 1) a \left|\psi_n^i\right\rangle. \tag{2.28}$$

According to Eq. (2.25) and Eq. (2.26), $\varepsilon_n = n + \frac{1}{2}$. In this comparison we can see that the operator a simply lowers the value of n by 1. It can be similarly shown that $a^\dagger$ raises the value of n by 1 and thus the operators a and $a^\dagger$ are called the lowering and raising operator, respectively.

If we replace the dimensionless operators with their observable counterparts X and P, we obtain the discrete energy levels of the quantum harmonic oscillator. Instead of Eq. (2.28), we now have

$$Ha \left|\psi_n^i\right\rangle = (E_n - \hbar\omega) a \left|\psi_n^i\right\rangle = (n + \frac{1}{2} - 1)\hbar\omega a \left|\psi_n^i\right\rangle, \tag{2.29}$$

where the a operator is shown to decrease the energy by the discrete amount $\hbar\omega$. The lowering operator will reach a limit at the ground state such that

$$a\left|\psi_0^i\right\rangle = 0. \tag{2.30}$$

As such, the ground state's energy is given by

$$H\left|\psi_n^i\right\rangle = (a^\dagger a\omega + \frac{1}{2}\hbar\omega)\left|\psi_0^i\right\rangle = \frac{1}{2}\hbar\omega\left|\psi_0^i\right\rangle. \tag{2.31}$$

From this we can deduce that the quantized energies of the quantum harmonic oscillator are

$$E = (n + \frac{1}{2})\hbar\omega. \tag{2.32}$$

The ground state wave function can be solved by use of the lowering operator to set up the following differential equation:

$$a\left|\psi_0^i\right\rangle = 0,$$

$$\frac{1}{\sqrt{2}}\left[\sqrt{\frac{m\omega}{\hbar}}X + \frac{i}{\sqrt{m\hbar\omega}}P\right]\left|\psi_0^i\right\rangle = 0,$$

so that the equation to solve in one dimension is

$$\left(\frac{m\omega}{\hbar}x + \frac{d}{dx}\right)\psi_0^i(x) = 0. \tag{2.33}$$

The solution of Eq. (2.33) is

$$\psi_0^i(x) = ce^{-\frac{1}{2}\frac{m\omega}{\hbar}x^2}, \tag{2.34}$$

where c is the integration constant to be determined by normalizing to unity. From here it can be further shown that the wave function for each state of the quantum harmonic oscillator is

$$\left|\psi_n^i\right\rangle = \frac{1}{\sqrt{n}}(a^\dagger)^n \left|\psi_n^i\right\rangle . \tag{2.35}$$

This can easily be applied to multiple dimensions in which the wave function is written

$$|\Psi_n\rangle = \psi_{n_x}(x)\psi_{n_y}(y)\psi_{n_z}(z). \tag{2.36}$$

The Hamiltonian and the energy eigenvalues of the multidimensional system are

$$H = \frac{P^2}{2m} + \frac{1}{2}m\left(\omega_x^2 x^2 + \omega_y^2 y^2 + \omega_z^2 z^2\right) \tag{2.37}$$

and

$$E = \varepsilon_x + \varepsilon_y + \varepsilon_z = \hbar\omega_x\left(n_x + \frac{1}{2}\right) + \hbar\omega_y\left(n_y + \frac{1}{2}\right) + \hbar\omega_z\left(n_z + \frac{1}{2}\right). \tag{2.38}$$

2.2.3 Harmonic approximation of a general potential

The harmonic potential does not describe the exact potential of an atom in a crystal lattice. However, we can still use it as an approximation. For example, take the general potential $V(x)$ which has a stable equilibrium at $V(0)$, and expand it using the Taylor expansion.

$$V(x) = V_0 + \left.\frac{dV}{dx}\right|_{x=0} x + \left.\frac{1}{2!}\frac{d^2V}{dx^2}\right|_{x=0} x^2 + \left.\frac{1}{3!}\frac{d^3V}{dx^3}\right|_{x=0} x^3 + ... \tag{2.39}$$

The first term is simply a constant and does not affect the dynamics of the system. In the second term, $\left.\frac{dV}{dx}\right|_{x=0}$ is zero, since that is a condition of a stable equilibrium. The

third term is the harmonic term, which is the focus of the treatments in the previous two sections. Beyond the harmonic term are the higher ordered terms. If we set the condition that the displacement x is to remain small, we can see that the higher ordered terms have very little effect compared to the harmonic term. Under these conditions we can use the harmonic oscillator as an approximation for any general potential that can be expanded in this way. This is the justification for using the harmonic oscillator as an approximation for the vibrational properties of materials. Those details not explained by the harmonic oscillator are classified as anharmonic effects and are discussed in Sec. 2.4.3.

2.3 Vibrations of crystals

A crystal is an array of atoms bonded together in an ordered manner that is repeated in three dimensions. Each atom has a stable equilibrium position where the net force from every other atom in the crystal equals zero. If an atom is perturbed from this equilibrium position, the net force reacts in such a way as to restore the atom to its equilibrium position. It is this restoring force, caused by ionic attraction/repulsion or covalent bonds, that is the mechanism responsible for vibrations in solids. In this section, I will discuss the vibrational properties of one-dimensional crystals constituted of atoms of identical mass (monatomic linear chain) and one-dimensional crystals made up of atoms of two different masses (diatomic linear chain).

2.3.1 Monatomic linear chain

In this section I will follow the treatment given in Kittel (2005). The easiest scenario to model is that of a linear chain of atoms, all of the same mass (see Fig. 2.1). While not a model of a three dimensional crystal, the linear chain still can

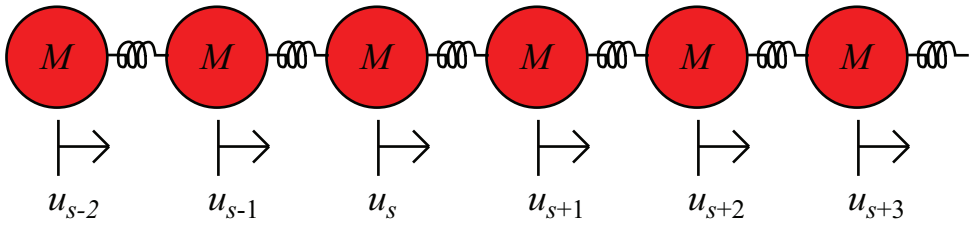

Figure 2.1: A monatomic linear chain of atoms with mass M.

be used to approximately model lattice vibrations propagating along the [100], [110], and [111] directions in a cubic crystal. In this section, the particular analog will be a simple cubic crystal with a one-atom basis.

For this model, the net restoring force is a linear function of an atom's displacement relative to its neighboring atoms. The displacement of atom s from its equilibrium position is denoted u_s. The force on atom s from the displacement of atom $s+p$ is proportional to the difference of their displacements, $u_{s+p} - u_s$. If only nearest neighbor ($p = \pm 1$) interactions are considered, then the total force on atom s from its neighbors is

$$F_s = C\left(u_{s+1} - u_s\right) + C\left(u_{s-1} - u_s\right), \tag{2.40}$$

where C is the force constant between nearest-neighbor atoms.

The equation of motion for atom s is

$$M\frac{d^2u_s}{dt^2} = C\left(u_{s+1} + u_{s-1} - 2u_s\right), \tag{2.41}$$

where M is the mass of the atom. Since the atoms oscillate around their equilibrium position, normal-mode solutions to Eq. (2.41) have the time dependence $\exp\left(-i\omega t\right)$. Then Eq. (2.41) becomes

$$-M\omega^2 u_s = C\left(u_{s+1} + u_{s-1} - 2u_s\right). \tag{2.42}$$

Considering a traveling wave with an amplitude u, we can write solutions in the form of

$$u_s = u\left\{\exp\left(isKa\right)\right\}, \tag{2.43}$$

where a is the spacing between atoms and K is the wavevector.

Inserting Eq. (2.43) into Eq. (2.42) yields

$$-\omega^2 Mu\exp\left(isKa\right) = Cu\left\{\exp\left[i\left(s+1\right)Ka\right] + \exp\left[i\left(s-1\right)Ka\right] - 2\exp\left(isKa\right)\right\}, \tag{2.44}$$

from which we can simplify to

$$\omega^2 M = -C\left[\exp\left(iKa\right) + \exp\left(-iKa\right) - 2\right]. \tag{2.45}$$

Using the identity $2\cos Ka = \exp\left(iKa\right) + \exp\left(-iKa\right)$, we obtain the dispersion relation $\omega\left(K\right)$.

$$\omega\left(K\right) = \left[\left(2\frac{C}{M}\right)\left(1-\cos Ka\right)\right]^{\frac{1}{2}}. \tag{2.46}$$

The more common form of this can be achieved with the trigonometric identity $1 - \cos Ka = 2\sin^2\frac{Ka}{2}$ so that Eq. (2.46) becomes

$$\omega\left(K\right) = 2\sqrt{\frac{C}{M}}\left|\sin\frac{Ka}{2}\right|. \tag{2.47}$$

A plot of the dispersion relation for a monatomic linear chain of atoms is shown in Fig. 2.2.

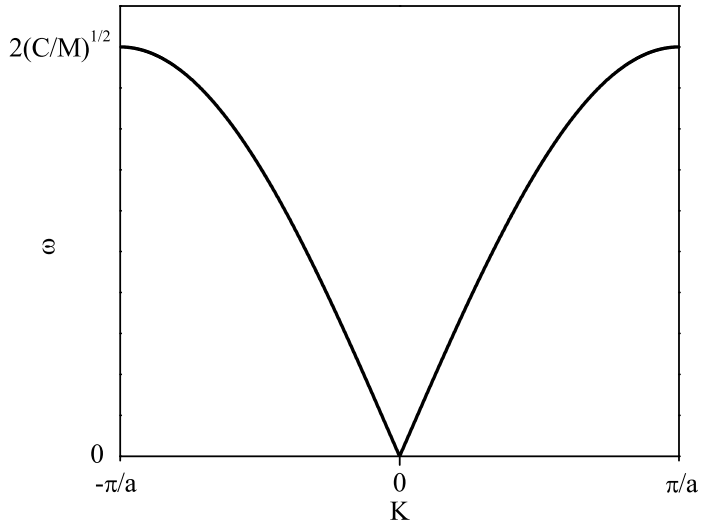

Figure 2.2: A plot of the dispersion relation for a monatomic linear chain of atoms.

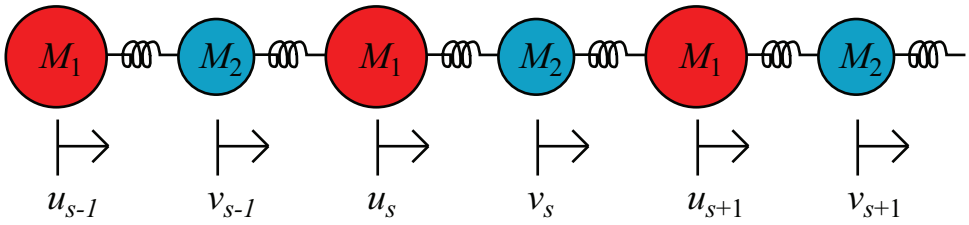

Figure 2.3: A diatomic linear chain of atoms with mass M_1 and M_2.

2.3.2 Diatomic linear chain

Continuing the treatment of Kittel (2005), we now move on to a linear chain of atoms in which the masses of the atoms are not all the same. The simplest such model is a linear chain with two types of atoms, with different masses M_1 and M_2, that are arranged in an alternating pattern (see Fig. 2.3). The atoms of mass M_1 and M_2 are located at positions u_s and v_s, respectively. Again, only nearest neighbor interactions

are considered. For example, the atom at position v_1 has mass M_2 and interacts only with the atoms of mass M_1 located at positions u_1 and u_2. The distances between like atoms; i.e., the length of each unit cell along the direction of propagation, is a. Following a similar treatment as for the monatomic linear chain, we write the equations of motion as

$$\begin{aligned} M_1 \tfrac{d^2 u_s}{dt^2} &= C\left(v_s + v_{s-1} - 2u_s\right) \\ M_2 \tfrac{d^2 v_s}{dt^2} &= C\left(u_{s+1} + u_s - 2v_s\right), \end{aligned} \tag{2.48}$$

where s now represents the unit cell within which the two atoms reside.

The solutions for the atoms on alternate planes will still take the form of a propagating wave. However, each atom will experience a different amplitude of oscillation:

$$\begin{aligned} u_s &= u \exp\left(isKa\right) \exp\left(-i\omega t\right) \\ v_s &= v \exp\left(isKa\right) \exp\left(-i\omega t\right). \end{aligned} \tag{2.49}$$

Inserting the solutions, Eq. 2.49, into Eq. (2.48), we have

$$\begin{aligned} -\omega^2 M_1 u &= Cv\left[1 + \exp\left(-iKa\right)\right] - 2Cu \\ -\omega^2 M_2 v &= Cu\left[1 + \exp\left(iKa\right)\right] - 2Cv. \end{aligned} \tag{2.50}$$

This system of linear equations only has nontrivial solution if

$$\begin{vmatrix} 2C - M_1\omega^2 & -C\left[1 + \exp\left(-iKa\right)\right] \\ -C\left[1 + \exp\left(iKa\right)\right] & 2C - M_2\omega^2 \end{vmatrix} = 0 \tag{2.51}$$

or

$$M_1 M_2 \omega^4 - 2C\left(M_1 + M_2\right)\omega^2 + 2C^2\left(1 - \cos Ka\right) = 0. \tag{2.52}$$

Solving for ω^2 we obtain

$$\omega^2 = C\left(\frac{1}{M_1}+\frac{1}{M_2}\right) \pm C\sqrt{\left(\frac{1}{M_1}+\frac{1}{M_2}\right)^2 - \frac{4}{M_1 M_2}\sin^2\left(\frac{Ka}{2}\right)}. \tag{2.53}$$

Analysis for the limiting cases $Ka \ll 1$ and $Ka = \pm\pi$ at the Brillouin zone edge is useful. For small Ka we have $Ka \cong 1 - \frac{1}{2}K^2a^2 + ...$, the roots of which are

$$\omega^2 \cong 2C\left(\frac{1}{M_1}+\frac{1}{M_2}\right); \tag{2.54}$$

$$\omega^2 \cong \frac{\frac{1}{2}C}{M_1+M_2}K^2a^2. \tag{2.55}$$

In this limit, Eqs. (2.54) and (2.55) represent the dispersion relations for the optical and acoustical phonon branches, respectively. For $K = \pm\frac{\pi}{a}$, the roots are

$$\omega^2 = \frac{2C}{M_1}; \tag{2.56}$$

$$\omega^2 = \frac{2C}{M_2}. \tag{2.57}$$

A plot of the dispersion relation for a diatomic linear chain of atoms is shown in Fig. 2.4.

For the optical branch, at $K = 0$ we find that $\frac{u}{v} = -\frac{M_2}{M_1}$. This shows that the two different types of atoms have opposing velocities for frequencies in the optical branch. Furthermore, if these two types of atoms carry opposite charge, then these modes may be excited by interactions with the electric field of a light wave. For this reason, the optical branch is given its name.

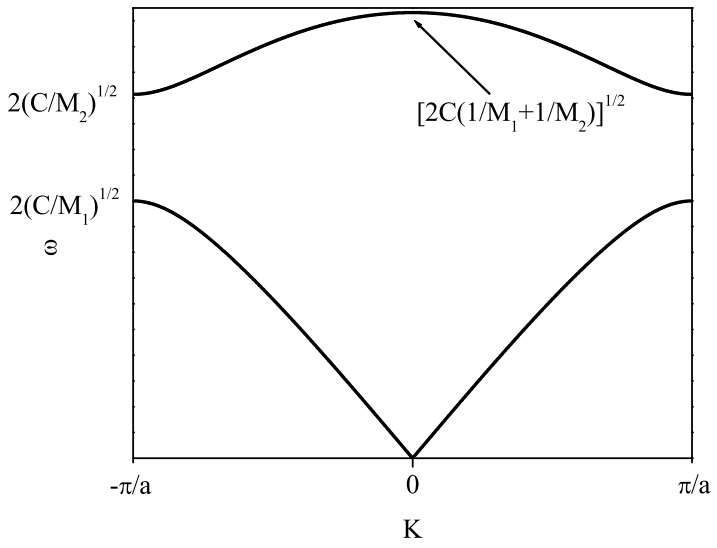

Figure 2.4: The dispersion relation for a diatomic chain of atoms with $M_1 > M_2$. Both the optical branch (top) and acoustical branch (bottom) are shown.

2.4 The local vibrational mode

If the translational symmetry of the crystal is broken by replacing one of the atoms with a new mass M_3, then the vibrational properties of the crystal are changed. By introducing an impurity, the vibrational frequencies of the crystal can be slightly altered or, if a large change in mass occurs, new modes can be introduced with frequencies in the gap region between the optical and acoustical phonon branches or at frequencies above the maximum phonon energy. These new modes are localized in both real and frequency space.

2.4.1 Numerical modeling of vibrational modes

Modeling gallium phosphide

From Eqs. (2.48) and (2.50), the equations of motion for a diatomic linear chain can be written:

$$\begin{aligned} -\omega^2 M_1 u_s &= C\left(v_s + v_{s-1} - 2u_s\right) \\ -\omega^2 M_2 v_s &= C\left(u_{s+1} + u_s - 2v_s\right). \end{aligned} \tag{2.58}$$

where u_s and v_s are the positions of the atoms of mass M_1 and M_2 in the sth unit cell, respectively. The solutions that we are interested in for these equations are the eigenvalues ω^2 and the corresponding eigenvectors u_s and v_s. In matrix form, the equations to be solved appear as [Barker and Sievers (1975)]

$$\begin{bmatrix} \frac{2C}{M_1}-\omega^2 & -\frac{C}{M_1} & 0 & 0 & \cdots & 0 & 0 & -\frac{C}{M_1} \\ -\frac{C}{M_2} & \frac{2C}{M_2}-\omega^2 & \frac{-C}{M_2} & 0 & \cdots & 0 & 0 & 0 \\ \vdots & \vdots & \vdots & \vdots & \ddots & \vdots & \vdots & \vdots \\ 0 & 0 & 0 & 0 & \cdots & -\frac{C}{M_1} & \frac{2C}{M_1}-\omega^2 & -\frac{C}{M_1} \\ -\frac{C}{M_2} & 0 & 0 & 0 & \cdots & 0 & -\frac{C}{M_2} & \frac{2C}{M_2}-\omega^2 \end{bmatrix} \begin{bmatrix} u_1 \\ v_1 \\ \vdots \\ u_N \\ v_N \end{bmatrix} = 0, \tag{2.59}$$

where N is the number of unit cells in the chain. The following examples will use the values $C = 0.87 \times 10^{15}$ dyne/cm, $M_1 = 70$ amu (^{70}Ga), and $M_2 = 31$ amu (^{31}P), simulated in a lattice of 512 atoms (256 unit cells). These values are representative of a GaP crystal.

The calculated density of states is shown in Fig. 2.5. The two branches are clearly visible in this calculation, the acoustical modes up to 205 cm^{-1} and the optical modes between 308 cm^{-1} and $\omega_{\mathrm{TO}} = 371$ cm^{-1}. There are no vibrational modes between

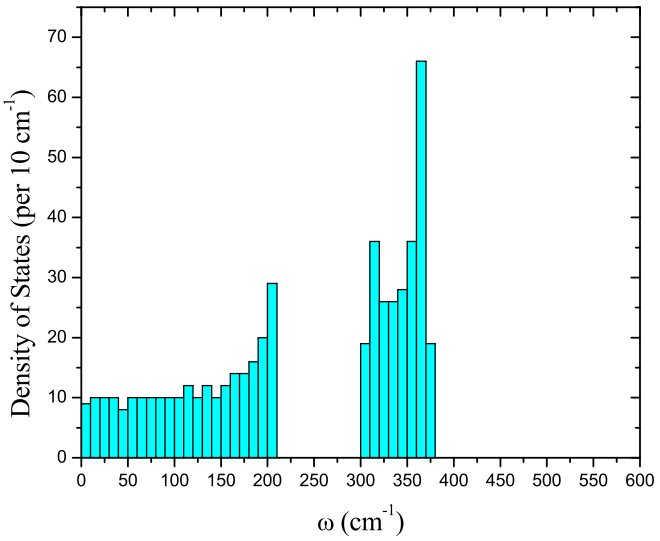

Figure 2.5: Histogram of the calculated density of states for GaP.

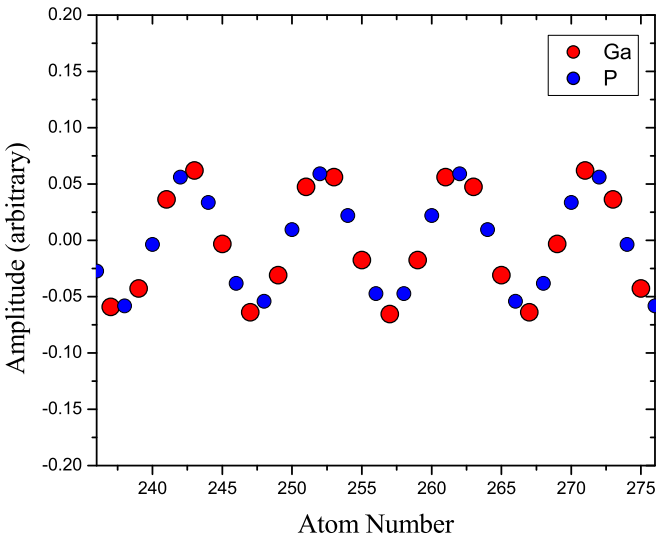

Figure 2.6: Vibrational amplitudes of atoms for an acoustical mode in GaP.

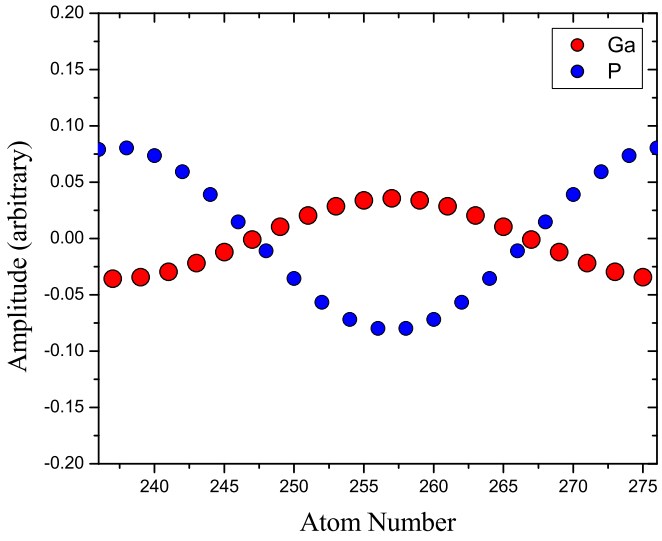

Figure 2.7: Vibrational amplitudes of atoms for an optical mode in GaP.

205 cm^{-1} and 308 cm^{-1}. The experimentally observed maximum for the transverse optical branch is $\omega_{\text{TO}} = 366\ \text{cm}^{-1}$.

The dramatic difference in oscillations between the acoustical mode and optical mode can be seen in Fig. 2.6 and Fig. 2.7, where the modes for $\omega = 108.2\ \text{cm}^{-1}$ and $\omega = 369.6\ \text{cm}^{-1}$ have been plotted, respectively.

The gap mode modeled in gallium phosphide

By replacing a mass M_2 with a heavier mass M_3, we break the perfect translational symmetry that was demonstrated previously. For this scenario, we use the same parameters as in the previous section with the substitution of atom number 256, a ^{31}P atom, with an atom of mass $M_3 = 62$ amu. The replacement of a single ^{31}P atom with an atom of heavier mass creates a vibrational state between the acoustical and optical phonon branches (Fig. 2.8). The gap mode is somewhat localized in both

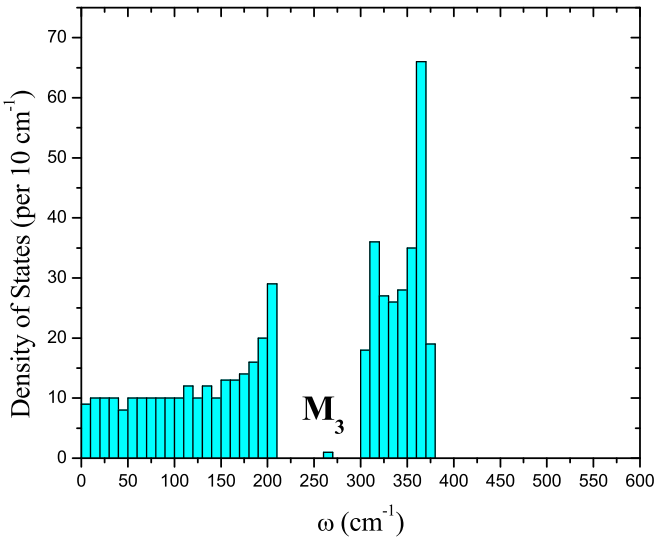

Figure 2.8: Histogram of the calculated density of states for GaP with a ^{31}P atom replaced with an atom of mass M_3 =62 amu. A gap mode is now visible.

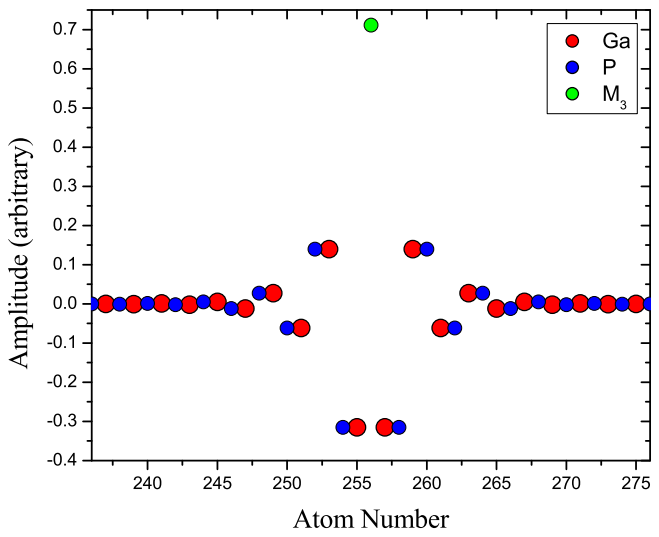

Figure 2.9: The calculated vibrational amplitudes for the gap mode in the GaP lattice with a substitutional impurity on a P site.

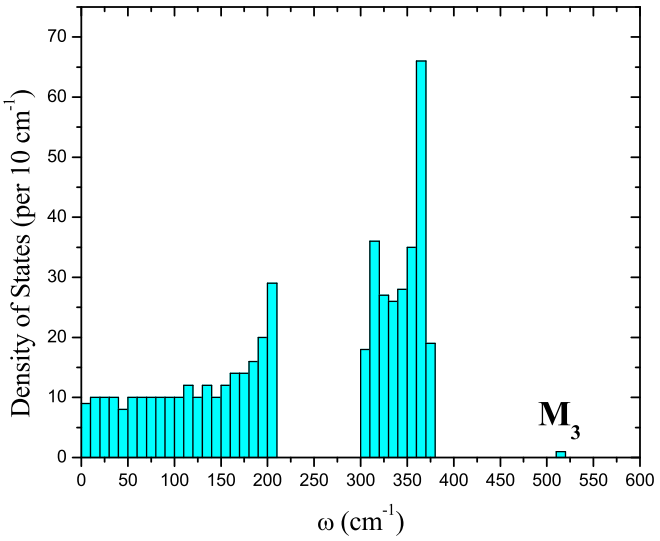

Figure 2.10: Histogram of the calculated density of states for GaP with a ^{31}P atom replaced with an atom of mass M_3 =12 amu. A local vibrational mode is now visible with frequency higher than ω_{TO}.

frequency space and real space, as can be seen in Fig. 2.9, where the mass M_3 perturbs only a few of its neighboring atoms.

Modeling of a local vibrational mode in gallium phosphide

If we instead replace the ^{31}P atom with an atom of light mass M_3 = 12 amu, a vibrational mode well above ω_{TO} is created (Fig. 2.10). This vibrational mode is highly localized in real space and frequency space, perturbing only a couple of atoms around the M_3 substitutional impurity (Fig. 2.11).

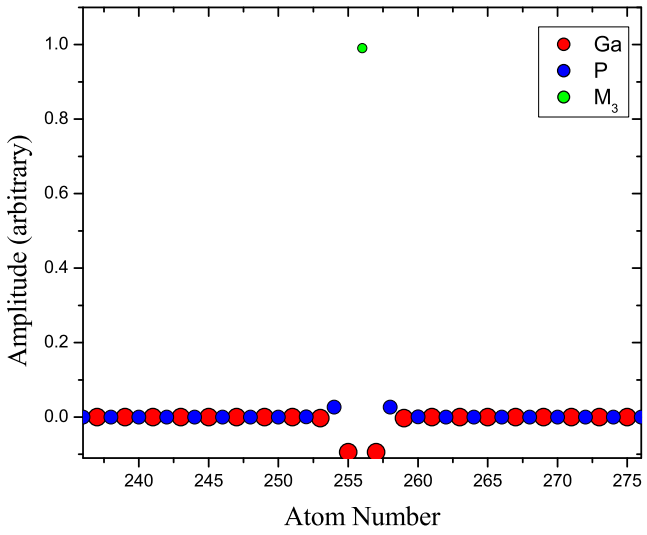

Figure 2.11: A highly localized vibrational mode created from the replacement of a ^{31}P atom with a lighter mass atom $M_3 = 12$ amu.

2.4.2 Modeling isotopic shifts in local vibrational modes

When observing LVMs, one often has the ability to narrow down what elements could be responsible for the impurity. However, since the modeling techniques described in Sec. 2.4.1, as well as many others, are only approximations, other techniques are often used for confirmation of the presence of a particular species of impurity. One particularly useful method is to introduce an isotope of the suspected impurity. The isotope, though different in mass, will bond in the same manner as its counterpart. However, the LVM frequency will be different. The shift in frequency is called an isotopic shift and can be quantitatively modeled in a fairly simple manner.

Since the LVM is highly localized, the system can be treated as if the crystal lattice is fairly rigid and only consider the nearest-neighbor atom, of mass M, as movable. We now model the impurity, with mass m, as attached to the nearest atom by a spring

with force constant k. In this manner, we can solve the oscillation frequency for a diatomic model:

$$\omega = \sqrt{\frac{k}{\mu}} = \sqrt{k\left(\frac{1}{M} + \frac{1}{m}\right)}, \tag{2.60}$$

where μ is the effective mass of the system (see Sec. 8.2). In the event of isotopic substitution of the atom responsible for the LVM, a ratio r can be taken between the two resulting frequencies. For example, if we suspected hydrogen were responsible for an LVM, we could introduce deuterium and would expect a ratio of the form

$$r = \frac{\omega_H}{\omega_D} = \sqrt{\frac{k\left(\frac{1}{M} + \frac{1}{m_H}\right)}{k\left(\frac{1}{M} + \frac{1}{m_D}\right)}} = \sqrt{2\left(\frac{M+1}{M+2}\right)}, \tag{2.61}$$

where ω_H and ω_D represent the frequencies of the hydrogen and deuterium LVMs, respectively. The masses m_H and m_D were taken to equal 1 amu and 2 amu, for the respective masses of hydrogen and deuterium. In the case of hydrogen and deuterium, r is slightly less than $\sqrt{2}$ due to the fact that the other atom has finite mass and that the lattice is not perfectly rigid.

2.4.3 Anharmonic potentials

Thus far, we have only considered models using harmonic potentials. However, real potentials exhibit anharmonicity. One model that attempts to compensate for this discrepancy is the Morse potential, given by

$$V(x) = D_e\left[\exp\left(-\beta x\right) - 1\right]^2, \tag{2.62}$$

where D_e is the binding energy. In the limit of small displacement from equilibrium, Eq. (2.62) is similar to a harmonic potential with spring constant $k = 2D_e\beta^2$.

The energy eigenvalues of the Morse potential are given by

$$E_n = \frac{1}{2}\hbar\omega_e \left(n + \frac{1}{2}\right)\left[1 - x_e\left(n + \frac{1}{2}\right)\right], \tag{2.63}$$

where

$$\omega_e = \beta\left(\frac{2D_e}{\mu}\right)^{\frac{1}{2}}, \tag{2.64}$$

and

$$\omega_e x_e = \frac{\hbar\beta^2}{2\mu}. \tag{2.65}$$

The first excited state is given by

$$\Delta E = E_1 - E_0 = \hbar\omega_e - 2\hbar\omega_e x_e. \tag{2.66}$$

The anharmonicity of the potential has the effect of reducing the isotopic frequency ratio that we derived in Sec. 2.4.2. This effect results from the anharmonic term $\omega_e x_e$, which decreases with the reduced mass.

Chapter 3
EXPERIMENTAL TECHNIQUES

3.1 Fourier transform infrared spectroscopy

3.1.1 FT-IR theory

Fourier transform infrared (FT-IR) spectroscopy is employed in our research as a method of probing local vibrational modes and free carrier absorption. The FT-IR spectrometer is composed of a light source (globar), a Michelson interferometer, and an IR detector appropriate for the range of light frequencies of interest (see Fig. 3.1). The globar is a heated piece of ceramic that emits a broad range of IR frequencies through black-body radiation. The broadband light source allows one to measure a broad spectrum in a relatively short period of time. An excellent source for information on FT-IR spectroscopy has been written by Griffiths and de Haseth (1986).

The interferometer used in the spectrometer is a Michelson interferometer where one path is of fixed length while the other path is of variable length. The variable length is obtained by a motorized movable mirror. If the two paths are of equal length, then all frequencies of light will constructively interfere when the two beams are recombined. However, when the mirror is moved away from the zero-path difference condition, some frequencies will destructively interfere while others will constructively interfere. The intensity of the output beam is a function of path length difference δ

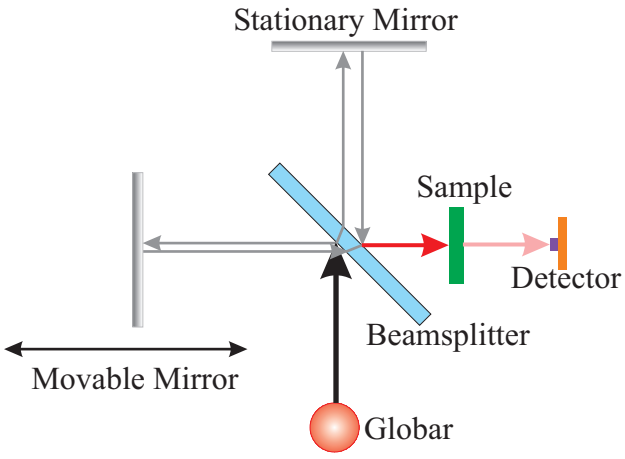

Figure 3.1: Schematic of an FT-IR spectrometer.

and light frequency $\overline{\nu}$:

$$I(\overline{\nu}, \delta) = I_0(\overline{\nu}) \cos(2\pi\overline{\nu}\delta), \tag{3.1}$$

where $\overline{\nu}$ is in wavenumbers (cm^{-1}) and δ is in cm. If the path-length difference between the two paths is zero, then the input beam is reconstructed at the output of the interferometer.

The output of the interferometer is sent through the sample of interest where some frequencies of light will be absorbed or scattered by the sample. After interacting with the sample, the composition of the beam is represented by

$$I(\overline{\nu}, \delta) = I_0(\overline{\nu}) S(\overline{\nu}) \cos(2\pi\overline{\nu}\delta), \tag{3.2}$$

where $S(\overline{\nu})$ is the fraction of light of frequency $\overline{\nu}$ that is transmitted through the sample.

Once through the sample, the beam is then incident upon a detector suitable for the spectral range. An ideal detector integrates the intensity of light over all

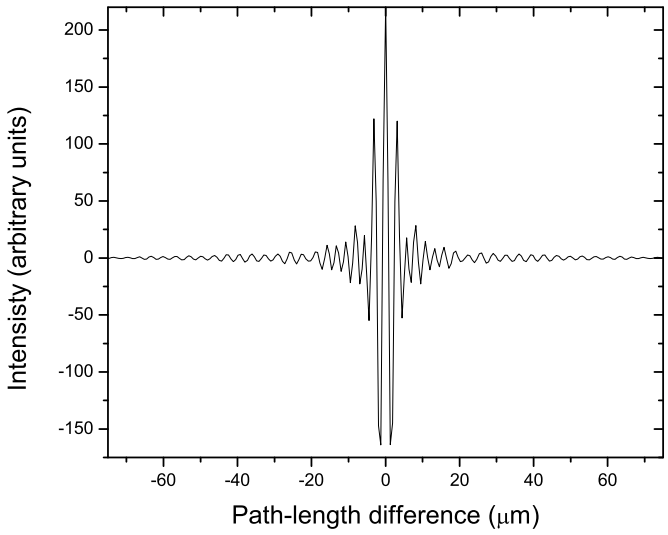

Figure 3.2: An example of an interferogram.

frequencies:

$$I(\delta) = \int_0^\infty I_0(\overline{\nu}) S(\overline{\nu}) \cos(2\pi\overline{\nu}\delta) d\overline{\nu}. \tag{3.3}$$

However, a real detector is only effective over a certain range of frequencies and has a varying efficiency over that range. A more realistic model is given by

$$I(\delta) = \int_{\overline{\nu}_{min}}^{\overline{\nu}_{max}} I_0(\overline{\nu}) D(\bar{\nu}) S(\overline{\nu}) \cos(2\pi\overline{\nu}\delta) d\overline{\nu}, \tag{3.4}$$

where $D(\overline{\nu})$ is the efficiency of the detector at a given frequency. The integral is taken over the effective range of the detector.

The collected data $I(\delta)$ is called the *interferogram* (Fig. 3.2), and is a record of intensity as a function of path length difference between the two arms of the interferometer. Collecting terms we can write Eq. (3.4) as

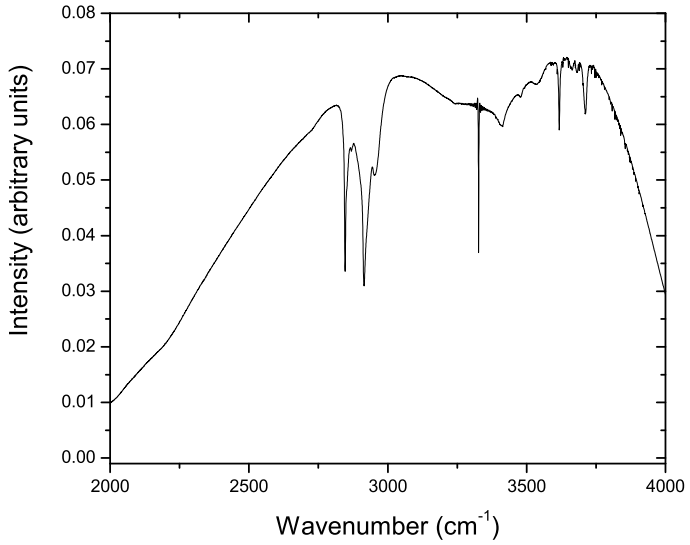

Figure 3.3: The Fourier transform of Fig. 3.2.

$$I(\delta) = \int_{\overline{\nu}_{min}}^{\overline{\nu}_{max}} B(\overline{\nu}) \cos(2\pi\overline{\nu}\delta) d\overline{\nu}, \tag{3.5}$$

where $B(\overline{\nu})$ is the "single-beam" spectrum recorded at the detector. By taking the Fourier transform of the interferogram $I(\delta)$, we recover the spectrum $B(\overline{\nu})$:

$$B(\overline{\nu}) = \int_{-\infty}^{\infty} I(\delta) \cos(2\pi\overline{\nu}\delta) d\delta. \tag{3.6}$$

Since this function is even, we can simplify it as

$$B(\overline{\nu}) = 2\int_{0}^{\infty} I(\delta) \cos(2\pi\overline{\nu}\delta) d\delta. \tag{3.7}$$

The Fourier transform of Fig. 3.2 is shown in Fig. 3.3.

Recovering the transmission spectrum of the sample, $S(\overline{\nu})$, requires a reference. The reference spectrum accounts for all the variations in the spectrum due to the globar emission spectrum, detector efficiency, and absorption features native to the spectrometer's internal environment. Dividing the reference $R(\overline{\nu})$ from Eq. (3.7) leaves

$$S(\overline{\nu}) = \frac{B(\overline{\nu})}{R(\overline{\nu})} = \frac{2}{R(\overline{\nu})} \int_0^\infty I(\delta) \cos(2\pi\overline{\nu}\delta) d\delta. \tag{3.8}$$

The transmission $S(\bar{\nu})$ is related to the concentration of absorbing material (in our case the density of defects that exhibit an LVM of wavenumber $\bar{\nu}$). This relation is known as Beer's Law:

$$A(\bar{\nu}) = \log_{10}[S^{-1}(\bar{\nu})] = \varepsilon(\bar{\nu}) l c, \tag{3.9}$$

where $A(\bar{\nu})$ is the absorbance as a function of wavenumber $\bar{\nu}$, $\varepsilon(\bar{\nu})$ is the absorptivity (absorption per unit density), l is the path-length traveled through the sample, and c is the density of absorbers in the sample.

Not all molecular bonds are observable using IR spectroscopy. Only those vibrational modes that induce a net change in dipole moment can properly couple with the electrical field component of light, thereby absorbing a photon. For this to occur, there must be some degree of ionic interaction between the atoms in the molecule. A non-polar, covalently bonded molecule will generally not absorb IR light. Even in the presence of ionic bonding, not all vibrational modes are detectable with IR spectroscopy. Three examples shown in Fig. 3.4 are the symmetric stretch, asymmetric stretch, and bending modes of a linear X-Y-X molecule. Of these, only the asymmetric stretch and bending modes are detectable with IR spectroscopy. The symmetric

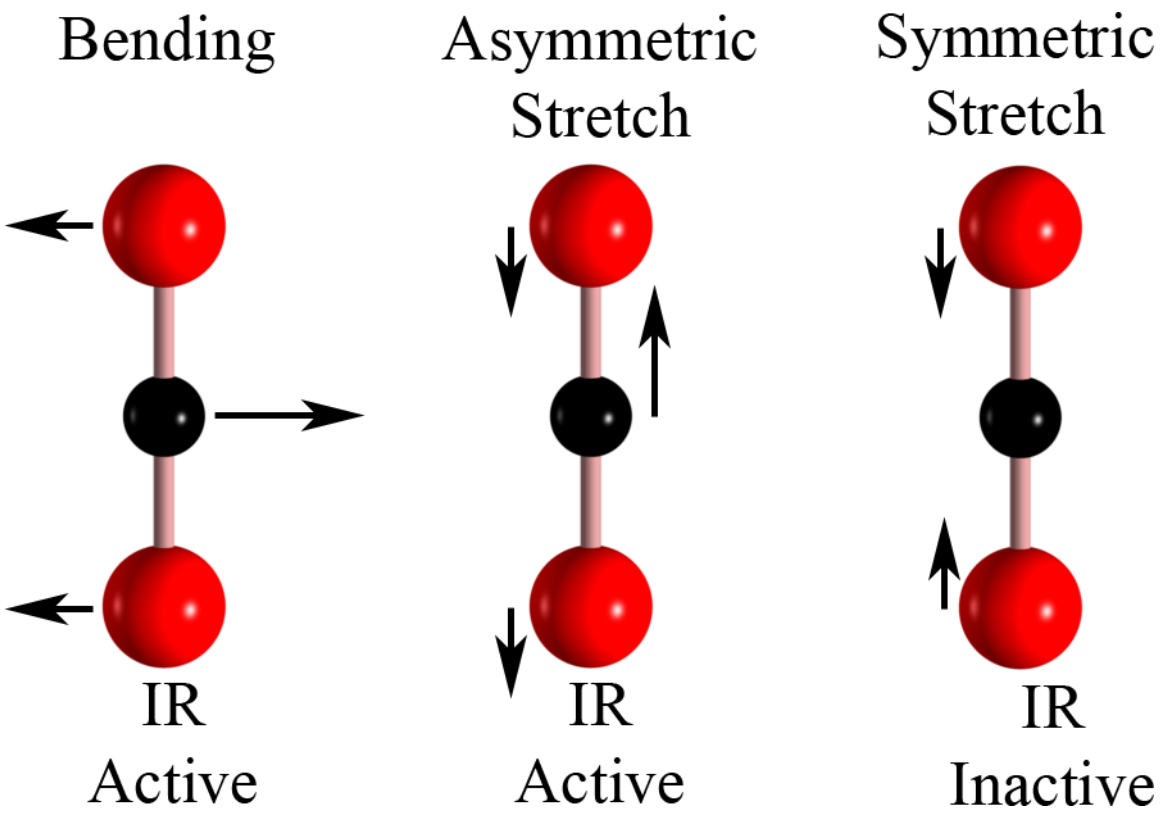

Figure 3.4: Three vibrational modes for a linear, triatomic molecule.

stretch mode does not induce a net change in dipole moment and is therefore IR forbidden.

3.1.2 Implementation

IR spectra were obtained with a Bomem DA8 FT-IR spectrometer using a variety of detectors and sample temperatures. The spectrometer is capable of using a wide array of interchangeable parts, allowing it to be tailored to the needs of the experimentalist. For this research the spectrometer was configured using a heated ceramic globar, KBr beam-splitter, and an MCT, InSb, or Ge:Cu detector. The MCT (mercury cadmium telluride) detector is sensitive to IR light in the range of 450 cm^{-1} –

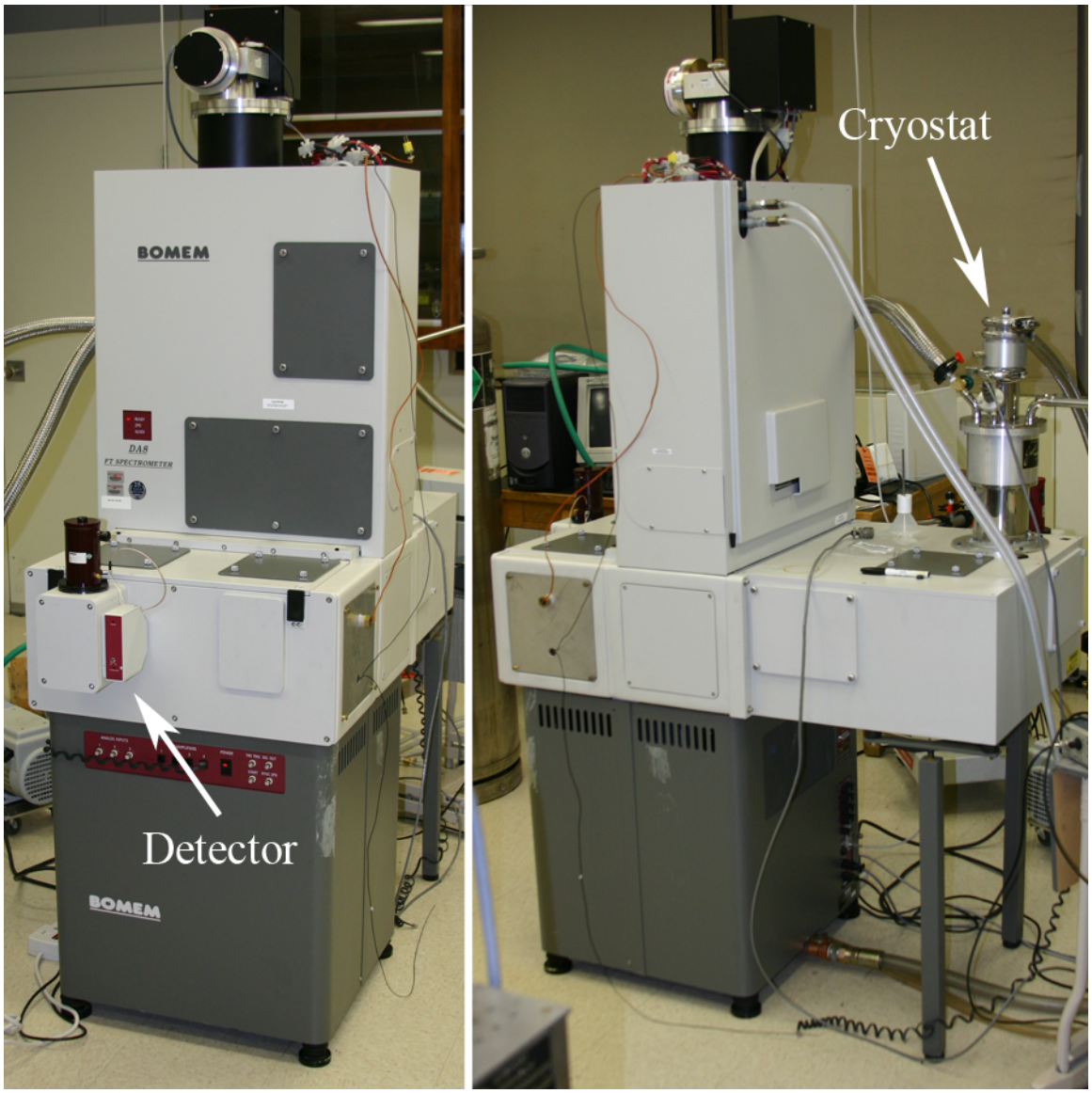

Figure 3.5: The Bomem DA8 FT-IR spectrometer with a Janis continuous-flow cryostat attached to the back port of the spectrometer. An MCT detector is attached to the front of the spectrometer for room temperature operation.

5000 cm^{-1} and must be cooled to liquid nitrogen temperatures. The InSb (indium antimonide) detector must also be cooled to liquid nitrogen temperatures but is much more sensitive than MCT in the range of 1600 cm^{-1} – 7000 cm^{-1}. The Ge:Cu (copper-doped germanium) is useful down to 350 cm^{-1} but must be cooled to a temperature below 10 K. However, the Ge:Cu detector has a high signal to noise ratio and is used in conjunction with a diamond anvil cell, where IR intensity is limited due to small aperture size. The beamsplitter is made out of KBr, which is suitable for the range between 450 cm^{-1} – 5000 cm^{-1}. The globar emits a broad black-body spectrum that is of sufficient intensity for wavelengths as low as 200 cm^{-1}.

Additional features of the spectrometer are its vacuum system and an attached Janis continuous-flow cryostat which is used to obtain sample temperatures as low as 4.2 K (using liquid helium). The vacuum system reduces unwanted absorption features due to water vapor and carbon dioxide that prove to be highly problematic for mid-IR spectra.

The Bomem DA8 spectrometer uses an in-line visible white light source and a He-Ne laser to determine zero-path-difference (ZPD) and the change in mirror position, respectively. The visible white light travels along the same Michelson interferometer as the light from the globar. For light sources of high frequencies (i.e. visible), the output of the interferometer has a very narrow and well defined maximum at ZPD. It is necessary to have this positional reference point so that each scan (one full mirror cycle) can be aligned and averaged before taking the Fourier transform. High precision tracking of the path-length difference is achieved by measuring maxima of interference fringes created when a He-Ne laser is passed through the Michelson interferometer. Each time a fringe maximum is reached, the mirror has moved a distance equal to one wavelength of the laser output (632.8 nm).

There are many deviations that the spectrometer takes from a theoretically perfect setup. One in particular is that the mirror cannot travel an infinite distance in order to create an infinitely long interferogram. This limits the resolving ability of the spectrometer. For a perfectly monochromatic source of frequency $\bar{\nu}$, the resulting spectrum is given by

$$B(\bar{\nu}) = \frac{\sin[2L\pi(\bar{\nu}' - \bar{\nu})]}{\pi(\bar{\nu}' - \bar{\nu})}, \tag{3.10}$$

as sampled through an FT-IR spectrometer limited to a maximum path-length difference of L. Equation (3.10) is referred to as the instrumental line shape. The result produces a peak with a full-width at half-maximum of $0.61/L$.

3.1.3 The benefits of FT-IR spectroscopy

When compared to gratings, Fourier transform spectroscopy has some clear benefits. The primary benefit is the amount of time necessary to take a complete spectrum. Both systems suffer from a similar fate where the cross-sectional area of the IR beam is concerned. In an FT-IR spectrometer, divergence increases the path-length traveled for rays at the edge of the beam as compared to the path-length of rays at the center of the beam. The effect from this limits the resolution of the spectrometer. The effect this has on monochrometers is similar but the tolerance for divergence is much lower. This is known as Jacquinot's advantage for FT-IR spectrometers [Jacquinot (1960)].

Another advantage is that the FT-IR spectrometer samples the entire spectrum with each mirror cycle. This is known as Fellgett's advantage [Fellgett (1958)]. A grating spectrometer requires that the spectrum is sampled at individual angles of the grating. The time required to gather a complete spectrum is proportional to the range of interest as well as resolution and beam intensity. The time it takes for an

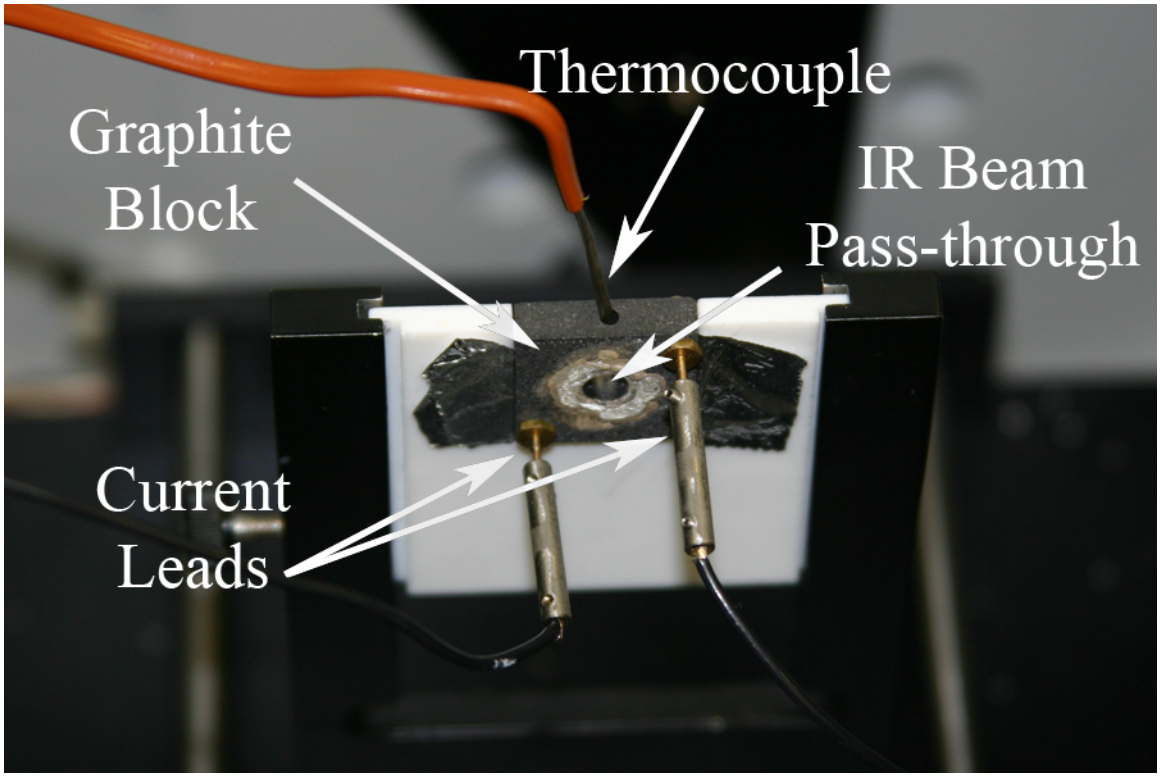

Figure 3.6: The graphite-block heater used to take IR absorption spectra at elevated temperatures.

FT-IR spectrometer to sample the spectrum is a function of resolution and beam intensity; spectral range does not affect the time necessary to complete the spectrum.

3.1.4 FT-IR measurements of samples at elevated temperatures

In order to obtain accurate decay measurements of O-H bonds in our ZnO samples, it was necessary to take FT-IR absorption spectra while keeping the sample at an elevated temperature. This was achieved by designing a graphite-block heater that fit into a ceramic sample holder (Fig. 3.6). The sample was placed over a hole through the heater and secured in place using a small amount of silver paint; enough paint was used to ensure good thermal contact. The IR beam passed through the hole in

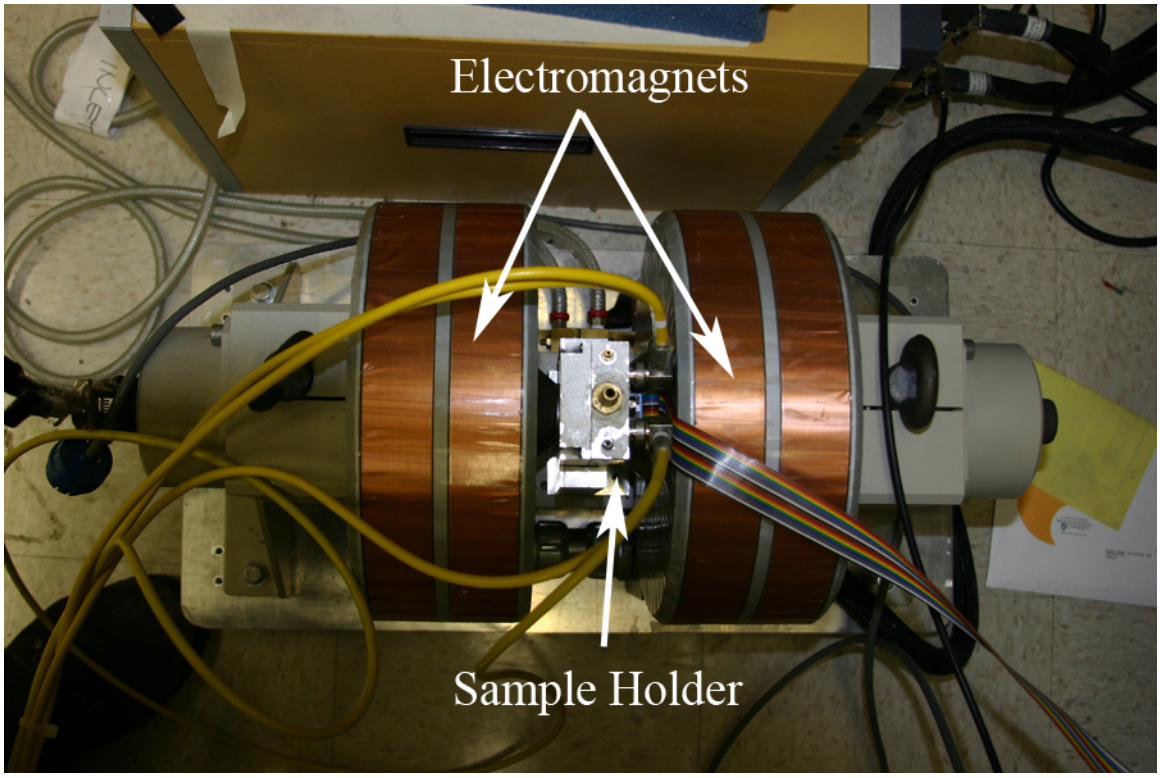

Figure 3.7: The MMR Technologies Hall System.

the heater and then through the sample of ZnO. Temperature control was achieved by passing an electrical current across the graphite block. The electrical current was supplied through two leads which entered into the evacuated spectrometer through two vacuum-tight conduits, designed specifically for the heater. The heater was capable of temperatures up to 400 K, limited by the low resistivity of the graphite and the current capability of the power supply.

3.2 Hall effect

Measurements were obtained with a Hall System from MMR Technologies, using the van der Pauw method (Fig. 3.7).

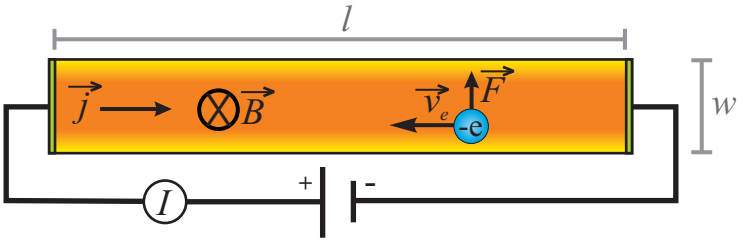

Figure 3.8: Hall effect with electrons.

3.2.1 Carrier density

The Hall effect makes use of the Lorentz force to determine the carrier type in a semiconductor. The Lorentz force states that a charged particle with velocity $\vec{v}$ and charge q will experience a force $\vec{F}$ when traveling through a magnetic field:

$$\vec{F} = q\vec{v} \times \vec{B}. \tag{3.11}$$

The force on the charged particle is perpendicular to both the B-field and the velocity vector.

Applying this concept to a solid carrying a current allows us to determine the charge and density of the carriers. Figure 3.8 shows a wafer of dimensions l, w, d carrying a current density $\vec{j}$. The electrons in the sample will experience a force as per Eq. (3.11). However, since there is no path for the current to flow in the vertical direction in Fig. 3.8, there must also be an induced electric field such that

$$\vec{F} = \vec{F_H} + \vec{F_B} = q(\vec{E_H} + \vec{v} \times \vec{B}) = 0, \tag{3.12}$$

where $\vec{F_H}$ and $\vec{F_B}$ are the forces from the electric and magnetic fields, respectively. The potential from the electric field can be measured directly and allows us to deter-

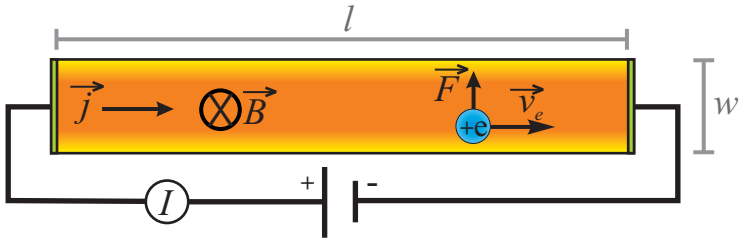

Figure 3.9: Hall Effect with holes

mine the electron density in the sample. Rewriting Eq. (3.12) in terms of measured quantities yields

$$F_H + F_M = \frac{-V_H q}{w} + \frac{IB}{An} = 0, \tag{3.13}$$

where I is the total electron current, A is the cross sectional area $w \times d$, V_H is the measured voltage from the induced electric field, and n is the electron density. Since the net force is equal to zero, we can write

$$\frac{V_H q}{w} = \frac{IB}{An}. \tag{3.14}$$

Finally, we obtain an equation for the electron density:

$$n = |\frac{IB}{(^-e)V_H d}|, \tag{3.15}$$

where $-e$ is the charge of an electron .

While the previous example was a material with electron charge carriers, the same treatment can be applied to a semiconductor with hole charge carriers. Figure 3.9 shows a similar setup as Fig. 3.8 except that now we are using a material with hole charge carriers. Since holes and electrons have opposite charge, they travel in opposite directions for a given current. A quick comparison between the two figures shows that

the holes experience a Lorentz force of the same magnitude and direction as that of the electrons. For the situation in Fig. 3.9, the induced electric field will be in an opposite direction to that in Fig. 3.8. Therefore the resulting polarity of the measured Hall voltage, V_H, determines whether the majority charge carriers are electrons or holes. The hole concentration p is given by

$$p = |\frac{IB}{e(V_H)d}|. \tag{3.16}$$

3.2.2 Mobility

The Hall effect can also determine the mobility μ of the charge carriers. The mobility is defined as

$$\overrightarrow{v} = \mu \overrightarrow{E}, \tag{3.17}$$

where $\overrightarrow{E}$ is the electric field driving the current. Substituting this expression into Eq. (3.12) yields the mobility:

$$q(\overrightarrow{E_H} + \mu \overrightarrow{E} \times \overrightarrow{B}) = 0 \tag{3.18}$$

$$\mu = \frac{-\overrightarrow{E_H}}{\overrightarrow{E} \times \overrightarrow{B}}. \tag{3.19}$$

3.2.3 Van der Pauw geometry

Van der Pauw (1958) showed that Hall-effect measurements can also be made on arbitrarily shaped *lamellae*, or disk-like samples. To do this all that is needed are four electrical contacts located near the edges of the sample. This particular configuration is known as the "van der Pauw geometry."

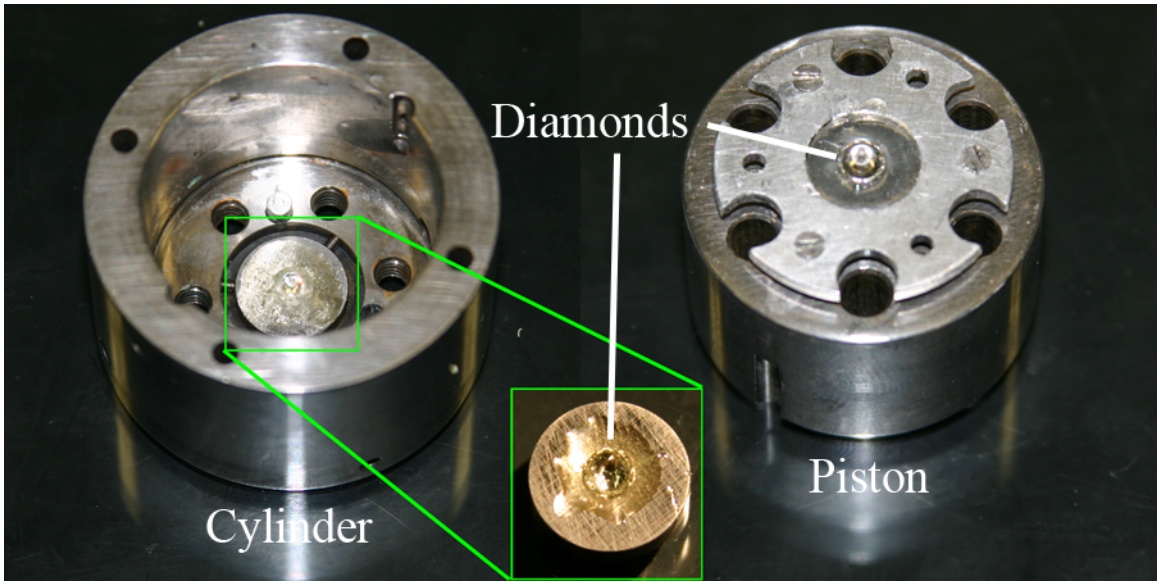

Figure 3.10: A diamond anvil cell. The inset is a picture of the cylinder's backing plate with affixed diamond.

3.3 High pressures obtained by diamond-anvil cells

3.3.1 Introduction

The application of hydrostatic pressure is performed via diamond-anvil cells (DACs). The use of diamond for high-pressure experiments has many advantages. First and foremost is the hardness of diamond. Not only is it the hardest material known, it is also highly transparent to a broad range of IR and visible radiation. This makes diamond nearly ideal for IR spectroscopy measurements on materials under pressure.

The diamond-anvil cell used for this work consists of two diamonds situated on opposite sides of a thin sheet of metal (gasket). These components are housed in a two-piece piston-cylinder diamond-anvil cell which applies force to the backs of the diamonds (Fig. 3.10). The force is concentrated to the culets (see Fig. 3.11), resulting in large pressures. Hydrostatic pressure is achieved inside a cylindrical hole that is

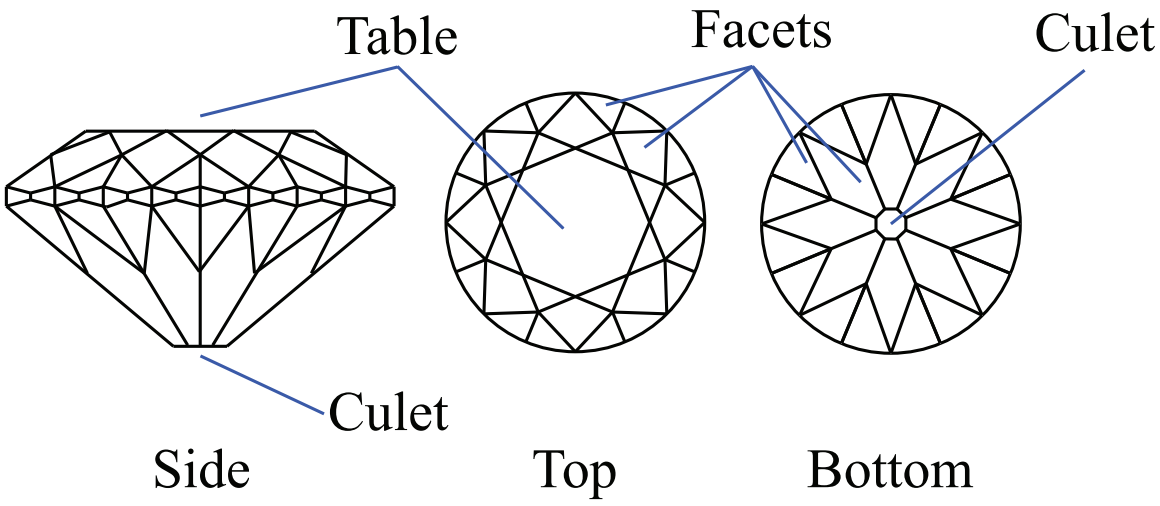

Figure 3.11: Schematic of a round brilliant-cut diamond.

drilled out of the gasket and filled with the sample, an ambient pressure medium, and ruby chips used for the room-temperature pressure calibration. The diameter of this hole is smaller than that of the diamond culet, allowing the diamonds to act as caps, preventing the pressure medium from leaking out.

3.3.2 Diamonds

There are two types of diamonds used in the DAC, type-I diamonds and type-IIA diamonds. Type-I diamonds include nitrogen defects, resulting in a broad IR absorption between 1000 cm^{-1} and 1500 cm^{-1}. Type-IIA diamonds do not have nitrogen defects but are substantially more expensive. Both types of diamonds include the two-phonon absorption at 2100 cm^{-1}.

Moissanite (SiC) anvils can also be used in place of diamonds [Xu *et al.* (2000)]. Moissanite has the advantage of being less costly than diamond. Due to their low cost, they can be cut into larger anvils. The larger aperture available on a larger anvil

can be beneficial for FT-IR measurements. However, they have the disadvantage of absorbing strongly in portions of the mid-IR spectrum. They also lack the ability to attain the same high pressures as diamonds of the same size.

3.3.3 Gasket

The gasket is used to contain the pressure medium laterally and to create a seal around the diamond culets. Various types of metal can be used for a gasket depending on what pressures are to be achieved. However, using stronger metals can increase the risk of diamond fracture. The experiments described here used a 0.25 mm thick grade #304 stainless steel gasket for pressures up to 8 GPa. Where high pressures were not necessary, moissanite anvils in conjunction with a 0.45 mm thick Cu:Be gasket were used to obtain pressures up to 2 GPa.

3.3.4 The loading cell

The DACs were constructed by Steve Watson of Washington State University and are of a piston-cylinder Merrill & Bassett design [Merrill and Bassett (1974); Sterer *et al.* (1990)]. The diamonds are affixed to two separate backing plates by means of "five-minute" epoxy. The backing plate on the piston can be adjusted for tilt alignment, while the backing plate in the cylinder can be adjusted for translational alignment. Both backing plates are held in place by set screws which also control their respective alignments. Force is applied to the diamonds by means of six hex-bolts that pass through holes in the piston and thread to the cylinder, pulling the piston closer to the bottom of the cylinder.

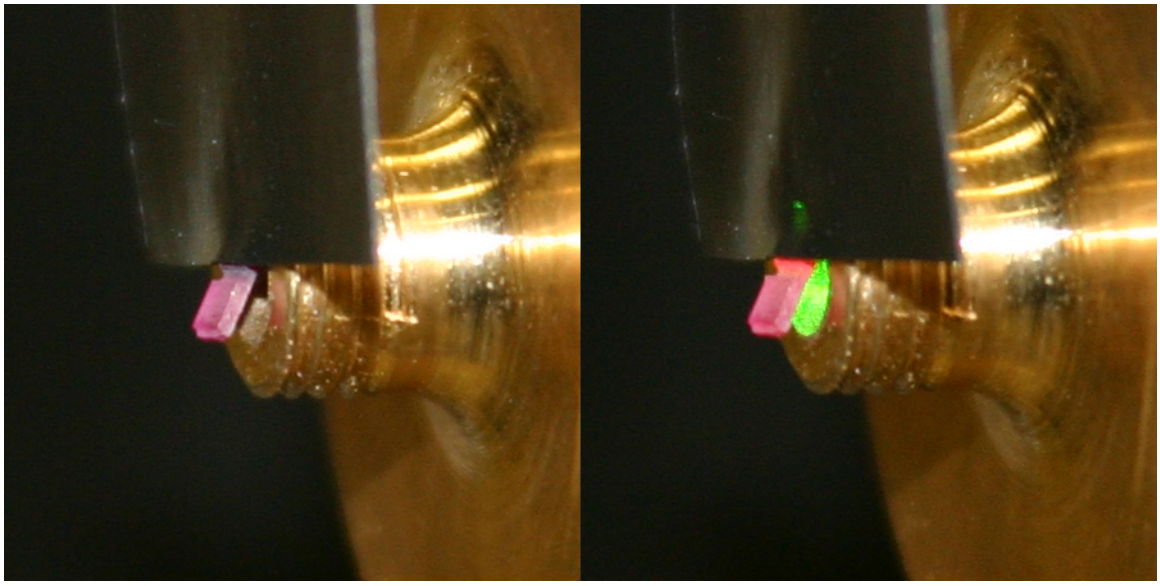

Figure 3.12: Pictures of ruby in room light (left) and fluorescing under green laser light (right).

3.3.5 Pressure calibration

Initial pressure calibration is achieved by measuring the fluorescence emission from ruby (Al_2O_3:Cr^{3+}). Ruby contains Cr^{3+} ions that are excited by 532 nm or shorter wavelengths of light. These ions emit two red fluorescence peaks near 694.5 nm. The stronger emission is designated as R_1 while the weaker is designated R_2. Both fluorescence peaks shift with pressure. Previous studies used the stronger R_1 emission as a pressure calibration [Forman *et al.* (1972); Mao *et al.* (1978)]. It was determined that the R_1 fluorescence peak center shifts linearly at a rate of 0.036 nm/kbar for pressures below 300 kbar, suitable for our range of study (1 kbar = 0.1 GPa).

While ruby fluorescence has been very well calibrated to pressure, it is not convenient to sample a fluorescence spectrum at low temperatures in the FT-IR spectrometer. Due to thermal contraction, the pressure determined at room temperature is

unreliable once the diamond-anvil cell has been cooled to liquid-helium temperatures. It is much more convenient to use a material with a pressure-sensitive IR absorption peak. In this case we can use the trace CO_2 molecules that dissolve in the liquid nitrogen pressure medium while loading the cell in an open air environment [McCluskey *et al.* (2002)]. Equation (3.20) describes the frequency, in wavenumbers (cm^{-1}), of the CO_2 ν_3 IR absorption peak as a function of pressure [McCluskey *et al.* (1996)]:

$$\nu_3(CO_2) = \begin{cases} 2349.3 + 12.3P & 0 \leq P \leq 0.45 \\ 2347.6 + 8.4P & 0.45 \leq P \leq 1.3 \\ 2349.5 + 6.9P & 1.3 \leq P \leq 1.9 \\ 2345.1 + 6.6P & 1.9 \leq P \leq 7 \end{cases}, \tag{3.20}$$

where P is in units of GPa. The discontinuities in Eq. (3.20) are due to phase changes in the N_2 pressure medium.

3.3.6 Loading the cell

Great care must be taken while preparing a DAC. Several steps require great patience and attention to detail. If great care is not taken, the likelihood of diamond fracture increases dramatically.

The first step to preparing a DAC is to affix the diamonds to the backing plates, which will later be placed in the cell. Each backing plate contains a hole, which is actually a tapered cone that directs the light through the backing plate. It is important to make sure that the diamonds are affixed to the correct side of the backing plate. The diamonds are affixed using an epoxy, the purpose of which is to keep the diamond in place. It is not necessary to use any particular kind of epoxy for this basic purpose. However, some epoxies hold up better under the low temperatures

the diamond-anvil cell experiences during its use. Using a microscope, be sure that the diamonds are directly over the holes on the backing plate. A small amount of epoxy should be applied around the diamond and should coat a portion of every facet, excluding the table and the culet (see Fig. 3.11). Care should be taken to prevent any epoxy from seeping under the diamond as this will create an unstable base for the diamond to rest on. If epoxy is accidentally applied to the culet, as much as possible should be removed while the epoxy is wet. The remaining epoxy can be scraped from the culet after it has dried.

After affixing the diamonds to the backing plates, they can be placed into the DAC. Be sure that no foreign material is located between the backing plates and the cell. Any foreign matter may cause the backing plates to shift during DAC operation, increasing the likelihood of inaccurate data or even diamond fracture. The diamonds can now be aligned using the set screws. Place the piston in the cylinder and allow the diamond surfaces to gently come into contact with each other. Be sure to rotate the piston so that the reference marks on both pieces of the cell are aligned. Close examination of the diamonds will reveal Newton's rings caused by a small gap between the diamonds due to their surfaces not being parallel to each other. Tilt direction can easily be determined by applying pressure to various points on the piston. Remove the piston and adjust the set screws on the tilt plate to correct for the tilt. Repeat this process until the diamond surfaces are as close to parallel as possible. Precise tilt alignment can be achieved by lightly tightening the hex-bolts on the assembled DAC until the interference fringes have completely disappeared. All hex-bolts should be slightly tight to prevent piston motion.

Once the diamonds are parallel, they should be aligned so that the facets around the culet are indistinguishable between the diamonds. If a diamond needs to be

rotated, the cell will have to be disassembled and the backing plate rotated. Translational alignment is achieved through the set screws that hold the backing plate in the cylinder. While looking through the DAC in a microscope, adjust the three set-screws until the culets are perfectly aligned.

The process should be repeated until optimal alignment is achieved. Once the diamonds have been aligned, measure the thickness of the cell at three equally spaced points. If these values vary from each other by more than 75 μm, it may be a sign that a backing plate is not flush with the inner surface of the DAC. Once this condition is met, note the differences between the thickness at each of the three points. These differences must be maintained throughout operation of the DAC to ensure that the diamond culets remain parallel. This procedure will decrease the risk of diamond fracture during the remaining steps.

The gasket can be prepared after the diamonds have been aligned. Remove the hex-bolts from the cell. If they are tight, then be sure to unscrew them equal amounts in several steps to prevent a large pressure gradient from occurring over the diamond culets. Carefully remove the piston from the cylinder. Place the gasket on top of the diamond in the bottom of the cell. Be sure to mark the gasket so it can be re-inserted with the same orientation after removal in further steps. If balance is difficult to maintain on the gasket, insert a post through the post hole in the cylinder portion of the gasket. Affix the gasket to the post with a piece of clay. The gasket should not be directly supported by the post, otherwise the gasket may not be properly level with the diamond culet. Next, carefully place the piston into the cylinder and allow the diamond to come into contact with the gasket. Insert the hex-bolts and lightly tighten each one. Measure the thickness of the cell at the same three positions as done previously. Tighten the hex-bolts until the diamonds are parallel. The gasket should

be compressed to at least 150 μm. Higher pressures will require thinner gaskets, otherwise gasket deformation will occur. Gasket compression should be accomplished by turning each hex-bolt in small increments, making sure that the diamonds are parallel throughout the process.

Carefully remove the hex-bolts. Make sure that the diamond culets are parallel throughout the removal process, preventing a large pressure gradient from occurring across the diamonds. The indentations created by the diamonds should be clear and uniform on both sides of the gasket. The indentation will allow us to drill a hole that is centered on the diamonds and will also allow for easy alignment of the gasket and diamonds. The gasket is now ready to be drilled. The drilling process in this work was done by hand, but has since been adapted to a mechanical drill by Gabriel Hanna, Washington State University. Drilling should be done with a bit that is less than one-half the diameter of the diamond culet. The bit can be centered in the indentation with the aid of a tilted mount an a microscope, allowing you to easily see where the drill is in contact with the gasket. Precise centering of the hole is not necessary, but the hole must not touch the edges of the culet indentation. This would prevent the diamonds from properly sealing the hole once it has been loaded with a pressure medium. Once the hole has been drilled, the edges should be cleaned, removing any burrs that could interfere with the diamond-gasket seal.

The next step in loading a diamond-anvil cell is the preparation of the sample. The sample must be thin enough to fit between the diamonds in the space supplied by the final thickness of the gasket. Samples of ZnO were thinned by polishing to a thickness of less than 100 μm. To achieve control over the polishing process, the sample is affixed to a glass slide using melted wax. The wax keeps the front and back surfaces of the crystal parallel to each other, a convenience for FT-IR spectroscopy.

Once thinned, a small piece can be broken off and cleaned of wax using any solvent that will not react with the material. In the case of ZnO, methanol or acetone was used. It is necessary that the sample is small enough such that any two points do not touch the walls of the gasket hole at any one time. The sample must not become lodged in place if hydrostatic pressure is to be maintained. However, the samples should also be large enough to minimize light leakage around the sample.

Reinsert the gasket into the cylinder portion of the DAC. Be sure to align the reference points so that the gasket is properly aligned with the diamonds. Again, if the gasket is not easily balanced, use clay to affix it to a post. Make sure that the gasket sits flat on the bottom diamond.

Place a piece of the sample in the gasket hole. Check to make sure the sample is not too large. Next, place some small pieces of ruby in with the sample. Make sure that the remaining portion of the indentation is clear of ruby or any other debris, as this material could interfere with the diamond-gasket seal. Carefully place the piston portion of the DAC into the cylinder, maintaining rotational alignment. Using a microscope, make sure that the indentation is aligned properly with the diamond. If a gentle rocking motion of the piston does not cause the indentation to align with the diamond, then it is necessary to remove the piston and adjust the gasket. If the gasket is lifted off the bottom diamond at any time, then the sample and ruby could fall out of the hole.

Once the top diamond is aligned, insert the hex-bolts and tighten them just enough to prevent the top diamond from separating from the gasket. Turn the DAC over and make sure the gasket is aligned with the bottom diamond.

Once the DAC has been loaded with ruby and a piece of the sample, it is now ready to be filled with a pressure medium. In these experiments, liquid nitrogen

was used [Schiferl *et al.* (1978)]. (If a less evaporative liquid is to be used, it can be inserted immediately after the sample and ruby have been inserted.) To fill with liquid nitrogen, the DAC will be immersed in a container of the liquid. Before this is done, the DAC needs to be mounted to a plate that can be held in place during the liquid nitrogen immersion. The plate is necessary to attain enough leverage to tighten the hex-bolts after the cell is filled with liquid nitrogen. Place the metal plate with the DAC into the liquid nitrogen. The tools used to hold the plate in place and tighten the cell should also be propped up so that the parts that will come in contact with the cell are cooled to liquid nitrogen temperatures. It has been advantageous to bubble helium gas into the liquid nitrogen around the DAC during the cooling and sealing process. The helium gas seems to suppress the boiling of liquid nitrogen, increasing the likelihood of a successful loading. When the DAC has reached thermal equilibrium with the liquid nitrogen, begin tightening the hex-bolts. Be sure to tighten each bolt only slightly before moving on to the next, attempting to keep the diamonds parallel during this process. After tightening each bolt a few times, carefully remove it from the liquid nitrogen, using tools (not hands). Allow the DAC to warm up to room temperature.

Check to see if the cell is loaded by measuring the ruby fluorescence. If the cell is loaded, a measurable shift will be seen in the ruby fluorescence peaks. Use an external ruby sample in a separate measurement as a reference. The pressure will probably be at least 5 kbar. If the pressure is lower than this, go back and tighten the screws until the diamonds are level. Take another fluorescence spectrum. If the spectrum has not shifted, the DAC may not be sealed properly. Confirmation of this can be achieved by further tightening of the hex-bolts, while maintaining the parallel surfaces of the

diamonds. If the pressure does not change, then the DAC should be loosened and another attempt at liquid nitrogen loading should be made.

3.4 Neutron activation analysis

Compositional analysis of materials can be obtained through neutron activation analysis (NAA). The process involves bombarding the sample with thermal neutrons, some of which are captured by atoms in the sample. In many cases, the new isotope formed is stable. In the case that the new isotope is not stable, it will decay and emit particles with characteristic energies, thereby providing a chemical "fingerprint". By measuring the spectrum of emitted gamma-ray photons and comparing it to a standard exposed to the same neutron flux, the composition of the sample can be determined. The process by which a sample is bombarded with neutrons and then later observed for gamma emission is known as delayed gamma neutron activation analysis (DGNAA). An overview of neutron activation analysis can be found at www.wikipedia.org.

DGNAA was performed using the 1 MW General Atomics TRIGA nuclear reactor at Washington State University. Two samples, one produced by Eagle Picher and the other produced by Cermet Inc., were placed in the reactor along with two standards of known composition. Each standard was placed within close proximity of each of the samples in the reactor. This ensures that both sample and standard receive the same dosage of neutrons, a necessary condition for the composition of the sample to be determined accurately.

The standard provides a calibration from which the composition of the sample can be extrapolated. The energy spectrum of photons radiating from the sample and the standard are measured simultaneously. The energies are characteristic of the isotopes

that emit them, allowing us to determine what elements are present in the sample. Since the intensity of each energy peak is proportional to the number of radioactive atoms, the standard can be used to determine the absolute number of radioactive atoms in the sample. From these values, the densities of isotopes can be determined using the following equation:

$$\rho_{sam} = \rho_{std} \frac{V_{std}}{V_{sam}} \frac{I_{sam}}{I_{std}}, \tag{3.21}$$

where ρ_{sam} and ρ_{std} are the densities of a given radioactive element in the sample and standard, respectively, V_{sam} and V_{std} are the total volumes of the sample and standard, and I_{sam} and I_{std} are the intensities of the energy peak associated with that element. It should be noted that the intensities of each peak must be decay corrected so that they represent the activity immediately after neutron bombardment.

Not all isotopes formed by neutron capture are unstable. If a neutron capture event results in a stable isotope, then this method of neutron activation analysis can not directly measure the presence of that isotope. This is not a problem as long as the relative abundance of isotopes for a given element is known. In most cases, samples consist of isotopes in naturally occurring relative abundances, which are well known. However, if the sample deviates from the natural isotopic abundances, then more must be known about the sample to determine all isotope concentrations.

A second method of neutron activation analysis measures the energies of emitted photons at the time of neutron capture. This method, known as prompt gamma neutron activation analysis (PGNAA), can determine isotopic abundances of elements regardless of the stability of the resulting isotope. However, since the detector would be saturated by neutrons if it were inside the reactor, PGNAA uses a beam of neutrons

from the reactor incident upon the sample, with the detector well outside of the beam's path. Since the neutron flux in a beam is much lower than that of the neutron flux inside the reactor, PGNAA is not as sensitive as DGNAA. In both cases, if the element has a low cross-section for neutron capture, detection may also be difficult.

3.5 Secondary ion mass spectroscopy

Secondary ion mass spectroscopy (SIMS) was employed to determine compositional differences between single-crystal ZnO from Cermet Inc. and Eagle Picher. The samples were sent to the Evans Analytical Group for compositional analysis. Their website (www.eaglabs.com) has an excellent tutorial on SIMS, which is summarized below.

The SIMS process uses a beam of ions to bombard the surface of a sample. During this process, surface atoms are broken off by the bombardment, many of which become ionized in the process (secondary ions). These ions will have a broad dispersion of velocities and must be sent through a "velocity selector". The ions of a specific velocity are then sent through a series of electrostatic lenses and then sent to a mass analyzer, a magnetic field which separates out ions depending on their charge and mass. The process is governed by the force equation

$$\overrightarrow{F} = q\left(\overrightarrow{E} + \overrightarrow{v} \times \overrightarrow{B}\right), \tag{3.22}$$

where q is the charge of the ion, $\overrightarrow{v}$ is its velocity, $\overrightarrow{E}$ is the electric field, and $\overrightarrow{B}$ is the field of induction within which the ions travel. The "velocity selector" is simply perpendicular electric and magnetic fields that only allow charged particles of a certain velocity to pass through without having a net force applied. Given an electric field with magnitude E_s and a magnetic field of magnitude B_s, there exists only one velocity

v_s that satisfies the following equation:

$$F \propto E_s + v_s B_s = 0 \tag{3.23}$$

A thin slit just past the selector ensures that only ions traveling in a straight path, ions with velocity v_s, are allowed to pass. The mass spectrometer uses a magnetic field so that the radius of the path of an ion, given its velocity is v_s, depends only on the charge and mass of the ion and the strength of the magnetic field in the spectrometer:

$$r = \frac{m v_s}{qB}. \tag{3.24}$$

Generally, SIMS uses two different types of ion beams (O_2^+ and Cs^-). The two beams are used due to their effectiveness at creating ions of different groups of elements. For instance O_2^+ is more effective at ionizing many of the rare-earth elements as well as the transition metals, due to the affinity of oxygen for electrons, which are easily pulled from these elements. Cesium is precisely the opposite, giving electrons to those elements with a high affinity for them.

3.6 Growth of zinc oxide using chemical vapor transport

In an attempt to study defects systematically, we used chemical vapor transport (CVT) to grow our own ZnO crystals [Look *et al.* (1999); Mycielski *et al.* (2004)]. Chemical vapor transport uses a combination of source materials and transport agents to grow high quality crystals. Single crystals are typically deposited on a substrate or seed. The source materials contain the elements that compose the final crystals and dopants of interest. The transport agents react with the source materials until a temperature dependent equilibrium is reached. As the products move into a cooler

region, the reverse reaction occurs, depositing material onto a substrate. CVT is particularly useful for materials with low vapor pressures, in which case extremely high temperatures may be required to grow crystals without an intermediate reaction.

When growing ZnO crystals, it was found that graphite performs as an excellent transport agent [Mycielski *et al.* (2004)]. Graphite, used in conjunction with high purity ZnO micro-particles, resulted in high quality and high purity ZnO polycrystalline growth. In this process the most probable reaction is

$$2\mathrm{ZnO}\,(s) + \mathrm{C}\,(g) \longleftrightarrow \mathrm{CO}\,(g) + \mathrm{Zn}\,(g)\,, \tag{3.25}$$

where s and g refer to the solid and gas phase, respectively.

In order to grow ZnO poly-crystals, ZnO micro-particles obtained from Sigma-Aldrich were mixed with graphite powder and placed in a quartz (fused silica) ampoule. The ambient air was evacuated and backfilled with $\frac{1}{2}$ atm of Ar or NH_3 gas, and the ampoule sealed closed with a hydrogen-oxygen torch. The use of NH_3 as an ambient was an attempt to introduce N impurities, acceptors in ZnO, into the growth. The ampoule was placed in a horizontal tube furnace. The source material was heated to a temperature of 900°C driving Eq. (3.25) to the right side of the equation until an equilibrium was reached. The natural temperature gradient in the furnace left the growth end of the ampoule at a temperature of 825°C. As the CO_2 and Zn vapor travels towards the cooler end of the ampoule, the reverse happens in Eq. (3.25), pushing the reaction to the left side of the equation until equilibrium is attained for the new temperature. At first, the deposition occurs on the fused-silica ampoule walls, not an ideal substrate for the deposition of ZnO. However, once a thin

layer of ZnO is deposited, the energetically favorable orientation for ZnO becomes apparent in the shape of hexagonal faceted growth.

An attempt at seeded growth was made by placing a piece of ZnO from Cermet Inc. at the cooler end of the ampoule. However, this approach met with little success, as the ZnO preferred to grow on the ampoule wall instead. It is possible that the curvature of the ampoule prevented the seed crystal from achieving good thermal contact with the ampoule wall. The seed crystal would then be several degrees warmer than the ampoule wall, possibly accounting for the lack of growth on the seed. Since crystalline growth could be achieved on the ampoule wall, it was decided to proceed without the use of a seed crystal.

A variety of crystal sizes were achieved and seemed to depend on both the growth temperature as well as the ratio of graphite to ZnO. We achieved excellent crystal growth using 2.0 g graphite and 1.5 g ZnO. Detailed crystal growth results are given in Sec. 5.1.

It should be noted that during the growth process there is an increase in the amount of CO_2 gas inside the ampoule. The ampoule was able to handle the increased pressures even at 950 °C. However, while the ampoule is being cooled, the ZnO crystal growth contracts with a different thermal-expansion coefficient than that of the ampoule wall. In the process of pulling away from the substrate, the ZnO can crack the ampoule, causing the wall to succumb to the internal pressure. For this reason we designed a shield that would contain the debris from the resultant explosion. Another solution to this problem is to allow the slow etching of the ampoule wall to create a tiny worm-like hole that allows the pressure to be relieved before the cool-down process. However, with the current setup, it is difficult to determine precisely when

this occurs. Also, this is not an option if it is necessary to maintain separation between the internal components and the outside air.

In an attempt to control the growth rate, ZnO was mixed with water and then boiled down to form larger ZnO aggregate masses. By decreasing the effective surface area of the ZnO starting material, the growth rate should be slowed. This approach proved highly successful. Using ZnO aggregate and graphite powder produced crystals of larger size. While the effect was positive, it is not certain whether it was due to the decreased surface area of the aggregated ZnO or whether it was due to the presence of water left over after boiling the mixture.

In several growth attempts the product was orange-colored polycrystalline ZnO. The production of orange-colored crystals seemed to depend on growth temperature and were readily grown at temperatures above 900 °C. In addition to the color, metallic droplets were apparent on the surface of the crystal growth. Energy-dispersive x-ray analysis (EDX) was later used, in conjunction with a scanning electron microscope (SEM), to determine that the metallic drops were Zn. It was later found that the graphite was contaminated with an unknown material. Replacing the graphite with high-purity graphite obtained from Sigma-Aldrich eliminated the orange color in the crystal growth. Previous researchers have found that annealing ZnO single-crystals in a Zn rich environment produces this color change [Mikami *et al.* (2005)]. By placing some Zn in with the high purity graphite and ZnO, we were able to recreate the orange color in the ZnO growth. However, it is uncertain whether the previous graphite source was contaminated with Zn or a material that reacted with oxygen, producing a Zn rich environment.

Chapter 4
HYDROGEN IN ZINC OXIDE

4.1 Bulk single-crystal ZnO sources

Bulk, single-crystal samples of ZnO were purchased from Cermet Inc. and Eagle Picher. Samples from Cermet Inc. and Eagle Picher had dimensions of 5 mm × 5 mm × 0.5 mm, which were cut from larger boules and polished prior to shipping. The samples were further cut into smaller pieces prior to annealing or other modification. In addition, we obtained samples from Prof. Kelvin G. Lynn that were of uncertain pedigree.

4.2 Determining the location and effects of hydrogen in ZnO

4.2.1 LVM spectroscopy

After annealing the samples in hydrogen, a new absorption peak was observed at 3326.3 cm^{-1} at liquid-helium temperatures and 3336.8 cm^{-1} at room temperature (Fig. 4.1) [McCluskey *et al.* (2002)]. We postulated that this absorption peak was due to an O-H stretch mode within the bulk single-crystal ZnO. The LVM frequency is similar to O-H complexes in GaAs, which have a stretch-mode frequency of 3300 cm^{-1} at liquid-helium temperatures [Pajot *et al.* (1992)].

Upon annealing an as-grown sample of ZnO in deuterium, a new absorption peak was observed at 2470.3 cm^{-1} at liquid-helium temperatures. After annealing in only deuterium, there was no absorption peak observed at 3326.3 cm^{-1}. Likewise, when annealing in only hydrogen, no absorption peak was observed at 2470.3 cm^{-1} (Fig.

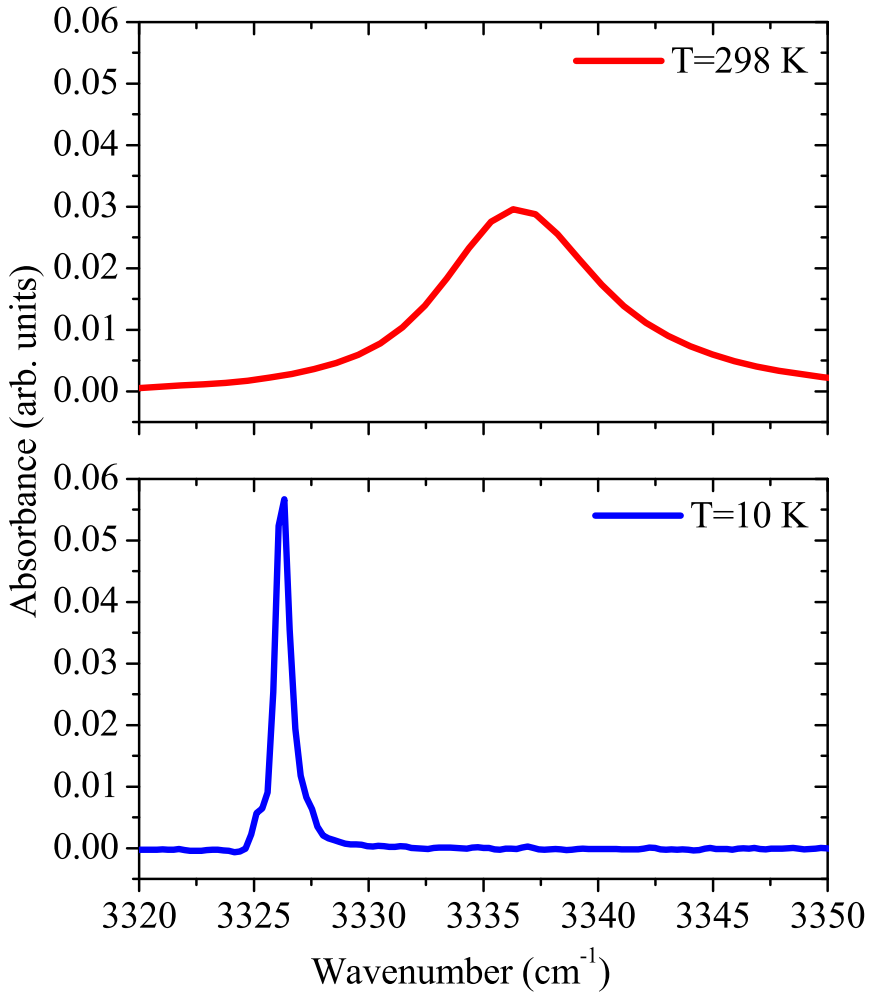

Figure 4.1: The O-H stretch mode observed at 3336.8 cm^{-1} at room temperature and 3326.3 cm^{-1} at liquid-helium temperatures.

4.2). Only when a mix of hydrogen and deuterium are used in the annealing process are both the 3326.3 cm^{-1} and the 2470.3 cm^{-1} absorption peaks visible in the same sample (Fig. 4.3). The ratio between these two frequencies is r=1.3465, in agreement with the isotopic shift model for hydrogen and deuterium. This is precisely the value observed in GaP for O-H and O-D bonds, where the ratio is also r=1.3465 [Ulrici *et al.* (1998)]. Furthermore, the vibrational frequency of 3326.3 cm^{-1} is in good agreement with Van de Walle's theoretical prediction of hydrogen in an AB position bonded with oxygen (ω = 3550 cm^{-1} in the harmonic approximation). As an estimate, we used the calculated anharmonic shift for an O-H molecule in the gas phase [Herzberg (1989)], which yields a decrease in ω by 166 cm^{-1}, resulting in a frequency of 3384 cm^{-1}. However, the anharmonic shift may be different than this initial estimate, so hydrogen in a BC position bonding with oxygen (ω = 3680 cm^{-1} in the harmonic approximation) cannot be ruled out by these results alone.

4.2.2 Comparison with theory

In an attempt to find the second excited state for the O-H vibrational stretch mode, we expanded the FT-IR frequency range by substituting the KBr beamsplitter with a CaF_2 beamsplitter. The CaF_2 beamsplitter allowed us to observe the range of IR frequencies where we expected the second harmonic of the O-H LVM. In the harmonic approximation, the n=0→2 transition would have exactly twice the frequency of the first excited state (3326.3 cm^{-1}). However, due to anharmonicity, we would expect to find the actual frequency below 2×3326.3=6652.6 cm^{-1}. Our observations showed a weak absorption peak at 6389.1 cm^{-1} at liquid-helium temperatures, a deviation of 263.5 cm^{-1} from the expected value for a harmonic potential (Fig. 4.4) [Jokela and McCluskey (2005)].

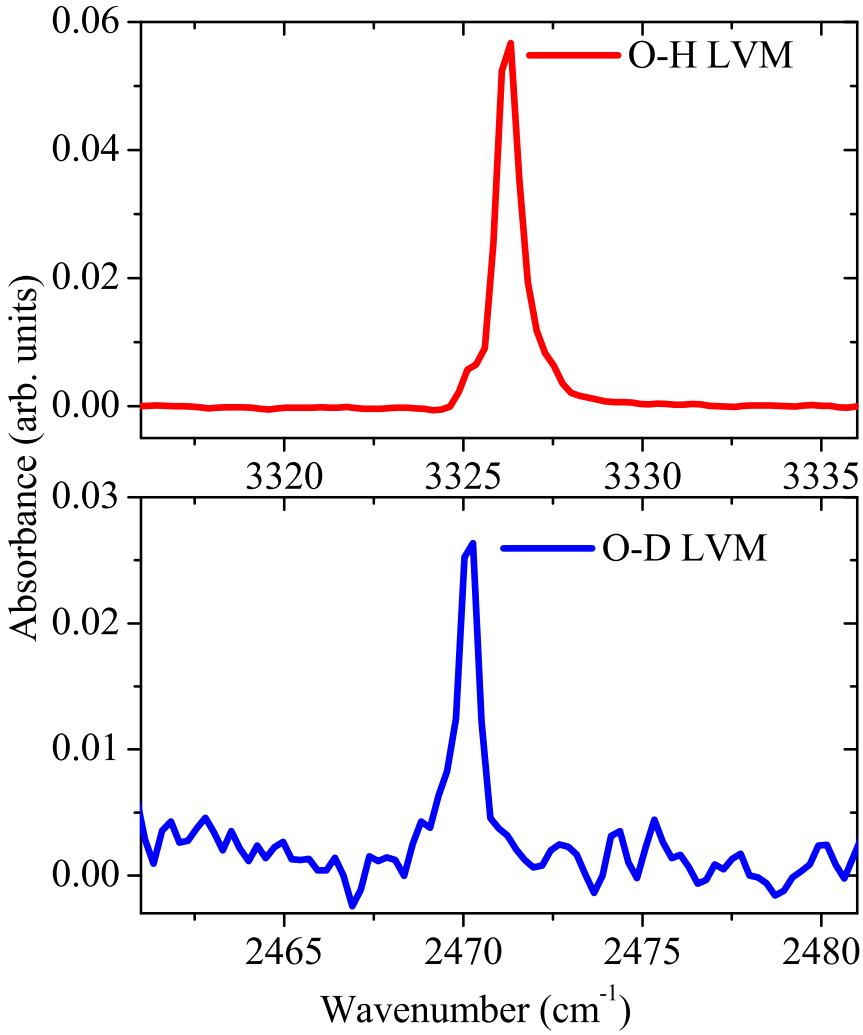

Figure 4.2: The O-H stretch mode at 3326.3 cm^{-1} and O-D stretch mode at 2470.3 cm^{-1}. Both spectra were taken at liquid-helium temperatures.

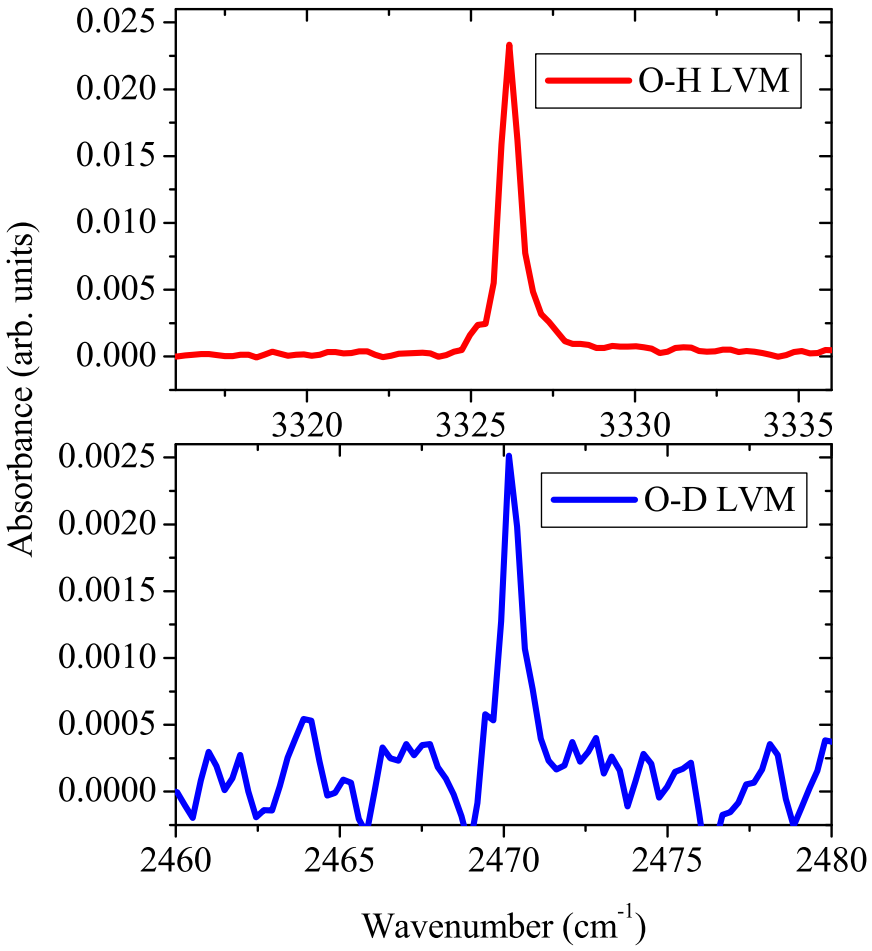

Figure 4.3: ZnO samples annealed in both 1/3 atm. H_2 and 1/3 atm. D_2 show that the O-H and O-D absorption peaks are not of the same intensity. The slower diffusion rate of deuterium may partially account for this difference. However, in samples annealed for long times (+50 hours), the absorption peaks are still different by a factor of 10. The cause of this effect is unknown.

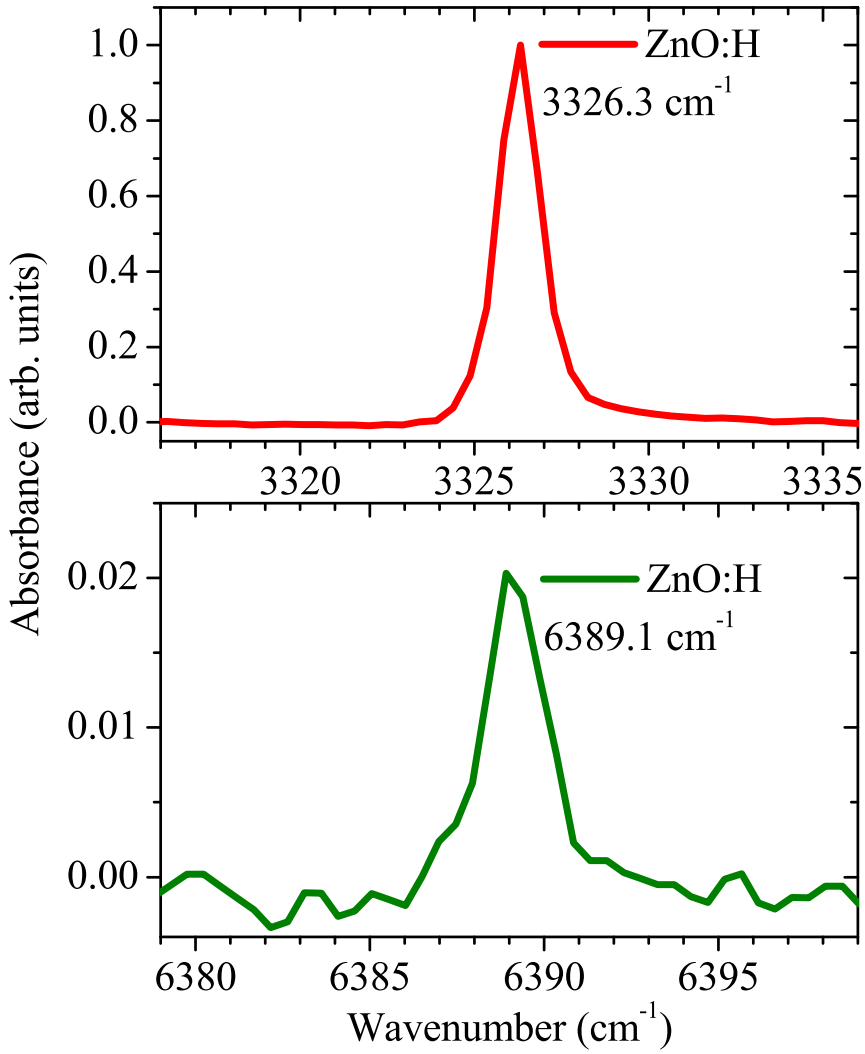

Figure 4.4: The first and second vibrational state of the O-H stretch mode in ZnO at liquid-helium temperatures.

The frequency of the second excited state allows us to compare our results with the harmonic approximation used by Van de Walle. Using the Morse potential as a model, the energy eigenstates are given by

$$E_n = \omega_e \left(n + \frac{1}{2}\right) \left[1 - x_e \left(n + \frac{1}{2}\right)\right], \tag{4.1}$$

where x_e accounts for the anharmonicity of the potential. Equation (4.1) is used to calculate the energy levels E_0, E_1, and E_2. The first and second excited states are given by

$$\Delta E_1 = E_1 - E_0 = \omega_e - 2\omega_e x_e \tag{4.2}$$

and

$$\Delta E_2 = E_2 - E_o = 2\omega_e - 6\omega_e x_e, \tag{4.3}$$

respectively. The harmonic frequency is given by ω_e and the anharmonic term is $\omega_e x_e$. Using 3326 cm^{-1} and 6389 cm^{-1} for the energies of the first and second excited states, we find that ω_e = 3589 cm^{-1} and the anharmonic shift $2\omega_e x_e$ = 263 cm^{-1}. These values are in reasonable agreement with the calculated harmonic frequency and anharmonic shift of 3481 cm^{-1} and -273 cm^{-1}, respectively, for hydrogen in an AB location, bonded with oxygen [Lavrov *et al.* (2002)].

4.2.3 Polarization dependence

As discussed previously, hydrogen annealing produces O-H bonds with an LVM frequency of 3336.8 cm^{-1}, at room temperature. Our observations indicate that hydrogen is bonded with oxygen at an AB location. However, Van de Walle predicted two AB locations where hydrogen would bond with oxygen, one with hydrogen situated along the tetrahedral angle ($\text{AB}_{\text{O},\perp}$) and the other with hydrogen situated along

the c axis ($AB_{O,\parallel}$). Both of these locations were predicted to have similar vibrational frequencies. By determining the O-H bond angle with respect to the c axis, we can determine which prediction is consistent with experiment.

A determination of the O-H bond orientation can be accomplished with the use of an IR polarizer. One of the requirements for a vibrational mode to be observed by IR spectroscopy is that the interaction between the electric field of the IR light and the two bonded atoms must induce a change in the net dipole moment. Conversely, this means that the IR source must emit light with an electric field component aligned in such a way as to induce a change in net dipole moment; otherwise, no IR absorption will occur. In most cases IR spectrometers are designed so that the light source is uniformly polarized. By inserting a polarizer into the beam, we can control the direction of the electric field vector of the IR light. The polarizer allows us to determine the direction of the changing net dipole moment; in the case of a stretch mode, this is also the direction of the bond.

Our results showed an IR absorption peak at 3336.8 cm^{-1} for normal-incidence transmission measurements performed on c-cut ZnO at room temperature. Since the IR light propagates along the c axis, there is no electric field component that is along the O-H bond, for $AB_{O,\parallel}$ complexes. Therefore, we can tentatively eliminate the $AB_{O,\parallel}$ model as a possibility. However, it is difficult to know if the propagation of IR light is perfectly aligned with the c axis. To provide definitive measurements, a polarizer was used for IR light propagating along the c axis as well as propagating perpendicular to the c axis.

The sample used in this experiment was provided by Kelvin G. Lynn, as the samples purchased from Cermet Inc. and Eagle Picher were not thick enough to readily provide all orientations necessary for polarized IR absorption measurements.

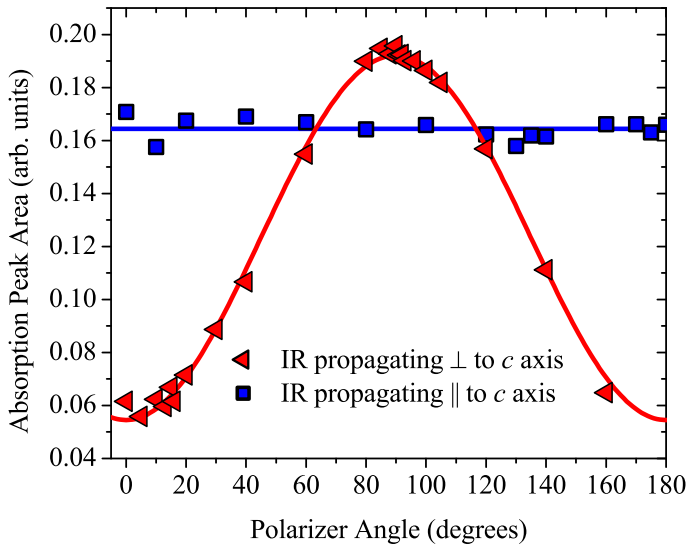

Figure 4.5: Polarization dependence for the O-H stretch mode for light propagating in the indicated directions. For light propagating $\perp$ to the c axis, the angle is with respect to the c axis. The uncertainty for the fitting routine is not shown.

Our results showed that the 3336.8 cm^{-1} absorption peak had no polarization angle dependence for IR light propagating along the c axis. However, the absorption peak does have a polarization angle dependence for light propagating perpendicular to the c axis (Fig. 4.5) [Jokela *et al.* (2003); Jokela and McCluskey (2005)]. In this latter case, the intensity of the absorption peak was at a maximum for polarization perpendicular to the c axis and a minimum, but not zero, for polarization parallel to the c axis. The first result shows that the O-H bonds are oriented symmetrically and radially around the c axis. The second result shows that the bond's orientation is much closer to being perpendicular to the c axis than it is parallel to the c axis. Both of these results are consistent with O-H bonds oriented along the tetrahedral angles of the ZnO crystal, indicating that hydrogen is in the $AB_{O,\perp}$ location. In the next section, we determine

a precise angle that this bond makes with the c axis by looking at the maximum and minimum values for the absorption intensity of polarized IR light propagating perpendicular to the c axis.

4.2.4 Polarization analysis

Since we have confirmed that hydrogen is distributed uniformly around the c axis and its bonds with oxygen are radially directed away from the c axis, we can be reasonably assured that the O-H bonds are in a tetrahedral-like formation around the c axis. An O-H bond parallel to the c axis can be excluded. From symmetry considerations, it is reasonable to assume that the O-H bond is oriented with the same angle to the c axis regardless of which of the three equivalent $AB_{O,\perp}$ locations hydrogen may reside. With these assertions and the data from the polarized IR measurements, we can build a model that will yield the precise angle between the bond direction and the c axis.

If IR light propagates perpendicular to the c axis and the polarization is parallel to the c axis, then the absorption ($I_{P\|c}$) is given by

$$I_{P\|c} \propto 3\cos^2\theta, \tag{4.4}$$

where θ is the angle between the bond direction and the c axis; the multiple of 3 accounts for the three equally probable orientations of the bond around the c axis.

For polarization oriented perpendicular to the c axis, we have a slightly more difficult problem. While each bond is oriented with the same angle θ from the c axis, they are not oriented with the same angle from the polarization direction. If we let ϕ_i represent the angle between each of the three bonds and the polarization (i=1, 2,

or 3) as projected onto the c plane, then we can write the absorption ($I_{P\perp c}$) as

$$I_{P\perp c} \propto \left[\cos^2(\phi_1) + \cos^2(\phi_2) + \cos^2(\phi_3)\right] \cos^2(\theta)\,. \tag{4.5}$$

Each of the three bonds are oriented equally around the c axis (i.e., 120° from each other on the c-plane projection). Hence, Eq. (4.5) can be written in terms of ϕ_1:

$$I_{P\perp c} \propto \left[\cos^2(\phi_1) + \cos^2(120^\circ + \phi_1) + \cos^2(120^\circ - \phi_1)\right] \cos^2(\theta)\,. \tag{4.6}$$

Using the trigonometric identities

$$\cos^2(u) = \frac{1 + \cos(2u)}{2} \tag{4.7}$$

and

$$\cos(u) + \cos(v) = 2\cos\left(\frac{u+v}{2}\right)\cos\left(\frac{u-v}{2}\right), \tag{4.8}$$

we can write Eq. (4.6) as

$$I_{P\perp c} \propto \frac{3}{2}\cos^2(\theta)\,. \tag{4.9}$$

We can now construct a ratio

$$\frac{I_{P\parallel c}}{I_{P\perp c}} = 2\cot^2(\theta)\,. \tag{4.10}$$

By inserting the observed values from Fig. 4.5, we obtain a ratio of 0.284±.008 which yields a value θ=110.6°±0.3°.

The lattice parameters for ZnO, as determined by extended x-ray-absorption fine-structure (EXAFS) calculations are c = 5.220 Å, a = 3.258 Å, and u = 0.382 [Decremps *et al.* (2003)]. A calculation of the angle between the c axis and the

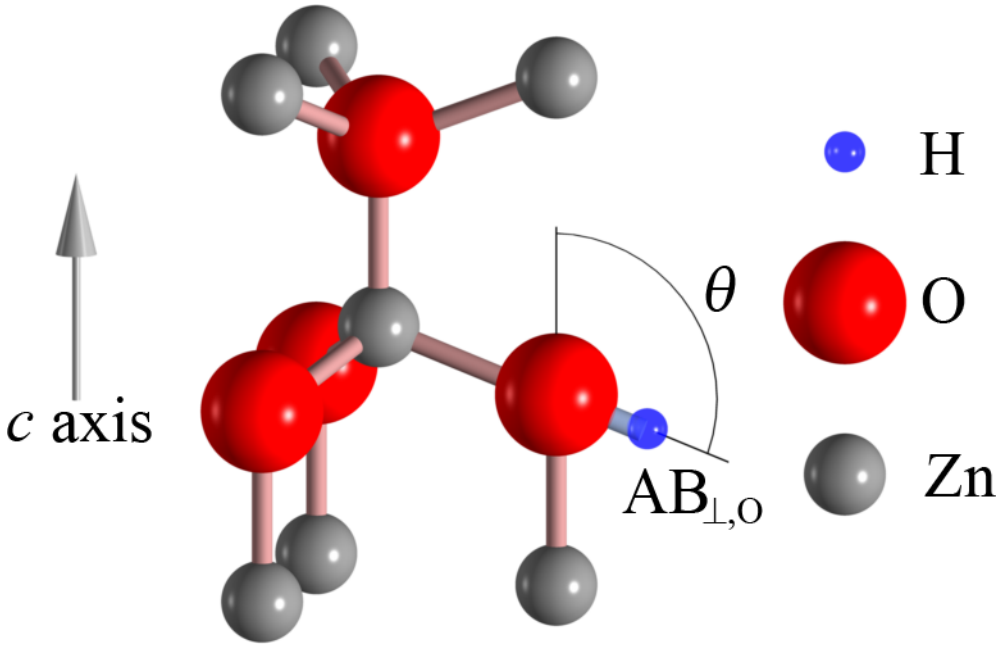

Figure 4.6: Polarized FT-IR measurements are used to determine the angle θ that the O-H bond lies to the c axis.

tetrahedral Zn-O bond using these parameters yields 108.1°. Our polarization measurements yield 110.6°, in good agreement with this calculation.

4.2.5 Pressure dependence

The application of hydrostatic pressure has the potential to help determine the microscopic structure of defects. In predictions made by Limpijumnong and Zhang (2005), the O-H bond formed in ZnO is affected differently depending on whether the hydrogen is in an AB or BC location. Their predictions showed that the vibrational frequency of the bond would increase as 4.2 cm^{-1}/GPa for hydrogen in a BC position and decrease with the same slope for hydrogen in an AB position, with only a slight dependence on whether the hydrogen was oriented along the c axis or at a tetrahedral angle. In the case of an O-H bond in ZnO, these frequency shifts are explained by the

change in bond length accompanied by the increase in pressure. In the BC case, the O-H bond length decreases with increased pressure, causing an increase in the frequency. In the AB case, the O-H bond length increases under pressure due to compression of the neighboring Zn-O bonds, thereby decreasing the bond's vibrational frequency. This behavior is also seen in a calculation of the acetylene molecule (H-C-C-H) where the C-H bond lengths increase when the C-C bond is compressed [Limpijumnong and Zhang (2005)].

The results of our high pressure experiments, performed at liquid-helium temperatures, show that the vibrational frequency decreases with increased pressure (Fig. 4.7). A least-squares fit to the data yields

$$\nu\left(\mathrm{cm}^{-1}\right) = 3326.43 \pm 0.02 - (1.84 \pm 0.03)\, P + (0.069 \pm 0.005)\, P^2, \tag{4.11}$$

where ν is the frequency of the O-H stretch mode and P is the hydrostatic pressure in GPa. The slope of the frequency change is -1.84 cm^1/GPa, which qualitatively agrees with hydrogen in an AB location. However, the observed magnitude of the slope is less than that of the predicted value of -4.2 cm^{-1}/GPa.

Prior to the liquid-helium temperature measurements, we used a DAC with moissanite anvils to take room temperature measurements. A linear fit of the room-temperature data yields

$$\nu\left(\mathrm{cm}^{-1}\right) = 3336.71 \pm 0.27 - (1.18 \pm 0.43)\, P. \tag{4.12}$$

Further evidence that hydrogen is in an AB location is the sublinearity of the frequency shift. In the cases of GaAs [McCluskey *et al.* (1997)] and InP [McCluskey *et al.* (2001)], the magnitude of the pressure-induced frequency shift is sublinear for AB configurations and supralinear for BC configurations.

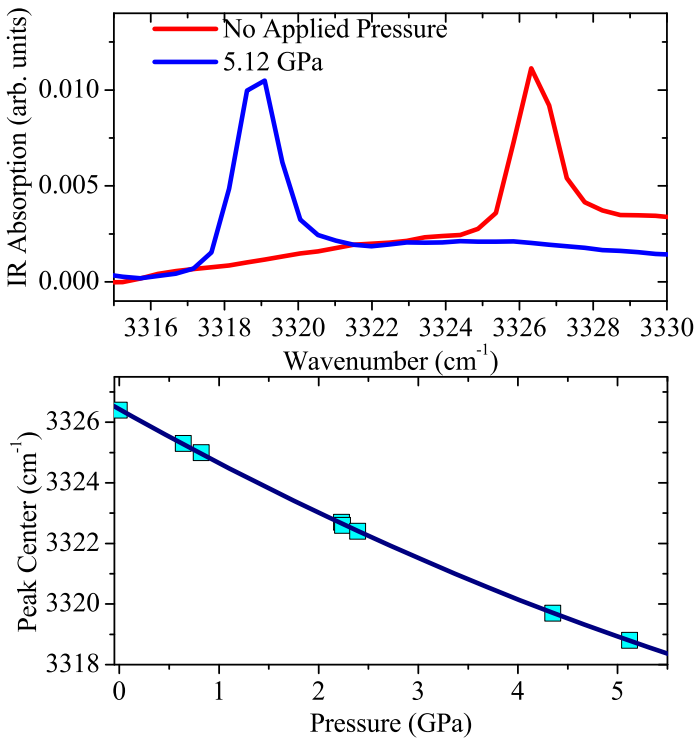

Figure 4.7: Top: The O-H stretch mode at zero applied pressure and 5.12 GPa. Bottom: The O-H stretch mode as a function of pressure. Both plots are for liquid-helium temperatures.

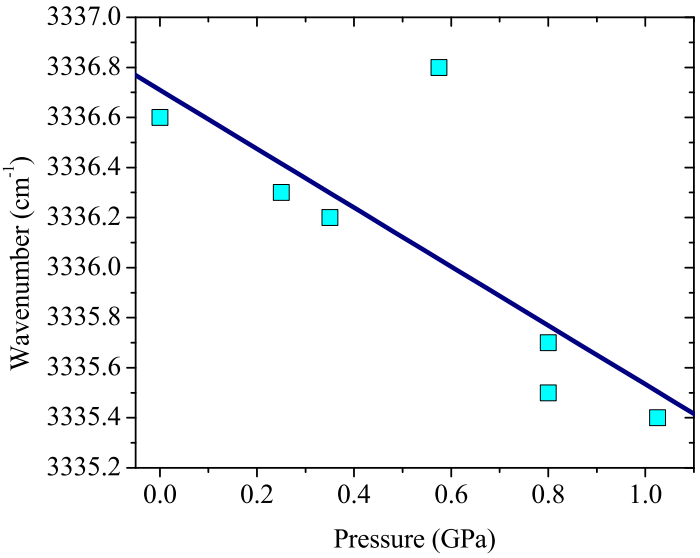

Figure 4.8: The O-H stretch frequency as a function of pressure. Measurements were taken at room temperature inside a DAC with moissanite anvils.

4.2.6 Temperature dependence

The IR absorption spectra were obtained at temperatures between 9 K and room temperature. At room temperature the O-H absorption peak had a vibrational frequency of 3336.8 cm^{-1} and a full-width at half-maximum of 8 cm^{-1}. As the temperature decreased, the peak decreased in vibrational frequency (Fig. 4.9) and narrowed in width. This was also accompanied by an increase in absorption intensity. The shift in vibrational frequency as a function of temperature is modeled by [Persson *et al.* (1985)]

$$\delta\nu = \frac{\delta\nu_0}{\exp\left(h\nu/kT\right) - 1}, \tag{4.13}$$

where h is Planck's constant, k is Boltzmann's constant, and T is the temperature in Kelvin. In this model, the LVM frequency is perturbed by one phonon frequency ν.

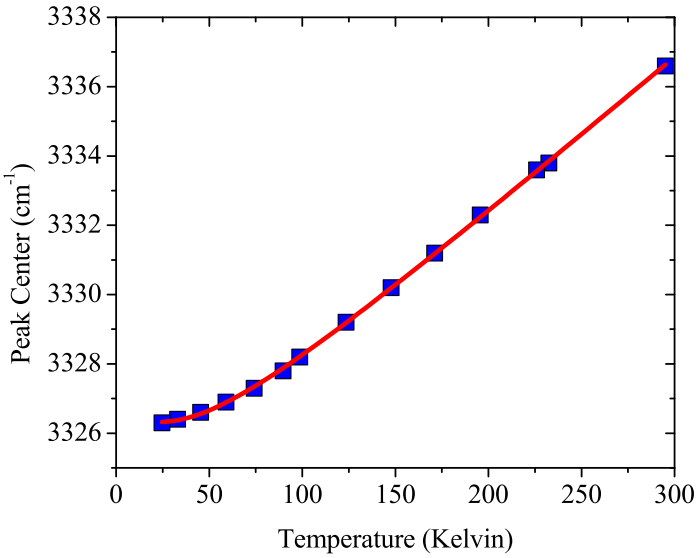

Figure 4.9: O-H stretch frequency as a function of temperature. The line is a fit to Eq. (4.13).

The fit to the data shows that $\delta\nu_0 = 7$ cm^{-1} and $\nu = 100$ cm^{-1}. The value of ν is physically reasonable, since there is a peak in the one-phonon density of states near 100 cm^{-1} [Serrano *et al.* (2003)].

4.2.7 Time dependence

When the hydrogenated samples were stored at room temperature, it was noticed that the O-H absorption peak decreased in intensity. Initially, it appeared that the absorption peak decayed exponentially with time. However, further observation revealed that the decay rate followed the bi-molecular decay scheme (Fig. 4.10), perhaps indicating that hydrogen is forming H_2 [Shi *et al.* (2004)]. Such a decay is described by a bimolecular model (see Sec. 8.1 for derivation), in which hydrogen atoms combine

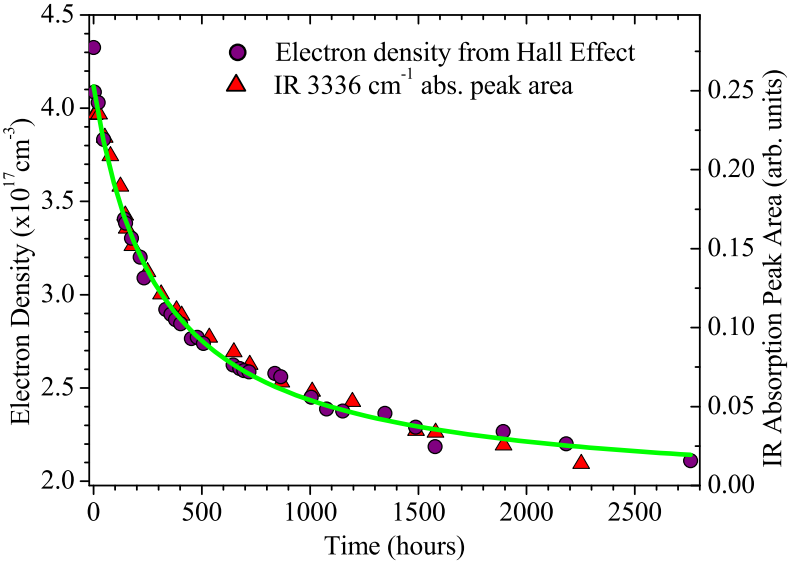

Figure 4.10: Plot of the O-H IR absorbance peak area and the carrier concentration at room temperature. The line is a fit to Eq. (4.14).

to form H_2:

$$n\left(t\right) = \frac{n_0}{\frac{n_0 k}{4} t + 1} + n_{t\to\infty}. \tag{4.14}$$

In this equation, n_0 represents the initial O-H concentration, k is the decay constant, and $n_{t\to\infty}$ represents the minimum value that n approaches as t increases. Equation (4.14) describes the observed decay better than a standard exponential decay, although it still slightly deviates from the data at longer times. The decay in IR absorbance is also well correlated with the decay in free-electron concentration as described in the next section.

The decay of the O-H peak was measured at several different temperatures (Fig. 4.11). The data were fit by

$$\ln k = A - \frac{E_a}{k_B T}, \tag{4.15}$$

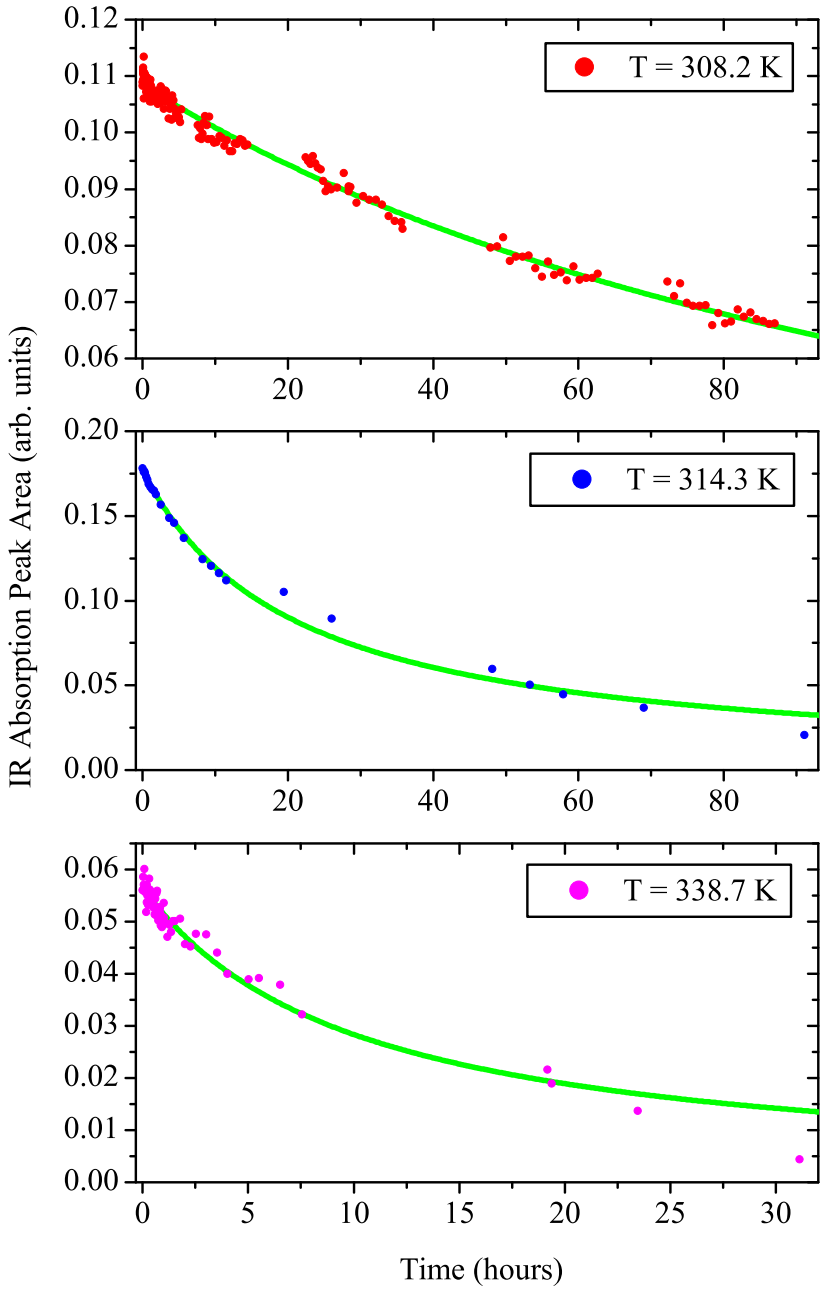

Figure 4.11: Plots showing the decrease in IR absorption peak area as a function of time. The decay is shown for three different temperatures. The green curve is a bimolecular fit to each set of data.

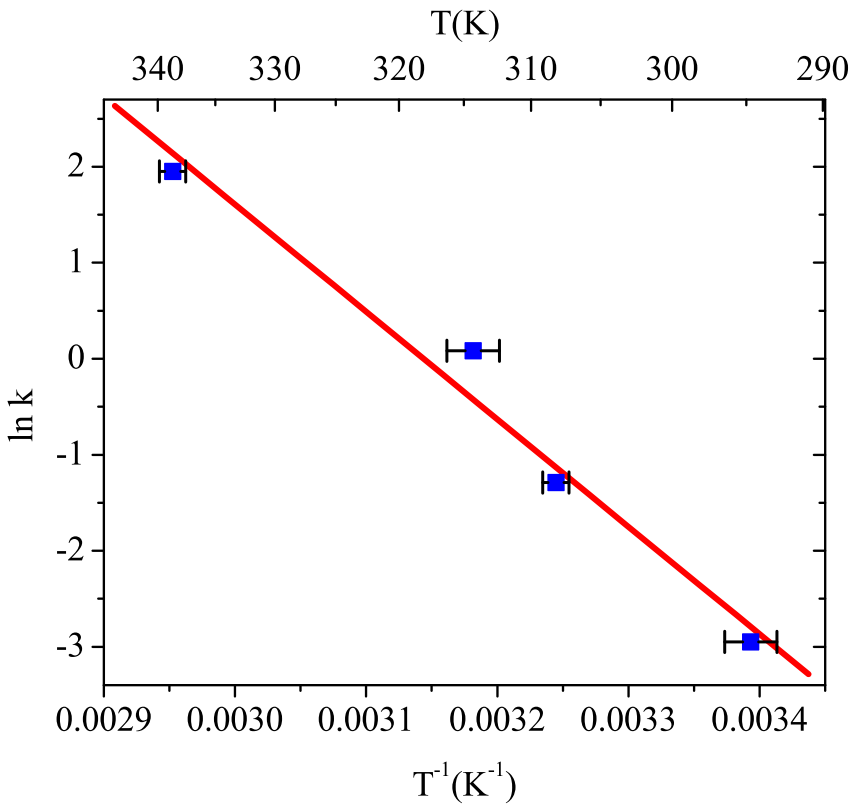

Figure 4.12: Plot of $\ln(k)$ as a function of inverse temperature, yielding an activation energy (E_a) of 0.96 eV. The solid line is a linear fit.

yielding an activation energy $E_a = 0.96$ eV. This value agrees with the diffusion activation energy measured by Mollwo (1954) and Thomas and Lander (1956) of 1.12 eV and 0.91 eV, respectively. The agreement suggests that the formation of H_2 molecules in this temperature range is diffusion-limited.

Upon annealing in open air at 700 °C for one minute, the 3336.8 cm^{-1} peak reappeared, though somewhat weaker than before. This result has been reproduced by others [Shi *et al.* (2004)]. When annealed at lower temperatures, the hydrogen peak does not grow weaker with each anneal, showing that while the O-H bond has been broken, hydrogen does not leave the sample. This supports the hypothesis that immobile H_2 molecules are being formed within the sample.

4.3 Hall effect results and comparison to IR data

The as-grown ZnO sample from Cermet Inc. had an electron carrier density of 1.8×10^{17} cm^{-3}. Immediately after hydrogen annealing, the electron carrier density increased to 4.3×10^{17} cm^{-3}. The carrier density and the O-H IR absorbance peak were monitored separately for two ZnO:H samples that had been simultaneously hydrogenated in the same ampoule. The results show that the two decaying values are very well correlated (Fig. 4.10), providing conclusive evidence that the O-H complexes are shallow donors. From the data we can deduce a calibration factor (ξ) for the following equation:

$$N = \xi \int \alpha(\nu)\, d\nu, \tag{4.16}$$

where N is the O-H donor concentration (cm^{-3}) and the integral is the area of the absorption coefficient of the O-H absorbance peak (cm^{-2}). The absorption coefficient is

$$\alpha(\nu) = \frac{A(\nu)}{x} \ln(10), \tag{4.17}$$

where $A(\nu)$ is the absorbance, x is the sample thickness, and ν is frequency (cm^{-1}). The data show the absorbance peak area and the free-electron concentration as a function of time, from which an average calibration factor of $\xi = 1.6 \times 10^{16}$ cm^{-1} is obtained. This value is in good agreement with hydrogen-related complexes in other semiconductors [Davidson *et al.* (1996)].

At longer times, the IR absorbance peak decays more rapidly than the electron concentration, suggesting the formation of a hidden hydrogen donor [Shi *et al.* (2004)]. Evidence of this "hidden" hydrogen donor has also been observed in as-grown ZnO. One candidate for the hidden donor is a hydrogen-decorated oxygen vacancy, which may have an LVM frequency below our measurement range. It is also possible for hydrogen to bind to a dislocation, an effect seen in crystalline germanium [Haller (1991)].

4.4 Compositional analysis

Observations made by Lavrov *et al.* (2002) showed an IR absorption peak at 3611.3 cm^{-1}, which they attributed to an O-H absorption mode polarized along the c axis. Further studies by Shi *et al.* (2005) determined that samples from different sources, such as Eagle Picher and Cermet Inc., respond differently to hydrogen annealing. Eagle Picher samples reveal the 3611.3 cm^{-1} absorption mode but only a weak 3326.3 cm^{-1} absorption. The exact opposite is seen in Cermet Inc. samples, only showing a weak 3611.3 cm^{-1} mode while a strong 3326.3 cm^{-1} mode is present. In the same study, the samples were illuminated with a tungsten-filament light bulb while the IR spectra were being gathered. The results showed a subtle weakening in the 3326.3 cm^{-1} absorption peak in both samples. However, no change in the 3611.3 cm^{-1} absorption peak was observed. Their conclusion is that due to the lack of a compli-

mentary change in the 3611.3 cm^{-1} absorption line upon secondary illumination, the two absorption lines are not due to the same defect in two different charge states.

Even with the wide interest in these two defects, there have been no conclusive studies performed that show why these two defects show up in different concentrations in samples grown by different methods. In order to determine if a second dopant could be responsible for either one of these peaks, we employed neutron activation analysis (NAA) and secondary-ion mass spectroscopy (SIMS) to determine the composition of the samples.

4.4.1 Neutron activation analysis

Neutron activation analysis was performed at the Nuclear Radiation Center at Washington State University, Pullman, WA [Tbl. 4.1]. It is unknown what effects the heavier isotopes, ^{152}Eu, ^{170}Tm, and ^{177}Lu, have on ZnO. It is also unknown if they are contaminants in as-grown ZnO or if contamination occurred after growth. The similarity in each isotope's concentration between the two samples seems to indicate that either contamination occurred after the crystals were grown or the samples were grown from the same stock of source materials.

4.4.2 Secondary ion mass spectroscopy

Secondary ion mass spectroscopy was performed by the Evans Analytical Group. Two samples of ZnO, one from Cermet and the other from Eagle Picher, were probed for the elements listed in Table 4.2. The collected data show some remarkable differences between the two samples. The most notable is the high concentration of Al in the Cermet Inc. sample, compared to the Eagle Picher sample, and the high concentrations of Ga and B in the Eagle Picher sample, compared to the Cermet Inc. sample.

Isotope	Cermet Inc.	Eagle Picher
^{24}Na	<7.75E16	<8.68E16
^{42}K	<3.88E18	<4.32E18
^{46}Sc	<6.78E13	<7.59E13
^{51}Cr	<5.72E15	<6.29E15
^{56}Mn	<9.44E14	<9.95E14
^{59}Fe	<6.96E17	<7.73E17
^{60}Co	<1.00E17	<1.85E15
^{65}Zn	6.51E22±4.48E21	6.62E22±4.56E21
^{76}As	<3.84E16	<4.30E16
^{85}Sr	<2.60E17	<2.91E17
^{86}Rb	<2.78E16	<3.03E16
^{124}Sb	<5.88E15	<6.56E15
^{134}Cs	<8.51E14	<9.61E14
^{141}Ce	<2.60E15	<2.87E15
^{152}Eu	8.9E16±1.7E16	4.43E16±2.36E16
^{153}Sm	<1.22E15	<1.37E15
^{159}Gd	<1.30E15	<1.45E15
^{160}Tb	<6.43E14	<7.18E14
^{165}Dy	<1.90E15	<2.00E15
^{169}Yb	<5.81E14	<6.41E14
^{170}Tm	5.07E17±2.7E16	5.34E17±2.9E16
^{177}Lu	4.61E17±1.01E17	4.80E17±1.06E17
^{181}Hf	<6.53E14	<7.25E14
^{182}Ta	<9.02E14	<1.00E15

Table 4.1: Results for NAA measurements for ZnO taken by the Nuclear Radiation Center at Washington State University, Pullman. Concentrations are in units of cm^{-3}.

Element	Detection Threshold (T)	Cermet ZnO	Eagle Picher ZnO
H†	2E+19	<T	<T
Li*	3E+13	3.45E+15[b]	<T
B*	2E+14	<T	1.3E+16[a]
C†	3E+18	<T	<T
N†	2E+16	<T	<T
F†	5E+15	<T	<T
Na*	1E+14	1.24E+15[b]	2.04E+14[b]
Mg*	5E+13	1E+16[b]	<T
Al*	1E+14	2.30E+17[a]	1.38E+15[a]
Si†	5E+15	1.0E+17[a]	1.3E+17[a]
Cl†	8E+16	<T	<T
K*	3E+14	<T	<T
Ca*	7E+14	3E+16[b]	<T
Cu*	5E+14	6.55E+14[c]	9.62E+14[c]
Ga*	3E+14	7.80E+14[c]	1.11E+16[c]
Cd*	1E+17	<T	<T
In*	1E+15	<T	<T

Table 4.2: Results for SIMS measurements for ZnO taken by the Evans Analytical Group. Concentrations are in units of cm^{-3}.

$\star$/† Data obtained with O_2^+ / Cs^- ion beam.
[a]Accuracy is better than 20%.
[b]Accuracy is better than 40%.
[c]Accuracy is within an order of magnitude.

Hall effect measurements, on the as-grown Cermet Inc. and Eagle Picher samples used in the SIMS measurements, showed that they contained an electron carrier concentration of $(1.48 \pm 0.03) \times 10^{17}$ cm^{-3} and $(1.10 \pm 0.01) \times 10^{17}$ cm^{-3}, respectively. It's possible that the increased free carrier concentration in Cermet Inc. samples is due to the presence of Al atoms substituting on the Zn lattice.

4.5 Conclusions

We have confirmed that hydrogen does behave as a donor when in an $AB_{\perp}$ location, bonding with oxygen, along one of the tetrahedral Zn-O bonds. Our evidence showed an increase in free carrier concentration upon annealing in hydrogen as well as an O-H bond with a vibrational stretch mode at 3326.3 cm^{-1}. The O-H bond and the free carrier concentration were shown to be correlated as they decayed at room temperature. The decay follows a bimolecular model, suggesting that hydrogen atoms are forming hydrogen molecules when they break away from the oxygen atom. Observations at several different temperatures show that the decay process is limited by a barrier with energy 0.96 eV. This value corresponds well with the energy of the hydrogen diffusion barrier observed by Mollwo (1954) and Thomas and Lander (1956).

It was thought that hydrogen may be an excellent candidate for the controlled n-type doping of ZnO. Our experiments seem to indicate that this is not the case. However, the formation of a "hidden" hydrogen donor does indicate that hydrogen presents a problem for the production of p-type ZnO. The results of the SIMS measurements also show several contaminants in both Cermet Inc. and Eagle Picher ZnO. These contaminants may also be to blame for the n-type conductivity of as-grown

ZnO from these companies. In light of these impurities, it is recommended that other sources of ZnO be procured or grown for further studies in this field.

Chapter 5

ZINC OXIDE GROWN BY CHEMICAL VAPOR TRANSPORT

In an attempt to investigate individual types of defects, we used chemical vapor transport (CVT) to grow our own ZnO crystals [Look *et al.* (1999); Mycielski *et al.* (2004)]. By growing our own crystals we could ensure that we had some control over contaminants and dopants in our crystals, something that cannot easily be done with purchased ZnO.

5.1 Physical properties of resulting growth

The quality of the ZnO growth created in this research was judged primarily by macroscopic observations, supplemented by FT-IR spectroscopy. Several factors affected the resulting ZnO crystal growth, including temperature, ZnO microparticle preparations, and dopants introduced both intentionally and unintentionally.

Our highest quality crystal growth was achieved with the use of high purity ZnO microparticles and graphite obtained from Sigma-Aldrich. The ZnO microparticles were aggregated by mixing with high-purity low-contamination (HPLC) H_2O and then boiling the water away. Pieces of the ZnO aggregate (1.5 g) and some graphite (2.0 g) were sealed in a fused-silica ampoule with 1/2 atm. Ar gas. The sealed portion of the ampoule was 9.5 cm in length and 1.7 cm in diameter. The end of the ampoule with the source material was heated to a temperature of 850°C. The natural temperature gradient of the furnace left the opposite end of the ampoule at approximately 800°C.

The resulting growth appeared to have grain sizes as large as 0.5 mm in diameter and 1.0 mm in length. The crystals were nearly colorless, exhibiting only a slight green-yellow color common in most high quality ZnO single crystals.

In our early attempts to grow ZnO, we used a source of graphite that was contaminated with an unknown material. The resulting growth would become orange when the source temperature exceeded 900°C (in contrast, the color of high quality growth with pure graphite had no noticeable temperature dependence in the range of 850°C to 920°C). Additionally, metallic droplets were visible on the exposed surface of the ZnO growth. The orange color suggests that a Zn rich environment was created [Mikami *et al.* (2005)]. The temperature dependence would seem to indicate that a chemical reaction between the graphite impurity and oxygen from the ZnO is creating a Zn rich environment.

To confirm that a Zn rich environment produces orange crystals, 0.5 g of Zn was added to the graphite-ZnO mixture that produced high quality crystals. The source temperature was set to 920°C. The resulting growth was deep-orange in color. Excess Zn formed a layer between the ZnO growth and the ampoule wall. Zinc droplets were also visible on the exposed surface of the ZnO growth.

5.1.1 Detailed growth results using contaminated graphite

The graphite used for our first series of crystal growth was obtained from graphite brushes used in electric motors. The graphite was ground up using a mortar and pestle to obtain a microparticle powder. When using microparticle ZnO, we obtained crystal sizes ranging from needle growth to small hexagonal crystals (Fig. 5.1). By using aggregated ZnO, we decreased the variation in sizes while increasing the overall size of individual crystals (Fig. 5.2). The use of an Ar or NH_3 ambient seemed to have

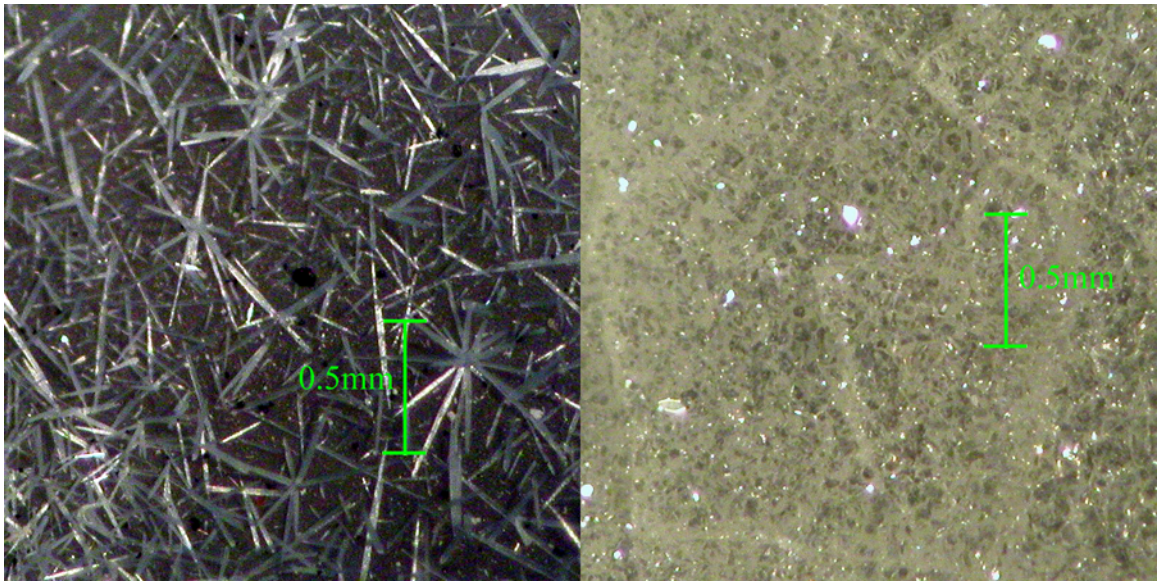

Figure 5.1: ZnO whisker growth (left) and small hexagonal crystal growth (right) obtained using the CVT method using contaminated graphite and ZnO micropowder as the source materials.

little effect on the resulting growth. When growth was conducted at temperatures above 900°C, the samples would take on an orange color. The surface of the samples were scattered with small metallic spheres, with higher densities located at the coolest part of the crystal during crystal growth (Fig. 5.3).

5.1.2 Detailed growth results using pure graphite

Upon the discovery of a contaminant in our graphite, we decided to obtain high purity graphite from Sigma-Aldrich. We continued to use aggregated ZnO microparticles as the source material, as that produced the largest crystals in our previous experiments. Various growth attempts were made using either Ar or NH_3 as an ambient with temperatures ranging between 850°C and 920°C. The resulting crystal

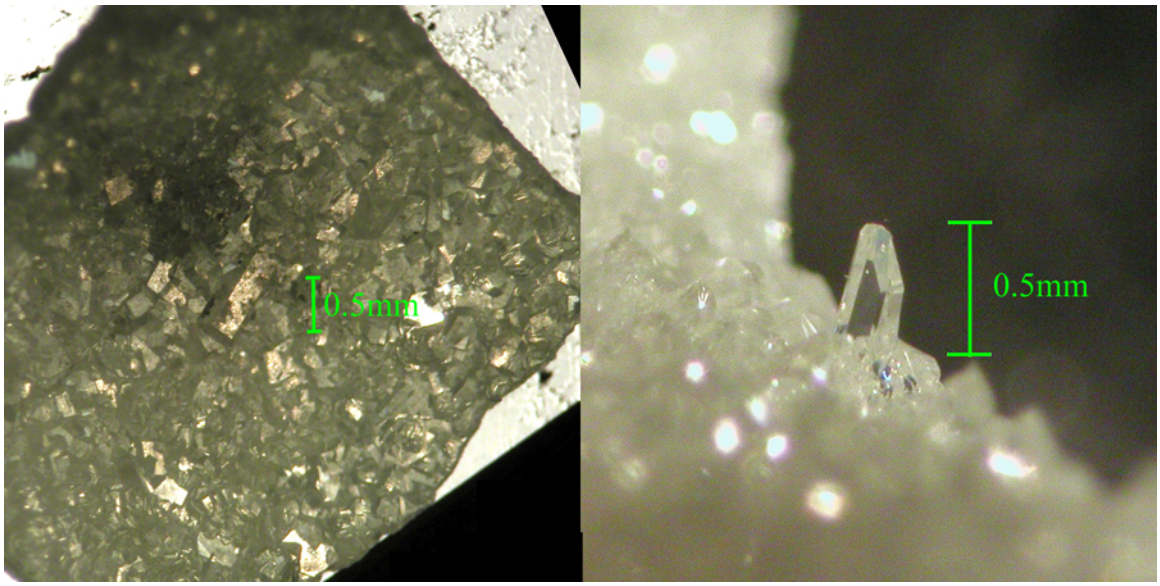

Figure 5.2: ZnO hexagonal crystal growth using contaminated graphite and aggregated ZnO microparticles as the source materials. The ambient gases used for each growth are Ar (left) and NH_3 (right).

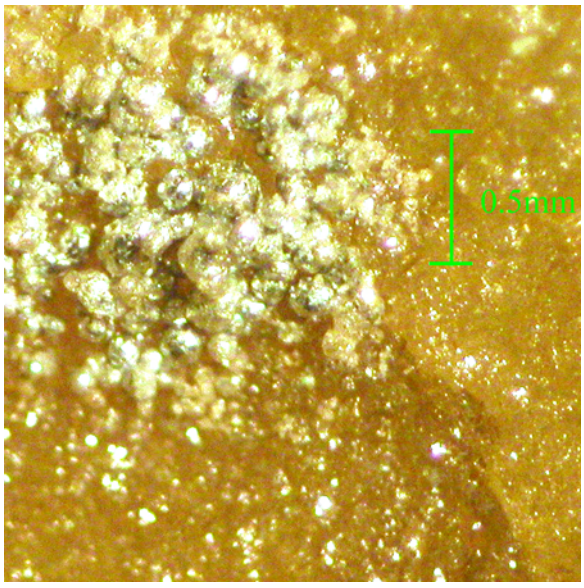

Figure 5.3: ZnO growth using the CVT method with contaminated graphite and ZnO aggregated microparticles as source materials. The samples take on an orange color when grown at temperatures in excess of 900°C.

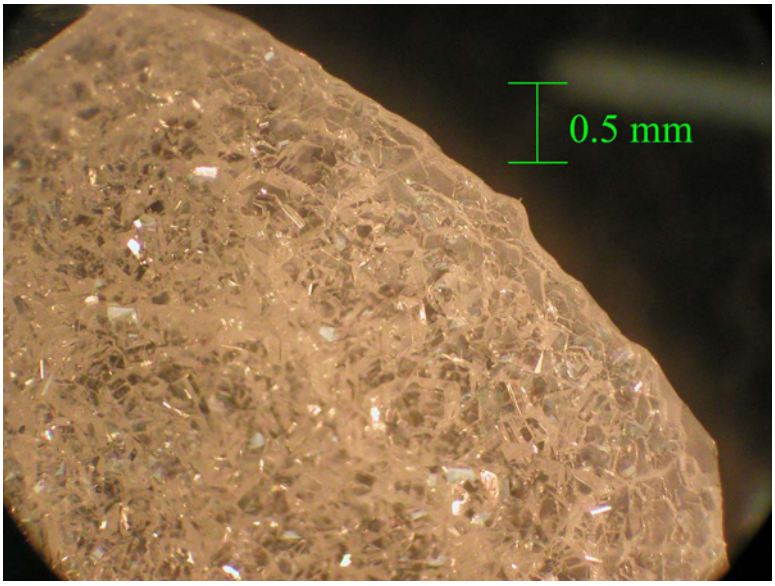

Figure 5.4: ZnO hexagonal structures grown using CVT with a pure source of graphite and aggregated ZnO microparticles. Samples were colorless for all temperatures attempted between 850°C and 920°C.

growth seemed to be rather consistent regardless of these factors. We were unable to reproduce orange growth using these conditions (Fig. 5.4).

Using evidence of a correlation between excess Zn and orange-colored ZnO, we included Zn particles with the aggregated ZnO microparticles and graphite source materials.

5.1.3 Comparison between contaminated and pure graphite growth

The only way to achieve orange-colored ZnO using the pure graphite was to add Zn metal to the source materials. The color was much deeper than that in the ZnO grown using the contaminated graphite. While the composition of the contaminated graphite has not been tested, we think that the difference between the two samples is the amount of excess Zn available during crystal growth. It is possible that several

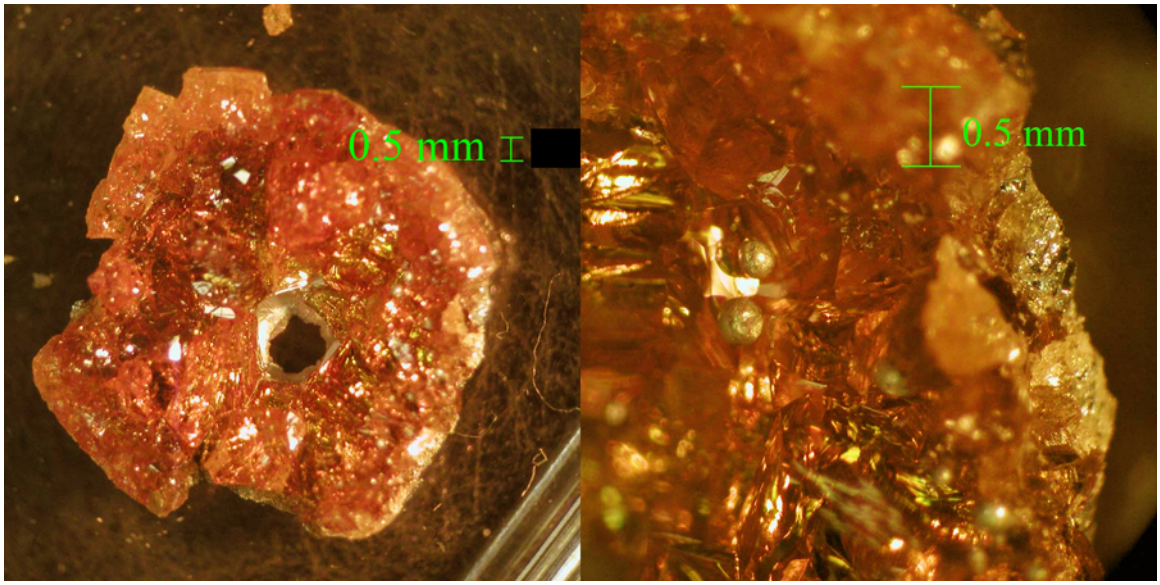

Figure 5.5: ZnO grown by the CVT method using aggregated ZnO microparticles, pure graphite, and Zn particles. The orange-red color is correlated with the presence of excess Zn during crystal growth. The magnified image (right) shows two spheres of Zn metal on the surface of the orange-red ZnO growth. The color of these photos have been adjusted by eye in an attempt to closely match the color of the resulting growth.

impurities exist in the graphite, one of which is Zn, or that the impurities assist in creating a Zn rich environment.

5.2 FT-IR results

High quality ZnO showed an absorption peak at 3326.3 cm^{-1}, which we have previously associated with O-H donors. It is reasonable to attribute the source of hydrogen to the ZnO aggregate which was formed by mixing with HPLC H_2O and the boiling away the water. It is expected that some water remains in the ZnO aggregate and is responsible for forming O-H bonds in our ZnO growth. Annealing in hydrogen at 720°C increases the LVM absorption at 3326.3 cm^{-1} and shows an LVM absorption at 3611.3 cm^{-1}. The absorption at 3611.3 cm^{-1} is the same as that observed by Lavrov *et al.* (2002). Annealing in deuterium gas confirms this by showing corresponding absorption peaks at 2470.3 cm^{-1} and 2668.0 cm^{-1}, associated with the isotopic shift of the 3326.3 cm^{-1} and 3611.3 cm^{-1} absorption peaks, respectively.

Zinc oxide grown using the contaminated graphite source also showed an LVM absorption peak at 3147.5 cm^{-1} at room temperature. The absorption peak appears to be stable, only dissociating at temperatures above 700°C (Fig. 5.7). Hydrogen annealing resulted in an increase in the 3147.5 cm^{-1} absorption peak, indicating that a hydrogen related bond is responsible. At liquid-helium temperatures, the absorption peak shifts to 3150.6 cm^{-1}. Annealing in deuterium showed an absorption peak at 2339.7 cm^{-1} at liquid-helium temperatures, corresponding to the isotopic shift of the LVM observed with a frequency of 3150.6 cm^{-1} (Fig. 5.8). The ratio between these two absorption peaks is $r = 1.3466$, nearly the same value of the ratio obtained for the 3326.3 cm^{-1} O-H and 2470.3 cm^{-1} O-D LVMs ($r = 1.3465$). The ratio strongly suggests that these new absorption peaks are also due to an O-H related complex.

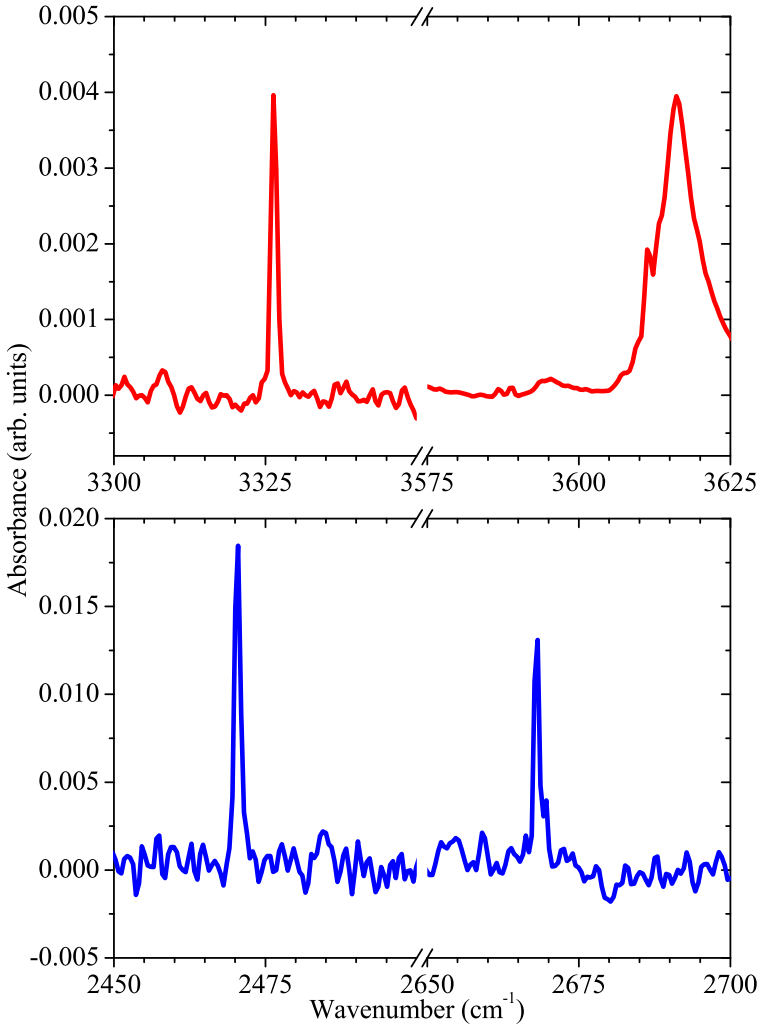

Figure 5.6: Top: The 3326.3 cm^{-1} and 3611.3 cm^{-1} O-H absorption peaks in ZnO grown by the CVT method with contaminated graphite. The broad absorption peak near 3617 cm^{-1} is a feature in both the as-grown ZnO spectrum and the ZnO:H spectrum. It may be a feature of the spectrometer. Bottom: Annealing in deuterium reveals the O-D absorption peaks at 2470.3 cm^{-1} and 2668.0 cm^{-1}. The larger absorption of the deuterium-related LVM, as compared to the hydrogen-related LVM, can be attributed to variations in the thickness of the polycrystalline growth as well as variations in annealing times and temperatures between the ZnO:H and ZnO:D samples.

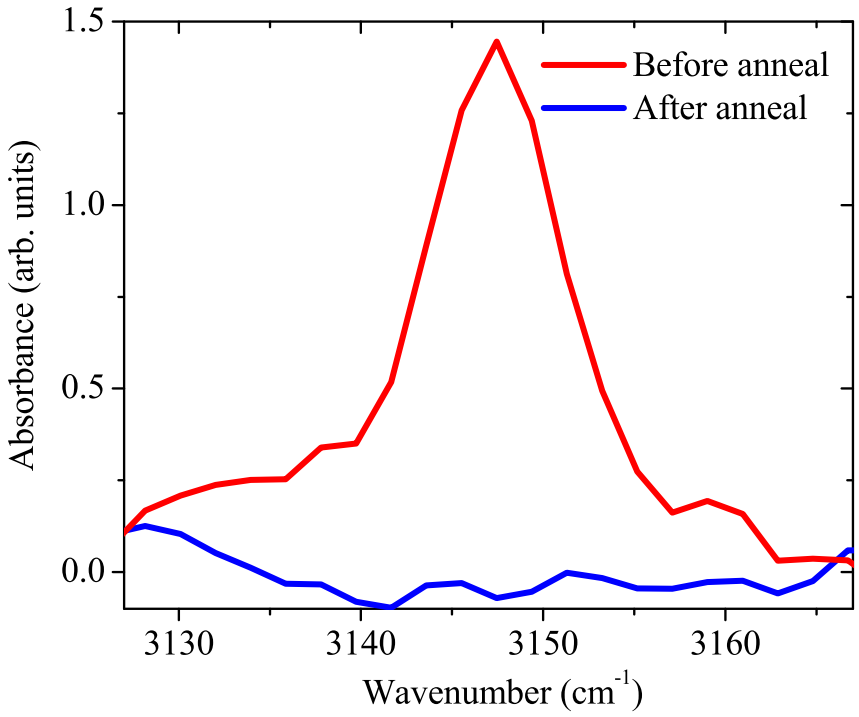

Figure 5.7: Absorption spectrum for ZnO grown by CVT method at a temperature above 900°C. The 3147.5 cm^{-1} absorption peak is no longer present after an anneal for one hour at 810°C in open air. An anneal at 610°C for thirty minutes showed no decay in the absorption peak.

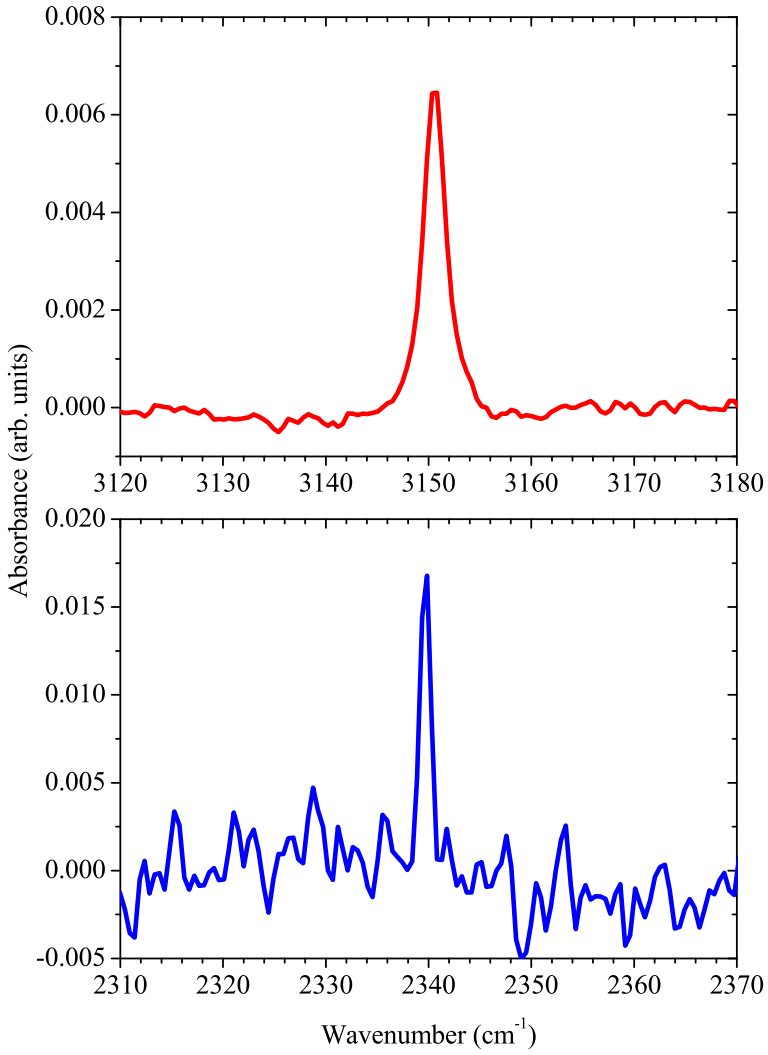

Figure 5.8: Top: The hydrogen related absorption peak at 3150.6 cm^{-1}. Bottom: Upon annealing in deuterium, the 2339.7 cm^{-1} absorption peak appears. Both spectra were taken at liquid-helium temperatures. The difference in intensities between the hydrogen-related and deuterium-related absorption peaks can be attributed to variations in the thickness of the polycrystalline growth.

Samples that were grown with high purity graphite in a Zn rich environment showed no O-H related LVMs at room temperature. This was the case for both as-grown samples and samples that were annealed in hydrogen. However, the free carrier absorption does increase after annealing in hydrogen. These results seem to indicate that hydrogen is still behaving as a donor even though it is not forming the 3326.3 cm^{-1} O-H complex.

5.3 Composition

The metallic droplets deposited on the ZnO that was grown using the contaminated graphite were analyzed via electron microprobe. The analysis showed the droplets to be composed of Zn, supporting our previous speculation that the orange color of the crystal is a result of growth conducted in a Zn rich environment.

Analysis of the FT-IR spectra show that hydrogen is present in the samples, the source of which is attributed to the water used in the ZnO aggregation process. It is known that the 3326.3 cm^{-1} is related to O-H bonds. However, the nature of the LVM at 3150.6 cm^{-1} is uncertain. The isotopic shift ratio would liken it to the previously observed O-H LVM, indicating that hydrogen is again bonding with oxygen. However, the isotopic shift ratio alone is not proof. Furthermore, the only samples that this is observed in are those grown with the contaminated graphite source, indicating that the 3150.6 cm^{-1} LVM is related to an element other than oxygen.

Chapter 6
CONCLUSIONS

Our results show conclusively that hydrogen can act as a donor in ZnO. The results also show that the O-H bond formed by hydrogen at the $AB_{O,\perp}$ site is unstable at room temperature. While the hydrogen remains in the crystal, it no longer behaves as a donor when the O-H bond is broken, perhaps because it forms H_2 molecules. This means hydrogen alone is not a suitable dopant for long-term control of the *n*-type conductivity of ZnO. However, it may play an important role in compensating or passivating acceptors.

CVT-grown ZnO, with impure graphite, contained a hydrogen related absorption peak at 3150.6 cm^{-1}, the 3326.3 cm^{-1} LVM related to hydrogen in the $AB_{O,\perp}$ location, and the 3611.3 cm^{-1} absorption peak as found by Lavrov *et al.* (2002), at liquid-helium temperatures. It is clear that the absorption peak at 3150.6 cm^{-1} is related to a defect in the CVT-grown ZnO. It is possible that this absorption peak is caused by hydrogen in the $AB_{O,\perp}$ location, complexed with an unknown acceptor at the Zn site. This could explain a shift in frequency from 3326.3 cm^{-1} to 3150.6 cm^{-1}. *Ab initio* calculations by Wardle *et al.* (2005) show that Cu_{Zn} is an excellent candidate for trapping hydrogen; the LVM frequency for such a complex is theorized to be 3150 cm^{-1}. It is also possible that hydrogen is bonding with another impurity in our CVT-grown ZnO. While the isotopic shift ratio seems to indicate that hydrogen is still forming a complex with oxygen, some other element of similar mass may be complexed with hydrogen.

It is not known why the results of hydrogenation differ between samples of ZnO grown by different methods. Lavrov *et al.* (2002) found that the defect related to the 3611.3 cm^{-1} was due to hydrogen in the $BC_{\|}$ position. Our results indicate that the 3326.3 cm^{-1} absorption peak is due to hydrogen in the $AB_{O,\perp}$ position. Shi *et al.* (2005) showed that the intensity of these peaks, and the likelihood of hydrogen residing in a particular location, depended on the method used to grow the ZnO crystal. From these results it is obvious that at least one of these two peaks is related to a defect, the cause of which is, in turn, related to the method of crystal growth. The defect is responsible for changing the preferred location for hydrogen within the ZnO crystal lattice. The nature of this defect, be it extended or point, has yet to be determined. The SIMS results showed a few impurities that differed between Cermet Inc. and Eagle Picher samples. While some of these impurities are most likely partially responsible for the *n*-type conductivity in as-grown ZnO, it is not known how they affect the preferred location for hydrogen.

Chapter 7
FUTURE RESEARCH

The use of ZnO in commerce and industry has not yet reached its full potential. The development of a solid method for creating p-type ZnO will result in a wide range of devices that were not possible with opaque wide-band-gap semiconductors. In understanding ZnO's potential, one realizes that further research on this material is warranted. The research that has been started and discussed in this paper is not yet complete. While we, in collaboration with many other researchers, have determined that hydrogen does play a vital role in the n-type conductivity of as-grown ZnO, there are still more questions that must be answered.

The discovery of the 3150.6 cm^{-1} absorption peak reiterates a good question; what defects are involved in affecting the preferential location for hydrogen diffused into ZnO? The possibility that Cu_{Zn} is somehow related to the 3150.6 cm^{-1} absorption peak is intriguing and requires further study. The suggested experiment is to grow ZnO:Cu using the CVT method with a subsequent anneal in hydrogen gas.

7.1 Summary of Tasks

- Determine composition of contaminated graphite.
- Hydrogenate a piece of ZnO:Cu grown by the CVT method.
- Attempt seeded chemical vapor transport (SCVT) growth.

- Use SCVT growth to determine hydrogen-related bond orientation for the 3150 cm^{-1} absorption peak.

- Attempt Hall effect measurements on CVT or SCVT-grown ZnO.

- Have orange samples of CVT-grown ZnO treated in oxygen. Compare results between samples grown with contaminated graphite and samples grown using high-purity graphite with added Zn.

- Continue research on identifying and eliminating donors in ZnO.

- Continue research on identifying promising methods for creating p-type ZnO.

Chapter 8

APPENDICES

8.1 Derivation of the bimolecular decay model

The bimolecular decay has been applied to the dissociation of O-H bonds in our samples of ZnO. Our observations revealed that atomic hydrogen was breaking away from oxygen at a rate far different than what could be described by the exponential decay. We knew that hydrogen was not leaving the crystal, but was no longer visible with IR light. We know that H_2 molecules are not directly visible with IR light. With this in mind we decided to apply the bimolecular model to the dissociation of O-H bonds, where hydrogen atoms only break away to form H_2 molecules, a decay that would not follow the exponential model.

In this section, I derive the bimolecular model where both reactants are atomic hydrogen. To begin we look at the rate associated with decays:

$$-\frac{d\,[n(t)]}{dt} = k\frac{[n(t)]}{2}\frac{[n(t)]}{2}, \tag{8.1}$$

where $[n(t)]$ is the concentration of O-H bonds in our ZnO sample and k is a proportionality constant (decay constant). To begin we will condense this to

$$-\frac{dn(t)}{dt} = \frac{k}{4}n^2(t), \tag{8.2}$$

where we have dropped the chemist's notation where [N] represents the concentration of N. A quick observation tells us that we are looking for solutions that go as a function of $\frac{1}{t}$, i.e.

$$-\frac{d\left(\frac{1}{t}\right)}{dt} = \left(\frac{1}{t}\right)^2. \tag{8.3}$$

The general form of this equation is

$$n(t) = \frac{1}{At+B} + C. \tag{8.4}$$

In this form $C = \lim_{t\to\infty}\left[n\left(t\right)\right]$ which we will represent by $n_{t\to\infty}$, and $n(0) = \frac{1}{B} + C$. For convenience we will represent $\frac{1}{B}$ with n_0. So far we have the solution

$$n(t) = \frac{1}{At+\frac{1}{n_0}} + n_{t\to\infty}. \tag{8.5}$$

Putting this in a simpler form we have

$$n(t) = \frac{n_0}{n_0 At+1} + n_{t\to\infty}, \tag{8.6}$$

where we have simply multiplied the first term by $\frac{n_0}{n_0}$. If we take the first derivative of Eq. (8.5), we obtain

$$n'(t) = \frac{d\left(At+\frac{1}{n_0}\right)^{-1}}{dt} = -A\left(At+\frac{1}{n_0}\right)^{-2}, \tag{8.7}$$

so that $A = \frac{k}{4}$. The solution is then

$$n(t) = \frac{n_0}{\frac{n_0 k}{4}t+1} + n_{t\to\infty}. \tag{8.8}$$

8.2 Harmonic motion of two masses attached by a spring

We use this model to approximate the local vibrational mode frequency associated with attaching a light atom to a crystal lattice. Two masses, m_1 and m_2, are attached by a spring of length d with spring constant k. According to Hooke's Law, the force applied by a spring is

$$F = -kx, \tag{8.9}$$

where x is the change in length of the spring. If we now have two masses attached on either side of the spring, we can write the force applied to each mass as

$$\begin{aligned} m_1\ddot{x}_1 &= -k\left(x_1 - x_2 - d\right) \\ m_2\ddot{x}_2 &= k\left(x_1 - x_2 - d\right) \end{aligned}, \tag{8.10}$$

where x_1 and x_2 are the positions and $\ddot{x}_1$ and $\ddot{x}_2$ are the accelerations for masses m_1 and m_2, respectively. Letting the change in length of the spring $x = x_1 - x_2 - d$ then Eq. 8.10 becomes

$$\begin{aligned} m_1\ddot{x}_1 &= -kx \\ m_2\ddot{x}_2 &= kx \end{aligned}. \tag{8.11}$$

Since we defined $x = x_1 - x_2 - d$, we also defined $\ddot{x} = \ddot{x}_1 - \ddot{x}_2$. Applying this to Eq. 8.11, we can write

$$\ddot{x} = \frac{-kx}{m_1} - \frac{kx}{m_2} = -kx\left(\frac{1}{m_1} + \frac{1}{m_2}\right). \tag{8.12}$$

If we define μ as the reduced mass, we can write Eq. 8.12 as

$$\ddot{x} = -\frac{k}{\mu}x, \tag{8.13}$$

where

$$\mu = \left(\frac{1}{m_1} + \frac{1}{m_2}\right)^{-1} = \frac{m_1 m_2}{m_1 + m_2}. \tag{8.14}$$

The solution to Eq. 8.13 is of the form

$$x(t) = A\sin(\omega t) + B\cos(\omega t), \tag{8.15}$$

where ω is the angular frequency. By setting the initial conditions to $x(0) = h$ and $\dot{x}(0) = 0$, we can write the solution as

$$x(t) = h\sin(\omega t). \tag{8.16}$$

We can determine ω by taking the second derivative of Eq. 8.16 and comparing it to Eq. 8.13:

$$\ddot{x}(t) = -\omega^2 h\sin(\omega t) = -\frac{k}{\mu}x(t). \tag{8.17}$$

We now recognize that

$$\omega^2 = \frac{k}{\mu}, \tag{8.18}$$

therefore

$$\omega = \sqrt{\frac{k}{\mu}}. \tag{8.19}$$

Chapter 9

PUBLICATIONS RESULTING FROM THIS WORK

1. McCluskey MD, Jokela SJ, Zhuravlev KK, Simpson PJ, and Lynn KG, "Infrared spectroscopy of hydrogen in ZnO," Appl. Phys. Lett. **81** (2002) 3807-9.

2. Jokela SJ, McCluskey MD, and Lynn KG, "Infrared spectroscopy of hydrogen in annealed zinc oxide," Physica B **340-342** (2003) 221-4.

3. McCluskey MD and Jokela SJ, "Infrared spectroscopy of hydrogen in ZnO," in *Hydrogen in Semiconductors*, edited by Nickel NH, McCluskey MD, and Zhang SB (*Mat. Res. Soc. Symp. Proc.* **813**, Warrendale, PA, 2004) H3.2.

4. Jokela SJ and McCluskey MD, "Structure and stability of O-H donors in ZnO from high-pressure and infrared spectroscopy," Phys. Rev. B **72** (2005) 113201.

5. McCluskey MD and Jokela SJ, "Hydrogen donors in zinc oxide," in *Proceedings of the NATO Advanced Workshop on Zinc Oxide*, edited by Nickel N and Terukov E, NATO Science Series II, Vol. **194** (2005) 125-32.

6. McCluskey MD, Jokela SJ, and Hlaing Oo WM, "Hydrogen donors in zinc oxide," in *Semiconductor Defect Engineering Materials, Sythetic Structures and Devices*, edited by Ashok S, Chevallier J, Sopori BL, Tabe M, and Kiesel P (Mater. Res. Soc. Symp. Proc. **864**, Warrendale, PA, 2005), E10.4.

7. McCluskey MD, Jokela SJ, and Hlaing Oo WM, "Hydrogen in bulk and nanoscale ZnO," Physica B **376-377** (2006) 690-3.

8. Huso J, Morrison JL, Hoeck H, Chen X, Bergman L, Jokela SJ, McCluskey MD, and Zheleva T, "Pressure response of the ultraviolet photoluminescence of ZnO and MgZnO nanocrystallites," Appl. Phys. Lett. **89** (2006) 171909.

BIBLIOGRAPHY

Aoki T, Shimizu Y, Miyake A, Nakamura A, Nakanishi Y, and Hatanaka Y, Phys. Status Solidi B **229** (2002) 911.

Bardeen J and Brattain WH, Phys. Rev. **74** (1948) 230.

Barker AS Jr. and Sievers AJ, Edited by Pines D, Rev. Mod. Phys. **47** (2) (1975).

Bergman K, Stavola M, Pearton SJ, and Lopata J, Phys. Rev. B **37** (1988a) 2770.

Bergman K, Stavola M, Pearton SJ, and Lopata J, Mat. Res. Soc. Symp. Proc. **104** (1988b) 281.

Brandt MS, Johnson NM, Molnar RJ, Singh R, and Moustakas TD, Appl. Phys. Lett. **64** (1994) 2264.

Cermet Inc., www.cermetinc.com.

Chang KJ and Chadi DJ, Phys. Rev. Lett. **60** (1988) 1422.

Chevallier J, Dautremont-Smith WC, Tu CW, and Pearton SJ, Appl. Phys. Lett. **47** (1985) 108.

Chevallier J and Aucouturier M, Ann. Rev. Mater. Sci. **18** (1988a) 219.

Chevallier J, Pajot B, Jalil A, Mostefaoui R, Rahbi R, and Boissy MC, Mat. Res. Soc. Symp. Proc. **104** (1988b) 337.

Chevallier J, Clerjaud B, and Pajot B, Semiconductors and Semimetals, edited by Pankove JI and Johnson NM (Academic Press, Orlando FL), Vol **34**, Ch 13 (1991).

Cohen-Tannoudji C, Diu B, and Laloë F, in Quantum Mechanics, (Hermann, Paris, France), Vol **1**, (1977).

Cox SFJ, Davis EA, Cottrell SP, King PJC, Lord JS, Gil JM, Alberto HV, Vilão RC, Piroto Duarte J, Ayres de Campos N, Weidinger A, Lichti RL, Irvine SJC, Phys. Rev. Lett. **86** (2001) 2601.

Davidson BR, Newman RC, Joyce TB, and Bullough TJ, Semicond. Sci. Technol. **11** (1996) 455.

Decremps F, Datchi F, Saitta AM, Polian A, Pascarelli S, Di Cicco A, Itié JP, and Baudelet F, Phys. Rev. B **68** (2003) 104101.

Didosyan YS, Hauser H, Reider GA, and Toriser W, J. Appl Phys. **95** (2004) 7339.

Dietl T, Ohno H, Matsukura F, Cibert J, and Ferrand D, Science **287** (2000) 1019.

Dietl T and Ohno H, MRS Bulletin **28** (2003) 714.

Eagle Picher, www.eaglepicher.com.

Estreicher SK, Throckmorton L, Marynick DS, Phys. Rev. B **39** (1989) 13241.

Evans Analytical Group LLC, www.eaglabs.com.

Fellgett P, J. Phys. Radium **19** (1958) 187.

Fiederling R, Keim M, Reuscher G, Ossau W, Schmidt G, Waag A, and Molenkamp LW, Nature **402** (1999) 787.

Forman RA, Piermarini GJ, Barnett JD, and Block S, Science **176** (1972) 284.

Gil JM, Alberto HV, Vilão RC, Piroto Duarte J, Ayres de Campos N, Weidinger A, Krauser J, Davis EA, Cottrell SP, and Cox SFJ, Phys. Rev. B **64** (2001) 075205.

Götz W, Johnson NM, Bour DP, McCluskey MD, and Haller EE, Appl. Phys. Lett. **69** (1996) 3725.

Gray PV and Brown DM, Appl. Phys. Lett. **8** (1966) 31.

Griffiths PR and de Haseth JA, Chemical Analysis, (John Wiley & Sons, New York, NY), Vol. **83** (1986).

Haller EE, Semiconductors and Semimetals, edited by Pankove JI and Johnson NM (Academic Press, Orlando FL), Vol **34**, Ch 11 (1991).

Herzberg G, *Molecular Spectra and Molecular Structure I: Spectra of Diatomic Molecules* (Krieger, Malabar, FL, 1989), p. 560.

Hofmann DM, Hofstaetter A, Leiter F, Zhou H, Henecker F, Meyer BK, Orlinskii SB, Schmidt J, and Baranov PG, Phys. Rev. Lett. **88** (2002) 045504.

Ohno Y, Young DK, Beschoten B, Matsukura F, Ohno H, and Awschalom DD, Nature **402** (1999) 790.

Jacquinot P, Rep. Prog. Phys. **23** (1960) 267.

Jalil A, Chevallier J, Azoulay R, and Mircea A, J. Appl. Phys **59** (1986) 3774.

Jalil A, Chevallier J, Pesant JC, Mostefaoui R, Pajot B, Murawala P, and Azoulay R, Appl. Phys. Lett. **50** (1987) 439.

Janotti A and Van de Walle CG, J. Cryst. Growth **287** (2006) 58.

Johnson NM, Herring C, and Chadi DJ, Phys. Rev. Lett. **56** (1986a) 769.

Johnson NM, Burnham RD, Street RA, and Thornton RL, Phys. Rev. B **33** (1986b) 1102.

Jokela SJ, McCluskey MD, and Lynn KG, Physica B **340-342** (2003) 221.

Jokela SJ and McCluskey MD, Phys. Rev. B **72** (2005) 113201.

Jonker BT, Park YD, Bennett BR, Cheong HD, Kiosoglou G, and Petrou A, Phys. Rev. B **62** (2000) 8180.

Kamilla SK and Basu S, Bull. Mater. Sci. **25** (2002) 541.

Kikkawa JM and Awschalom DD, Nature **397** (1999) 139.

Kim KK, Kim HS, Hwang DK, Lim JH, and Park SJ, Appl. Phys. Lett. **83** (2003) 63.

Kittel C, Introduction to Solid State Physics 8th Ed., (John Wiley & Sons, Hoboken, NJ), Chp. 4 (2005) 89.

Kobayashi A, Sankey OF, and Dow JD, Phys. Rev. B **28** (1983) 946.

Lavrov EV, Weber J, Börrnert F, Van de Walle CG, Phys. Rev. B **66** (2002) 165205.

Li X, Yan Y, Gessert TA, Perkins CL, Young D, Dehart C, Young M, and Coutts TJ, J. Vac. Sci. Technol. **21** (2003) 1342.

Limpijumnong S and Zhang SB, Appl. Phys. Lett. **86** (2005) 151910.

Limpijumnong S, Zhang SB, Wei SH, and Park CH, Phys. Rev. Lett. **92** (2004) 155504.

Look DC, Reynolds DC, Sizelove JR, Jones RL, Litton CW, Cantwell G, and Harsch WC, Solid State Commun. **105** (1998) 399.

Look DC, Hemsky JW, and Sizelove JR, Phys. Rev. Lett. **82** (1999) 2552.

Look DC, Mater. Sci. Eng. B **80** (2001) 383.

Look DC, Reynolds DC, Litton CW, Jones RL, Eason DB, and Cantwell G, Appl. Phys. Lett. **81** (2002) 1830.

Look DC, Claflin BB, Cantwell G, Park S, and Renlund GM, Zinc Oxide - A Material for Micro- and Optoelectronic Applications, edited by Nickel NH and Terukov E (Springer, Dordrecht, Netherlands), NATO Science Series II **194** (2005) 37.

Mao HK, Bell PM, Shaner JW, and Steinberg DJ, J. Appl. Phys **49** (1978) 3276.

McCluskey MD, Hsu L, Wang L, and Haller EE, Phys. Rev. B **54** (1996) 8962.

McCluskey MD, Haller EE, Walker J, Johnson NM, Vetterhöffer, Weber J, Joyce TB, and Newman RC, Phys. Rev. B **56** (1997) 6404.

McCluskey MD, Zhuravlev KK, Davidson BR, and Newman RC, Phys. Rev. B **63** (2001) 125202.

McCluskey MD, Jokela SJ, Zhuravlev KK, Simpson PJ, and Lynn KG, Appl. Phys. Lett. **81** (2002) 3807.

McCluskey MD and Zhuravlev KK, J. Chem. Phys. **116** (2002) 1607.

Merrill L and Bassett WA, Rev. Sci. Instr. **45** (1974) 290.

Mikami M, Eto T, Wang J, Masa Y, and Isshiki M, J. Crys. Growth **276** (2006) 389.

Minami T, MRS bulletin **25** (2000) 38.

Mollwo E, Z. Phys. **138** (1954) 478.

Mycielski A, Kowalczyk L, Szadkowski A, Chwalisz B, Wysmołek A, Stępniewski R, Baranowski JM, Potemski M, Witowski A, Jakieła R, Barcz A, Witkowska B, Kaliszek W, Jędrzejczak A, Suchocki A, Łusakowska E, and Kamińska E, J. All. Com. **371** (2004) 150.

Nakahara K, Takasu H, Fons P, Yamada A, Iwata K, Matsubara K, Hunger R, and Niki S, J. Cryst. Growth **237** (2002) 503.

Nanhdra PS, Newman RC, Murray R, Pajot B, Chevallier J, Beal RB, and Harris JJ, Semicond. Sci. Technol. **3** (1988) 356.

Nause J and Nemeth B, Semicond. Sci. Tech. **20** (2005) S45.

Ntep JM, Hassani SS, Lusson A, Tromson-Carli A, Ballutaud D, Didier G, and Triboulet R, J. Cryst. Growth **207** (1999) 30.

Nuruddin A and Abelson JR, Thin Solid Films **394** (2001) 49.

Pan N, Lee B, Bose SS, Kim MH, Hughes SJ, Stillman GE, Arai K, and Nashimoto Y, Appl. Phys. Lett. **50** (1987a) 1832.

Pan N, Bose SS, Kim MH, Stillman GE, Chambers F, Devane G, Ito CR, and Feng M, Appl. Phys. Lett. **51** (1987b) 596.

Pankove JI, Carlson DE, Berkeyheiser JE, and Wance RO, Phys. Rev. Lett. **53** (1984) 856.

Pankove JI, in Hydrogen in Semiconductors, edited by Pankove JI and Johnson NM, (Academic Press, Inc., San Diego, CA) Vol. **34**, Ch. 3 (1991).

Pajot B, Jalil A, Chevallier J, and Azoulay R, Semicond. Sci. Technol. **2** (1987) 305.

Pajot B and Song C, Phys. Rev. B **45** (1992) 6484.

Parkin S, Jiang X, Kaiser C, Panchula A, Roche K, and Samant M, Proceedings of the IEEE **91** (2003) 661.

Pearton SJ, Dautremont-Smith WC, Chevallier J, Tu CW, and Cummings KD, J. Appl. Phys. **59** (1986) 2821.

Pearton SJ, Norton DP, Ip K, Heo YW, and Steiner T, J. Vac. Sci. B **22** (2004) 932.

Persson BNJ and Rydberg R, Phys. Rev. B **32** (1985) 3586.

Prinz GA, Science **282** (1998) 1660.

Ryu YR, Lee TS, and White HW, Appl. Phys. Lett. **83** (2003) 87.

Sah CT, Sun JYC, and Tzou JJ, Appl. Phys. Lett. **43** (1983) 204.

Schiferl D, Cromer DT, and Mills RL, High Temp. High Pressures **10** (1978) 493.

Serrano J, Manjón FJ, Romero AH, Widulle F, Lauck R, and Cardona M, Phys Rev. Lett. **90** (2003) 055510.

Shi GA, Saboktakin M, Stavola M, and Pearton SJ, Appl. Phys. Lett. **85** (2004) 5601.

Shi GA, Stavola M, Pearton SJ, Thieme M, Lavrov EV, and Weber J, Phys. Rev. B **72** (2005) 195211.

Shockley W and Pearson GL, Phys. Rev. **74** (1948) 232.

Singh AV, Mefra RM, Wakahara A, and Yoshida A, J. Appl. Phys **93** (2003) 396.

Smith JW, Tokach HMD, Goodband RD, Nelssen JL, and Richert BT, J. Animal Sci. **75** (1997) 1861.

Stavola M, Pearton SJ, Lopata J, and Dautremont-Smith WC, Appl. Phys. Lett. **50** (1987) 1086.

Steane A, Reports on Progress in Physics **61** (1998) 117.

Sterer E, Pasternak MP, and Taylor RD, Rev. Sci. Instr. **61** (1990) 1117.

Thomas DG and Lander JJ, J. Chem. Phys. **25** (1956) 1136.

Ulrici W, Czupalla M, and Seifert M, Phys Status Solidi B **210** (1998) 551.

Van de Walle CG, Phys. Rev. Lett. **85** (2000) 1012.

van der Pauw LJ, Philips Tech. Rev. **20** (1958/59) 220.

Wager JF, Science **300** (2003) 1245.

Wardle MG, Goss JP, and Briddon PR, Phys. Rev. B **72** (2005) 155108.

Wikipedia, http://en.wikipedia.org/wiki/Neutron_activation_analysis, (Nov. 2006).

Xu J and Mao H, Science **290** (2000) 783.

Zutic I, Fabian J, and Das Sarma S, Phys Rev B **64** (2001) 121201.